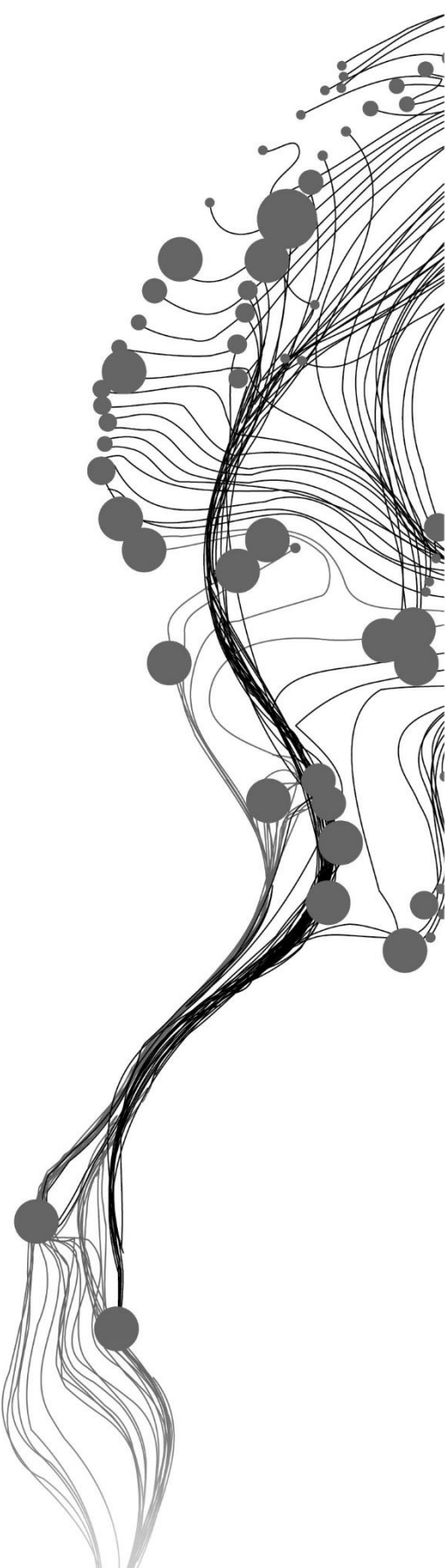


MULTI-FREQUENCY SAR DATA- BASED PolInSAR INVERSION MODELING FOR FOREST HEIGHT RETRIEVAL

AKSHAT RAWAT
November, 2021

SUPERVISORS:
Dr. Shashi Kumar (IIRS)
Dr. Hossein Aghababaei (ITC)



MULTI-FREQUENCY SAR DATA- BASED PolInSAR INVERSION MODELING FOR FOREST HEIGHT RETRIEVAL

AKSHAT RAWAT

Enschede, The Netherlands, November, 2021

Thesis submitted to the Faculty of Geo-Information Science and Earth Observation of the University of Twente in partial fulfilment of the requirements for the degree of Master of Science in Geo-information Science and Earth Observation.

Specialization: Geo-Information Science and Earth Observation

SUPERVISORS:

Dr. Shashi Kumar (IIRS)

Dr. Hossein Aghababaei (ITC, University of Twente)

THESIS ASSESSMENT BOARD:

Prof Dr. Ir. A. Stein (Chair, ITC, University of Twente)

Dr. Anup Das (External Examiner, SAC, Ahmedabad)

etc

DISCLAIMER

This document describes work undertaken as part of a programme of study at the Faculty of Geo-Information Science and Earth Observation of the University of Twente. All views and opinions expressed therein remain the sole responsibility of the author, and do not necessarily represent those of the Faculty.

Dedicated to Nana Nani
Dadi Maa Paa and Di.

ABSTRACT

With the threat of climate change and its impact on the plant and animal life on earth looming around us for over decades, it becomes necessary to understand the concept of climate change. An increase of the global temperature is a direct impact of the climate change process, resulting in subsequent rise in sea levels, stronger cyclones, and wildfires. The effects of these on animal life can be deciphered easily, but their effects on plant life is adverse and can only be understood with a proper study. Forests store in them huge amount of carbon, with the majority being stored in the trees and soil, constituting to the biomass. Using the height of the trees in the region, diameter at the breast height of all those trees, and the density, the above ground biomass is estimated. When a calamity such as forest fires, or deforestation occurs in a forest area, it helps in determining the amount of carbon released into the environment, and subsequent steps that must be taken to account for the loss that occurred during the event. This study focuses on determining one of the bio-physical components of the trees, the tree height using spaceborne Synthetic Aperture Radar (SAR) data, with the chosen area being the Manali forest ranges, Ram Bagh and Van Vihar in Himachal Pradesh, India. Data from multiple frequencies, X, C, and L band data are used in this study with the Polarimetric SAR Interferometry (PolInSAR) technique being implied as it has shown potential to determine accurate forest height results over many studies in the past (Aghabalaei et al., 2020; Chen et al., 2021; Denbina et al., 2018). Baseline simulation was carried to estimate the value of baseline compatible with the corresponding height of ambiguity, since prior knowledge of the forest height of the area was present. This was used to calculate the vertical wavenumber. Three Stage Inversion (TSI) and Coherence Amplitude Inversion (CAI) models were used in the study for determining the forest height. The modelled height was then validated with the field data of the field work carried out by Dr. Shashi Kumar in the year 2012. While the accuracy of the modelled height with CAI technique ranged between 84% and 92% for the three sets of data, it ranged between 91% and 95% for them when TSI technique was used. Further, the Global Ecosystem Dynamics Investigation (GEDI) product, 2019 global forest canopy height map was used for comparison with the field work as well as with the modelled height. It was observed at many places, the GEDI data had underestimated the forest height values, while at some places with lesser forest area, GEDI had not estimated the forest height. The changes in tree height due to temporal gap between the year of the field work and the acquisition date of the data pairs were not considered in the scope of the study. The forest ranges in the study are old and the trees are matured to their maximum height by the time field data was performed. The results suggested the use of TerraSAR-X data for the estimation of tree height in the region as its accuracy was most with the least RMSE value. Amongst TSI and CAI, TSI model was preferred since the inaccurate heights of urban and riverbed could be dealt with using a two-step improved TSI technique.

Keywords: Forest height, PolInSAR, synthetic aperture radar, coherence, interferometry, three stage inversion.

ACKNOWLEDGEMENTS

Throughout my journey of the master's course, completing the research has been a roller coaster ride for me with multiple challenges on some weeks to weekend getaway with friends. I would like to express my gratitude to everyone who have helped me in any stage of this research.

The biggest person in the list is my mentor at IIRS, Dr. Shashi Kumar, who has helped me innumerable number of times since the research work commenced in September 2020. His words have always encouraged me to focus on the task at hand. The important concepts explained by him are something I will remember for my lifetime.

My ITC supervisor, Dr. Hossein Aghababaei has always been there to clear my doubts away, for which I will always be grateful. The important suggestions and recommendations he provided in the thesis are invaluable.

I would sincerely thank Dr. Sameer Saran and Dr. Sander Oude Elberink for the help offered during the courses at IIRS-ITC and their concern over the thesis work, which made me work relentlessly on some days. At last, I would also thank Dr. Alfred Stein for his useful comments and suggestions regarding the thesis work, during the proposal and the midterm defence which made me refine my work further.

During the stress days, Maa, Paa and Di have always blown away those stress clouds out with the phone conversations and made me believe in myself whenever I felt low.

My grandmothers, uncles, aunts, and brothers never made me feel out of home with the love they showered on me during these 2 years. Their tasty food is something I will cherish for a long time.

I would like to thank all my friends, who became a family, and made the hostel days look like my home. The biggest support came from my best friend Alice, who helped me the most in thesis writing and calmed me down on all occasions. For all the fun times and exciting tours at Dehradun and the Netherlands, I would like to thank Awinash Singh, Jitendra Shankaraiah, Waris Hooda, Sidharth Narayan Borah, Nomit Rawat, and Masud Islam.

TABLE OF CONTENTS

1. INTRODUCTION.....	11
1.1. Background.....	12
1.2. Motivation.....	13
1.3. Research Objective.....	14
1.3.1. Sub-objectives of the study	14
1.3.2. Research questions to be addressed.....	14
2. LITERATURE REVIEW.....	15
2.1. Relation of forest with the biomass	15
2.2. Methods used in estimating the forest height	15
2.3. Working of Synthetic Aperture Radar in brief.....	16
2.4. Advanced SAR techniques for forest height retrieval.....	18
2.4.1. Estimation of forest height using PolInSAR technique	19
2.4.2. Forest height retrieval using InSAR technique	19
2.4.3. PolInSAR technique for forest height retrieval	20
2.5. Decomposition techniques in SAR.....	27
2.6. Inversion models for estimation of forest height.....	28
2.6.1. Three Stage Inversion model	29
2.6.2. Coherence Amplitude Inversion model	32
3. STUDY AREA	33
3.1. Dataset.....	34
3.2. Field data.....	34
3.3. Global Ecosystem Dynamics Investigation (GEDI) data.....	37
4. METHODOLOGY.....	38
4.1. Co-registration of image pair.....	38
4.2. Generation of kz number	38
4.3. T6 coherency matrix	39
4.4. Complex coherence.....	39
4.5. Forest height estimation using Three Stage Inversion and Coherence Amplitude Inversion.....	40
4.6. Range doppler terrain correction and masking.....	40
4.7. Validation of results	40
5. RESULTS AND DISCUSSION	42
5.1. Shift due to co-registration	42
5.2. Obtaining the T6 matrix.....	45
5.3. Baseline estimation and kz calculation	47
5.4. Complex coherences in various polarisation basis	48
5.5. Forest height.....	62

5.6.	Validation of the obtained forest height	64
5.6.1.	Using field values.....	64
5.6.2.	Using GEDI data	68
5.6.3.	Comparing field values with GEDI derived height	71
5.7.	Sources of error	72
6.	CONCLUSIONS AND RECOMMENDATIONS.....	74
6.1.	Conclusions	74
6.2.	Recommendations.....	75

LIST OF FIGURES

Figure 1: Shows the interference of atmospheric particles on the wavelength range of the electromagnetic spectrum, with an emphasis on the visible range and microwave range. (DePasquale et al., 2015)	12
Figure 2: Backscattered information of target is equal to combination of all backscattered information gathered from the target in between time T-1 and T-3, elongating the length of aperture virtually, and improving the azimuth resolution.....	17
Figure 3: Front view of how a SAR sensor gathers data. Transmitted signal wave is red in colour, while backscattered signals are shown in green colour. Side looking property of sensor overcomes the left-right ambiguity of a nadir looking SAR sensor. As a result, wave reaches and backscatters from Object 1 earlier than Object 2, enabling it to be identified as the object closer to the sensor.....	18
Figure 4: Shows the working of InSAR (PolInSAR in case of Polarimetric data). Data acquisition from different locations generates a baseline useful in estimating vertical structures accurately.	20
Figure 5: Polarization ellipse is shown in the image. Upon interaction with various features, the POA, denoted by ψ in this figure, changes, altering the power of various scattering types.....	23
Figure 6: An illustration of a unit circle with phase and coherence values and coherence region that contains all possible polarization combinations. In this example, the green coloured dot depicts the coherence value of HV polarisation while the red coloured dot depicts the coherence value of HH polarisation in linear basis. The blue coloured shape consists of coherence values of all possible polarisations in the linear basis and is defined as the coherence region.	27
Figure 7: Different types of scatterings	28
Figure 8: Schematic diagram of the three-stage inversion model.....	29
Figure 9: representation of inversion of γ in a unit circle.....	31
Figure 10: Standard False Colour Composite image of the region obtained using Sentinel-2B optical satellite.....	33
Figure 11: Figure showing Dr. Shashi Kumar using a laser dendrometer RD1000 to obtain the tree heights within a plot of 0.1 hectare. Image was taken on 27 November 2012.	35
Figure 12: Figure showing the gaps between trees which could help the non-penetrating waves detect ground information. Image was taken on 27 November 2012.	35
Figure 13: A field visit photo depicting the height of the trees in the region, which could increase up to 50 meters. Though, most of the trees were about 40 meters tall. Image was taken on 27 November 2012.	36
Figure 14: The region was undulating with tree ranges too having topographic variations because of mountains. Image was taken on 30 November 2012, a day before the satellite pass.....	36
Figure 15: Flowchart explaining the methodology of this study.	41

Figure 16: Pauli RGB images of RADARSAT-2 data. Left side: S1 scattering matrix, right side: S2 scattering matrix. Here, red: double bounce scattering component, blue: surface scattering component, and green: volumetric scattering component. 43

Figure 17: Pauli RGB images of ALOS-2 data. Left side: S1 scattering matrix, right side: S2 scattering matrix. Note that, image is inverted vertically because terrain correction was not performed in this step. Here, red: double bounce scattering component, blue: surface scattering component, green: volumetric scattering component, and white: presence of all the scattering components equally. 44

Figure 18: Pauli RGB images of TerraSAR-X data. Left side: S1 scattering matrix, right side: S2 scattering matrix. Note that, image is inverted horizontally because terrain correction was not performed in this step. Here, red: double bounce scattering component, blue: surface scattering component, green: volumetric scattering component..... 45

Figure 19: Zoomed in portion of multilooked Pauli RGB image of RADARSAT-2 data after the generation of T6 coherency matrix. Left: T1, right: T2. Significant double bounce scattering (red coloured pixels) can be seen in the Manali city with a dominant volumetric scattering (in green colours) in the forest areas. Surface scattering in blue colours can also be seen in many parts of the image..... 46

Figure 20: Zoomed in portion of multilooked Pauli RGB image of ALOS-2 data after the generation of T6 coherency matrix. Left: T1, right: T2. Whitish colours imply the presence of all the three types of scattering in the area. Forests have only volumetric scattering (green coloured pixels), while urban area has dominant double bounce scattering along with volumetric scattering at some places..... 46

Figure 21: Zoomed in portion of multilooked Pauli RGB image of TerraSAR-X data after the generation of T6 coherency matrix. Left: T1, right: T2. While T1 shows significant surface scattering all over the area, the same area gets substituted to double bounce scattering. Though, urban area cannot be distinguished looking at the T2 RGB image, forests can still be distinguished easily..... 47

Figure 22: Subset of coherence values of HH (left) and HV (right) components of the linear polarisation basis for RADARSAT-2 satellite..... 48

Figure 23: Coherence values of HH (left) and HV (right) components of the linear polarisation basis for RADARSAT-2 satellite. 95% of pixels lie between a range of coherence value 0.01 and 0.44 for both HH and HV polarisation combination. 49

Figure 24: Left: Coherence values of VV component of the linear polarisation basis for RADARSAT-2 satellite. Range of coherence is between 0.02 and 0.45 for this polarisation combination. Right: RGB composite image for interpretation of the different scatterings in linear polarisation basis, with red representing the double bounce scattering (HH), green representing the volumetric scattering (HV) and blue representing the surface scattering (VV)..... 50

Figure 25: Histogram showing frequency of various components of linear polarisation basis with their coherence values for RADARSAT-2. Red represents HH, green represents HV, and blue represents VV. 50

Figure 26: Subset of left: coherence values of VV component of the linear polarisation basis for RADARSAT-2 satellite, and right: RGB composite image of linear polarisation basis. Red: double bounce scattering, Green: volumetric scattering, Blue: surface scattering. Features such as the forests of Manali, Manali city, Apple orchards in the city are clearly visible in RGB image.	51
Figure 27: Coherence values of HH+VV (left), with 95% of pixels within the range of 0.02 and 0.46 coherence, and HV+VH (right), with 95% of pixels within the range of 0.01 and 0.43 coherence, components of the Pauli polarisation basis for RADARSAT-2 satellite.....	52
Figure 28: Subset of coherence values of HH+VV (left) and HV+VH (right) components of the Pauli polarisation basis for RADARSAT-2 satellite.....	52
Figure 29: Left: Coherence values of HH-VV, with 95% of pixels within 0.01 and 0.4 coherence value, component of the Pauli polarisation basis for RADARSAT-2 satellite. Right: RGB composite image for interpretation of the different scatterings in Pauli polarisation basis, with red representing HH-VV, blue representing HH+VV, and green representing HV+VH.	53
Figure 30: Subset of left: coherence values of HH-VV component of the Pauli polarisation basis for RADARSAT-2 satellite, and right: RGB composite image of Pauli polarisation basis. The main difference with the linear basis RGB composite is that this has higher surface scattering component (in blue colour).	53
Figure 31: Histogram showing frequency of various components of Pauli polarisation basis with their coherence values for RADARSAT-2. Red represents HH-VV, green represents HV+VH, and blue represents HH+VV.....	54
Figure 32: Coherence values of LL (left), with 95% of pixels within the range of 0.01 and 0.41 coherence, and LR (right), with 95% of pixels within the range of 0.02 and 0.46 coherence, components of the circular polarisation basis for RADARSAT-2 satellite.....	55
Figure 33: Histogram showing frequency of various components of circular polarisation basis with their coherence values for RADARSAT-2. Red represents LL, green represents LR, and blue represents RR. .	55
Figure 34: Left: Coherence values of RR, with 95% of pixels within 0.02 and 0.41 coherence value, component of the circular polarisation basis for RADARSAT-2 satellite. Right: RGB composite image for interpretation of the different scatterings in circular polarisation basis, with red representing LL, blue representing RR, and green representing LR.	56
Figure 35: Coherence values of Opt1 (left), with 95% of pixels within the range of 0.34 and 0.7 coherence, and Opt2 (right), with 95% of pixels within the range of 0.15 and 0.49 coherence, components of the optimal polarisation basis for RADARSAT-2 satellite.....	57
Figure 36: Histogram showing frequency of various components of optimal polarisation basis with their coherence values for RADARSAT-2. Red represents Opt1, green represents Opt2, and blue represents Opt3.....	57
Figure 37: Left: Coherence values of Opt3, with 95% of pixels within 0.012 and 0.256 coherence value, component of the optimal polarisation basis for RADARSAT-2 satellite. Right: RGB composite image for	

interpretation of the different scatterings in optimal polarisation basis, with red representing Opt1, blue representing Opt3, and green representing Opt2..... 58

Figure 38: Coherence values of HH (i), HV (ii), and VV (iii) components of the linear polarisation basis for ALOS-2 satellite. 95% of pixels lie between a range of coherence value 0 and 0.38, 0 and 0.39, and 0 and 0.4, for HH, HV, and VV polarisation combination. RGC composite image (iv) for interpretation of the different scatterings in linear polarisation basis, with red representing the double bounce scattering (HH), green representing the volumetric scattering (HV) and blue representing the surface scattering (VV)..... 59

Figure 39: Histogram showing frequency of various components of linear polarisation basis with their coherence values for ALOS-2. Red represents HH, and green represents HV. 59

Figure 40: Coherence values of HH+VV (i), with 95% of pixels within the range of 0 and 0.37 coherence, HV+VH (ii), with 95% of pixels within the range of 0 and 0.39 coherence, HH-VV (iii), with 95% of pixels within 0 and 0.36 coherence value and components of the Pauli polarisation basis for ALOS-2 satellite. RGB composite image (iv) for interpretation of the different scatterings in Pauli polarisation basis, with red representing HH-VV, blue representing HH+VV, and green representing HV+VH. 60

Figure 41: Histogram showing frequency of various components of Pauli polarisation basis with their coherence values for ALOS-2. Red represents HH-VV, and green represents HV+VH, and blue represent HH+VV. 60

Figure 42: Histogram showing frequency of various components of circular polarisation basis with their coherence values for ALOS-2. Red represents LL, and green represents LR, and blue represent RR. 61

Figure 43: Histogram showing frequency of various components of optimal polarisation basis with their coherence values for ALOS-2. Red represents Opt1, and green represents Opt2, and blue represent Opt3. 61

Figure 44: Height map of the Manali forest using (i) TSI technique (ii) CAI technique, on RADARSAT-2 data. 63

Figure 45: Height map of the Manali forest using (i) TSI technique (ii) CAI technique, on ALOS-2 data. 63

Figure 46: Height map of the Manali forest using (i) TSI technique (ii) CAI technique, on TerraSAR-X data. 64

Figure 47: Plot showing the relation between the estimated forest height using TSI technique on RADARSAT-2 data and the field calculated height. The yellow line is the 45° angle line, while the blue line is the trend line..... 65

Figure 48: Plot showing the relation between the estimated forest height using CAI technique on RADARSAT-2 data and the field calculated height. As per the points, the model seemed to have overestimated the height. 66

Figure 49: Plot showing the relation between the estimated forest height using TSI technique on ALOS-2 data and the field calculated height. 66

Figure 50: Plot showing the relation between the estimated forest height using CAI technique on ALOS-2 data and the field calculated height.	67
Figure 51: Plot showing the relation between the estimated forest height using TSI technique on TerraSAR-X data and the field calculated height. All the points closer to the yellow line denotes the high accuracy of the model derived height.	67
Figure 52: Plot showing the relation between the estimated forest height using CAI technique on TerraSAR-X data and the field calculated height. Again, the CAI technique seemed to have overestimated the height of trees.	68
Figure 53: GEDI derived forest canopy height map of the year 2019. Downloaded from the authorised GEDI page, subset was taken using vector data in QGIS software.	68
Figure 54: Plot showing the relation between the estimated forest height using TSI technique on RADARSAT-2 data and the GEDI derived height data.	69
Figure 55: Plot showing the relation between the estimated forest height using CAI technique on RADARSAT-2 data and the GEDI derived height data.	69
Figure 56: Plot showing the relation between the estimated forest height using TSI technique on ALOS-2 data and the GEDI derived height data.	70
Figure 57: Plot showing the relation between the estimated forest height using CAI technique on ALOS-2 data and the GEDI derived height data.	70
Figure 58: Plot showing the relation between the estimated forest height using TSI technique on TerraSAR-X data and the GEDI derived height data.	71
Figure 59: Plot showing the relation between the estimated forest height using CAI technique on TerraSAR-X data and the GEDI derived height data.	71
Figure 60: Plot showing the relation between the GEDI derived height data and the field calculated height data. The plot clearly shows the underestimated height of GEDI product, Global Forest Canopy Height map 2019.	72

LIST OF TABLES

Table 1: Parameters of the dataset used in this study.....	34
Table 2: Parameters of RADARSAT-2 satellite.....	47
Table 3: Parameters of ALOS-2 satellite.....	47
Table 4: Parameters of TerraSAR-X data.....	48
Table 5: Observation of TSI derived forest heights of the 3 satellites when validated with field values....	74
Table 6: Observation of CAI derived forest heights of the 3 satellites when validated with field values...	74

1. INTRODUCTION

Forests play a vital role in managing the ecology of the earth. They regulate the ecosystem in such a manner that all the life on earth is provided with the necessities of survival. Since the time of industrialization, poor planning has led to the degradation of many natural resources. One such resource humans have often disregarded is the forest area, until recently when scientists carried out studies and showed repercussions of deforestation. Because of the rapid migration from the hills and being a ‘counter magnet’ of Delhi, the population of Dehradun city increased manifold (Deep & Kushwaha, 2020) in the last two decades, with the forest area substituted by rapid urbanization. While Manali, a famous tourist spot has observed deforestation due to the indiscriminate construction of hotels (Kuniyal et al., 2003). Such activities adversely affect the environment with the release of carbon content, contributing to climate change.

Apart from deforestation which is a result of man-made activity, forest fires, and intense cyclones are some of the direct impacts of climate change that adversely affect the overall biomass content from an area. Therefore, it becomes the need of the hour to keep an estimate on the above ground biomass (AGB), whose main contribution is from the trees and soil. Among the various contributors of the biomass in a tree such as the density, diameter at breast height and tree height, the tree height is one of the main biophysical parameters of forests which can be obtained using laser scanning technology or a space-borne satellite system (Chen et al., 2021; Joshi & Kumar, 2017). While a handheld scanner accurately estimates the tree height individually, an airborne system such as Laser imaging, detection, and ranging (LiDAR) holds the advantage of obtaining data in a greater area at one time. But for the estimation of AGB, the diameter at breast height must also be known which can only be estimated using in-situ observations. Contrary to an airborne system, a spaceborne satellite system covers a bigger area, but usually has a coarser spatial resolution.

In forestry applications, while the optical remote sensing suffices when studying about the forest canopy and its extent, microwave remote sensing is required to study the forest structure in depth (S. Kumar, 2009). Because of no or a very less atmospheric opacity, microwaves also have the tendency to penetrate most of the atmospheric particles, enabling it to gather data even in thick clouds and capture forest structure. The microwave region can be seen clearly in *figure 1*, where the lower wavelength bands such as the X band has the tendency to be interfered by various atmospheric particles. While longer wavelength bands such as C band and L band have almost no interference, enabling them to capture the forest structure through the canopy.

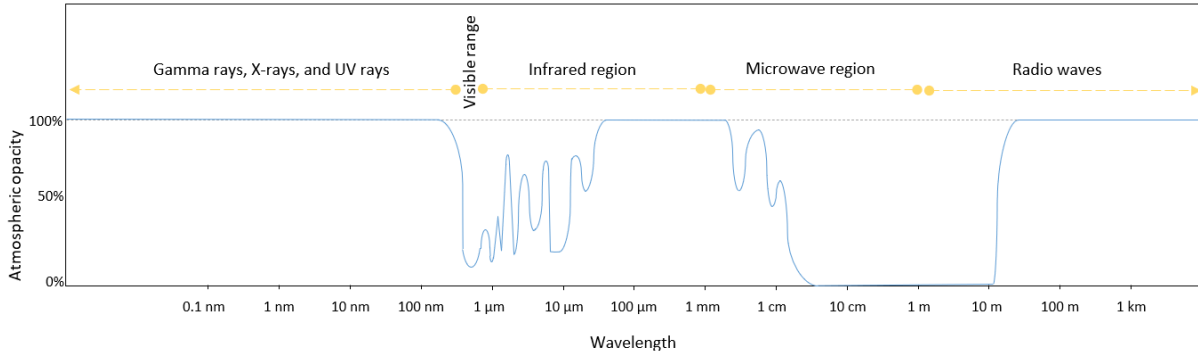


Figure 1: Shows the interference of atmospheric particles on the wavelength range of the electromagnetic spectrum, with an emphasis on the visible range and microwave range. (DePasquale et al., 2015)

1.1. Background

Radio Detection and Ranging (Radar) is a part of the microwave region of the spectrum, which works with the signals emitting from the transmitter, with the speed of light. The time is noted when the backscattered signal is detected at the receiver (Skolnik, n.d.), which usually is present at the same location as the transmitter, and is further used to calculate the range of the target from the sensor. Based on the placement of the transmitter and receiver, the system is divided into two classes, monostatic or bistatic system, where monostatic is defined by the co-existence of the transmitter and receiver, and bistatic is defined by both being present at different locations. Synthetic Aperture Radar (SAR) is a type of Radar used in various applications ranging from oil spill detection to obtaining the bio-physical parameters of the forests.

The in-situ method for forest height estimation is performed using handheld hypsometers which use clinometers for measuring the angle, and rangefinders for measuring the distance between the device and target. This method gives the highest accuracy in estimating forest height but is very time-consuming. To overcome this, remote sensing was introduced which covered a larger area at a given time. Airborne remote sensing platform which uses LiDAR is used for obtaining the forest height but is susceptible to atmospheric effects such as rain, fog, and snow. A LiDAR works in the infrared region of the electromagnetic spectrum with a wavelength range between 0.9 and 1.5 μm . Another way of calculating the forest height is by using a SAR sensor, which could work in both airborne and space-borne systems. A SAR sensor works in the microwave region of the electromagnetic spectrum and has various wavelength ranges corresponding to different bands. With a higher wavelength than LiDAR, the ability of SAR sensors to penetrate surfaces and objects increases. Just like LiDAR, a SAR sensor is independent of Sun's light energy, enabling it to capture data at any time. The main advantage of using a space-borne SAR sensor, apart from having greater coverage, is that the atmospheric particles do not interfere in the signals, as seen in *figure 1*, and hence data is acquired in any weather conditions. Though an airborne sensor has a lesser coverage area, it has a higher Signal to Noise ratio (SNR), and a better temporal and spatial resolution as compared to the space-borne sensor (S. Lee, 2013).

The first satellite with a SAR system was the Seasat, launched in the year 1978, with an L band radar (*NASA-JPL: Seasat*, n.d.). Since then, many SAR satellites have been launched by various government space agencies

such as NASA, ISRO, JAXA, ESA etc. While all the satellites had a single frequency SAR system on the satellite, the NASA-ISRO Synthetic Aperture Radar (NISAR) project will launch the first spaceborne satellite with two radars, one of the L band frequency and the other of S band frequency (*NASA-JPL: NISAR Mission*, n.d.). The mission is planned to be launched in the year 2023. Based on wavelength, while some studies related to forest height or forest biomass used a higher wavelength band data such as P band or L band (Asopa & Kumar, 2020; Kugler et al., 2015; Papathanassiou & Cloude, 2001), other studies used lower wavelength X or C band data (Chandola et al., 2014; S. Kumar et al., 2017; Mukhopadhyay et al., 2021).

For the estimation of forest height, various techniques in SAR were introduced with each having its merits. Polarimetric SAR (PolSAR), with its polarization combinations, is useful in extracting different scattering patterns of a target, which helps in determining its physical properties such as structure, size, dielectric property, and orientation (Khatai & Kumar, 2014). Interferometric SAR (InSAR), another technique of SAR, is useful in determining the exact location of the target. With elevation information from the top of the canopy and ground, forest height could be estimated using the InSAR technique (P. Kumar & Krishna, 2019). Polarimetric SAR Interferometry (PolInSAR) is the latest amongst all which combines the merits of both PolSAR and InSAR (Shane R Cloude, 2005, 2006), where accurate positional information is retrieved for different types of scatterers. Inversion models such as the Random Volume over Ground (RVoG) have been used (Aghabalaei et al., 2020; Babu & Kumar, 2018) in the past studies to derive the forest height. Other models such as the TSI and CAI have also been implied (Joshi & Kumar, 2017; S. Kumar et al., 2017) by various authors in their study. Some of them are explained in detail in the following sections.

1.2. Motivation

This study focuses on retrieving forest height using multi-frequency SAR data with the PolInSAR technique. TerraSAR-X satellite data is used which has the sensor working in X band of the spectrum, RADARSAT-2 satellite data is also used which has a C band sensor, and the third satellite used in the study is ALOS-2 PALSAR-2, which has an L band sensor. Various algorithms, both for airborne and space-borne systems, have been derived in the past for the estimation of forest height (Attema & Ulaby, 1978; S R Cloude & Papathanassiou, 2003). While most of the studies focused on the use of airborne data, comparatively, a fewer number of studies used spaceborne data.

Vertical wavenumber, denoted by k_z , plays an important role in estimating the forest height since it related the interferometric phase with the height of the scatterers (Ghosh et al., 2018; Khatai & Kumar, 2014). Baseline, slant range, wavelength of the signals, and incidence angles of the image pairs determine the value of k_z . This value comes with a constraint that it should neither be too high, nor be too low as a higher value would saturate the coherence for some heights, and a lower value would not let the coherence segregate the height (Ghosh et al., 2018; Kugler et al., 2015). Since the other values are fixed by the sensor, only the

baseline component can be altered to get the desired value of k_z . The step, known as the baseline simulation, is an important step where using the height of ambiguity, the baseline component is obtained.

Forest height, which is one of the biophysical parameters of the forest, is an important parameter that is useful in determining the above ground biomass present in the atmosphere. The need to study this is utmost in the current scenario where global temperatures are rising, giving birth to several dormant calamities such as rise in sea level, super storms, hurricanes, and forest wildfires. Release of carbon into the environment, which leads to these problems, must be studied to estimate their total quantity and the carbon sequestration that would happen upon deforestation. So, the estimation of forest height is an important step in determining the total Above ground biomass present in a forest. In the world of remote sensing, it becomes quite easy to estimate that using appropriate data and softwares. SAR data is thus used in this study to determine accurate forest height in the Manali forest ranges, Ram Bagh, and Van Vihar.

1.3. Research Objective

The main objective of the study is to estimate the height of the forest in Manali city using inversion models, with PolInSAR data of three satellites, TerraSAR-X with X band frequency, RADARSAT-2 with C band frequency, and ALOS-2 PALSAR-2 with L band frequency. The study also concludes which inversion model amongst the TSI, and CAI is best suited for obtaining the forest height. The validation of the results is from the field values and GEDI product, the forest canopy height map, which will tell us if spaceborne LiDAR system a good alternative to field visits.

1.3.1. Sub-objectives of the study

- i. To estimate the forest height using different frequency band data and compare their results.
- ii. To estimate the baseline component and generate the vertical wavenumber file.
- iii. To study the results obtained using Three Stage Inversion and Coherence Amplitude Inversion methods, and comment on the accuracy of the modelled height.
- iv. To compare the GEDI product, the Global Forest Canopy Height map of the year 2019 with the field data and determine whether the GEDI product is suitable for analysing the forest height parameters.

1.3.2. Research questions to be addressed

- i. Which frequency band data amongst the three is best suited for obtaining the forest height?
- ii. For different backscatter components, how the complex coherences differ for various polarisation basis?
- iii. Amongst the TSI and CAI models, which model should be preferred for the estimation of forest height using PolInSAR technique?
- iv. How much is the accuracy obtained of the estimated forest height using both the models with respect to the field data?

- v. Is the GEDI product, the forest canopy height map, a good alternative to field values for validation of the results?

2. LITERATURE REVIEW

This section consists of a brief history about SAR, and various methods implied for obtaining forest heights using remotely sensed SAR data. Also explained in the section is the current scenario of various SAR techniques being studied for the estimation of forest height, and the procedure followed from generation of Scattering matrix to Pauli basis, to coherence matrix, to estimation of baseline and its use in generation of vertical wavenumber, till the application of inversion models. Apart from that, a brief explanation of the working of a few inversion models have been demonstrated too.

2.1. Relation of forest with the biomass

Forests have been used by every being on earth, be it humans, animals, or plants for their survival. Apart from their direct usage in terms of wood, fuel, paper, and fodder, they have other indirect uses as well that helps in maintaining the ecosystem. One of the indirect usages of forest is that it stores within it three quarters of carbon in plants and about 40% of the soil carbon (Gorte & Sheikh, 2010), helping in maintaining the temperature of the planet. Forest carbon stocks consists of Below Ground Biomass (BGB), Above Ground Biomass (AGB), litter, dead wood, and soil until a depth of 100 cm (*Forest Carbon Stock*, n.d.). All the parts of trees such as the foliage, trunk, stem, and branches contribute to the total carbon content. Over the years for human need or due to natural calamities such as forest fires, trees have been cut or burned, which releases the carbon stored within it in the form of carbon di oxide and other trace gases (Brown, 1997). Studies have found a direct relation between deforestation and climate change with the fact that released carbon led to a rise in temperature of the planet over the years (Gorte & Sheikh, 2010; Shukla et al., 1990). Therefore, it is necessary to calculate the AGB, for studying the amount of carbon present, in all the forests so that measures to reduce unlawful deterioration of forests could be taken and implemented at the global level. For AGB estimation, forest height along with the diameter at breast height and the density are required, while this study focuses on estimating the forest height using PolInSAR technique for three different frequency pair of data.

2.2. Methods used in estimating the forest height

Various studies in the past have estimated the AGB using allometric equations (T Mette et al., 2004), for which correct estimation of forest height, which is a forest biophysical parameter, is very important. Since the inclusion of remote sensing and GIS in the world of science, it has become cost efficient and less time consuming to gather data and monitor it for a period. In-situ methods are only used for validation of the results (Minguez et al., 2001) obtained from algorithms and models applied on remotely sensed data. Also,

the in-situ does not work at nighttime when there is a lack of sunlight, while the other remotely sensed is either in LiDAR or SAR, both of which are active sensors and may gather data at any time, regardless of the sunlight. Just like accuracy assessment is performed after classification of satellite data in Optical remote sensing, validation is performed by selecting few sample trees whose height values are compared with the estimated tree height obtained using model. The degree of overestimation or underestimation explains the performance of the model.

Because of the large distance of the spaceborne system from earth as compared to an airborne system, electromagnetic waves that travel from the sensor to earth, and then back to sensor, interacts with many particles on the way and gets attenuated. Thus, the SNR is lower in spaceborne sensors than their airborne counterparts. Apart from a high SNR in an airborne system, the temporal decorrelation, which occurs in the image pairs due to changes in the area because of the time gap between the image acquisitions, is very low in these system as compared to a spaceborne system, which is why most of the studies preferred to use airborne data (Shane Robert Cloude & Papathanassiou, 1998; Hajnsek et al., 2009; Tobias Mette et al., 2002) than spaceborne data (Krieger et al., 2005). Another reasons why they are preferred is because of their better spatial resolution (S. Lee, 2013).

Studies related with airborne system used the LiDAR system as well for estimation of forest height (Li et al., 2019). They used the properties of laser scanning and Digital Surface Model (DTM) where the backscattered signals from the top of the canopy were utilized, while the Digital Terrain Model (DTM) was subtracted from the modelled height map, giving an estimation of the forest height. Most of the LiDAR system works in the infrared region with a wavelength of 0.9-1.5 μm . Due to a lesser wavelength, the signals are unable to penetrate through suspended air particles and are susceptible to atmospheric interactions. With a higher wavelength range than infrared region, microwave region dominates which is further divided into bands. The main bands used in satellites or airborne systems are X band with a wavelength range of 2.5-3.75 cm and frequency range of 8-12 GHz, C band with a wavelength range of 3.75-7.5 cm and frequency range of 4-8 GHz, and L band with a wavelength range of 15-30 cm and frequency range of 1-2 GHz.

2.3. Working of Synthetic Aperture Radar in brief

SAR is a form of RADAR which is used in remote sensing, and it differs from a normal optical remote sensing satellite in numerous ways, one of which is the side looking property of the SAR system. While the optical remote sensing satellites usually have a nadir looking transmitter, the SAR has a side looking transmitter to avoid a left-right ambiguity, as a nadir looking RADAR system will have a pair of equidistant pixels from the receiver at each position of the satellite and an ambiguity may arise in determining whose backscattered information is received at the receiver. Unlike optical remote sensing which has one spatial resolution, SAR remote sensing has two resolutions, the azimuth and range resolution. The ability of a radar system to differentiate between adjacent scatterers in the direction parallel to the system defines the azimuth resolution, while the ability to differentiate between adjacent scatterers in the perpendicular direction of the system defines the range resolution.

$$R_a = \frac{H \cdot \lambda}{L \cdot \cos \theta} \quad (2.1)$$

$$R_r = \frac{c \cdot \tau}{2 \cdot \sin \theta} \quad (2.2)$$

Here; R_a and R_r are the azimuth and range resolution, respectively,

H is the sensor height,

λ is the wavelength of the transmitted wave,

L is the geometric length of the antenna,

θ is the angle of incidence,

c is the speed of light, 2.99×10^8 m/s, and

τ is the pulse duration of transmitter.

The equations 2.1 and 2.2 shows the dependency of azimuth resolution on the antenna length, wavelength of the band used in the platform, and the height of the platform, while the range resolution depends upon Pulse width time. For a higher azimuth resolution, the length of the aperture must be very high which is possible in SAR because of the high speed of the platform due to which an antenna of normal length virtually seems like a very long antenna.

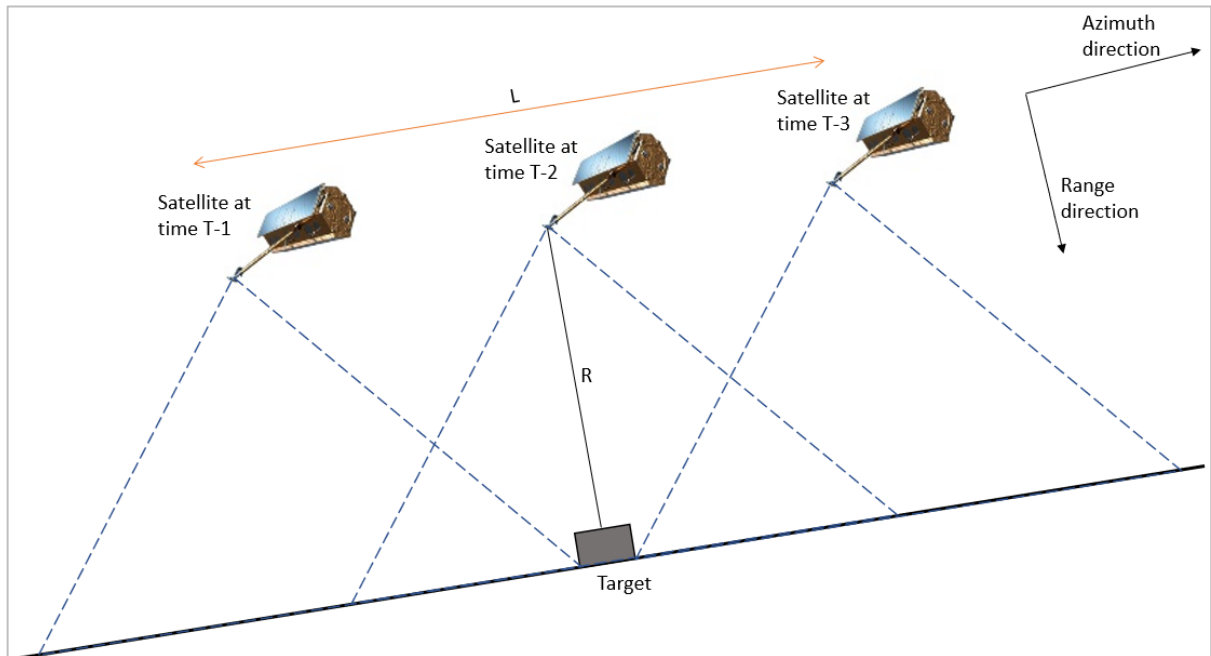


Figure 2: Backscattered information of target is equal to combination of all backscattered information gathered from the target in between time T-1 and T-3, elongating the length of aperture virtually, and improving the azimuth resolution.

Figure 2, which is a side view of the SAR demonstration, explains how in SAR, a higher azimuth resolution is obtained using virtually longer antenna length. This also illustrates the procedure of gathering backscattered information from a target pixel. Information from target on ground is backscattered as satellite reaches a point at time T-1. The information is gathered until satellite reaches another point at time T-3,

when there is no backscatter from that target location. Between time $T-1$ and $T-3$, the platform travelled a distance L , which is the virtual length of antenna, and is used to calculate the azimuth resolution.

The front view of a model of SAR explains some useful parameters. *Figure 3* shows an aircraft transmitting wave signals from the sensor towards ground. The waves get transmitted at different angle of depression, which enables the system to determine the pixel whose backscattered energy is received at the receiver. Angle of depression at two extreme ends defines the near and far range. While the highest value of angle of depression defines near range, the lowest value of angle of depression defines the far range of the SAR system. When the transmitted signal detects Object 1, signals containing information about the scatterer retrace back at the receiver end. The time taken by the signal to return is then used to determine the distance of the object from sensor, and hence the position of it is ascertained. Along with different polarizations in the wave, horizontal or vertical, properties of the object, such as shape, size, or orientation is determined (Khatai & Kumar, 2014).

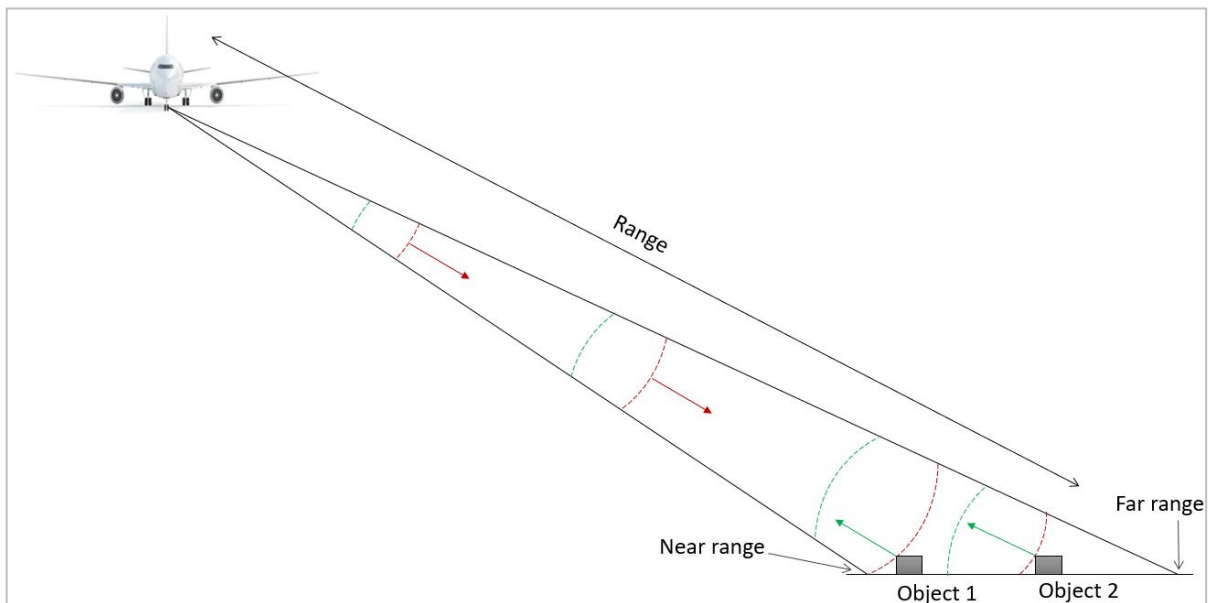


Figure 3: Front view of how a SAR sensor gathers data. Transmitted signal wave is red in colour, while backscattered signals are shown in green colour. Side looking property of sensor overcomes the left-right ambiguity of a nadir looking SAR sensor. As a result, wave reaches and backscatters from Object 1 earlier than Object 2, enabling it to be identified as the object closer to the sensor.

2.4. Advanced SAR techniques for forest height retrieval

For estimating forest height using remotely sensed data of a SAR sensor, mainly three advanced techniques were incorporated, Polarimetric SAR (PolSAR), Interferometric SAR (InSAR), and Polarimetric SAR Interferometry (PolInSAR). While PolSAR used polarization combinations to extract different scattering patterns of targets, helping in estimating their orientation, shape, size, and dielectric property, InSAR coherently combined signals from two different locations to accurately locate the target pixel under consideration. PolInSAR combined the advantages of both techniques (Shane R Cloude, 2005, 2006) and

used them to estimate forest height with a much higher accuracy. Another technique which has been used for forest height estimation is tomography (Aghababaei et al., 2020; Asopa & Kumar, 2020; Minh et al., 2014) where multiple datasets of the same area is obtained from different locations, making it a multi baseline system.

2.4.1. Estimation of forest height using PolInSAR technique

Each pulse, or wave transmitting through the SAR sensor in airborne or spaceborne platform consist of polarization. There are 3 possible polarization combinations in SAR data: single, dual and quad-polarization. A pulse consists of either a vertical or a horizontal polarization, which may or may not change upon interaction with targets, giving us four possible cases: HH, HV, VH, and VV. Here, HH symbolize the wave has got horizontal polarization and after interaction with the target, it retains the same polarization state. Similarly, HV symbolize the wave has got vertical (V) polarization while emitting from the sensor but upon interaction with the target, the state of polarization changes to horizontal (H). Thus, data can be in combination of these 4 types of polarization states, with single polarized data may have either HH, or HV, or VH, or VV sensing ability. With presence of more polarization combinations in the data, more scattering patterns of the target pixels may be extracted, helping in determining various target properties such as their size, shape, and orientation. The data used in the study is a quad polarized data and hence may detect all the four types of polarization states.

Various studies in the past have used PolSAR data for estimating forest height (Shane Robert Cloude & Papathanassiou, 1998). Although the authors have used the concept of PolInSAR, the data used is a Polarimetric SAR data while the Interferometric section includes another PolSAR data with a baseline for accurate estimation of the location of the scatterer.

2.4.2. Forest height retrieval using InSAR technique

Studies have also used the InSAR technique to estimate the height of forest (P. Kumar & Krishna, 2019). Authors used the principle of Digital Elevation Model (DEM) differencing by generating a Digital Surface Model (DSM) of the canopy top of the forest and subtracting the DEM, which was obtained using backscattered information from ground through canopy gaps. But this technique could fail where a dense canopy is present, and the penetration is minimal, rendering it difficult for the system to generate accurate DEM. Usually single polarization set is present in InSAR studies and hence there is not much information about the scatterers. InSAR uses the concept of baseline to capture data, with mainly two types of baselines. Spatial baseline is the distance between the positions of satellite sensors at the time of respective data acquisition of the same area. Temporal baseline on the other hand is the difference between the data acquisition of the image pair in terms of number of days. The concept of baseline is further used in PolInSAR technique.

2.4.3. PolInSAR technique for forest height retrieval

Many studies used PolInSAR technique for obtaining the forest height (S. Kumar et al., 2020) as it provided better accuracy and better information. Spatial resolution is one of the most important parameters in remote sensing. A higher spatial resolution, meaning a lower value, is of much importance as detailed information can be gathered as compared to an image with a low spatial resolution, which tends to lose information. This is because within a cell, the feature with the maximum backscattered information is shown, ignoring the presence of other features. But in SAR, using Polarimetry, information using different polarization sets such as HH, HV, VH, and VV were able to identify multiple features within a single resolution cell. But because of single dataset, the idea accurate depth information was not available. Hence, Interferometry was introduced along with Polarimetry, making the technique as PolInSAR. With InSAR component, it became much accurate in estimating the depth and the location of the scatterer. The working of the same is explained in the following sections.

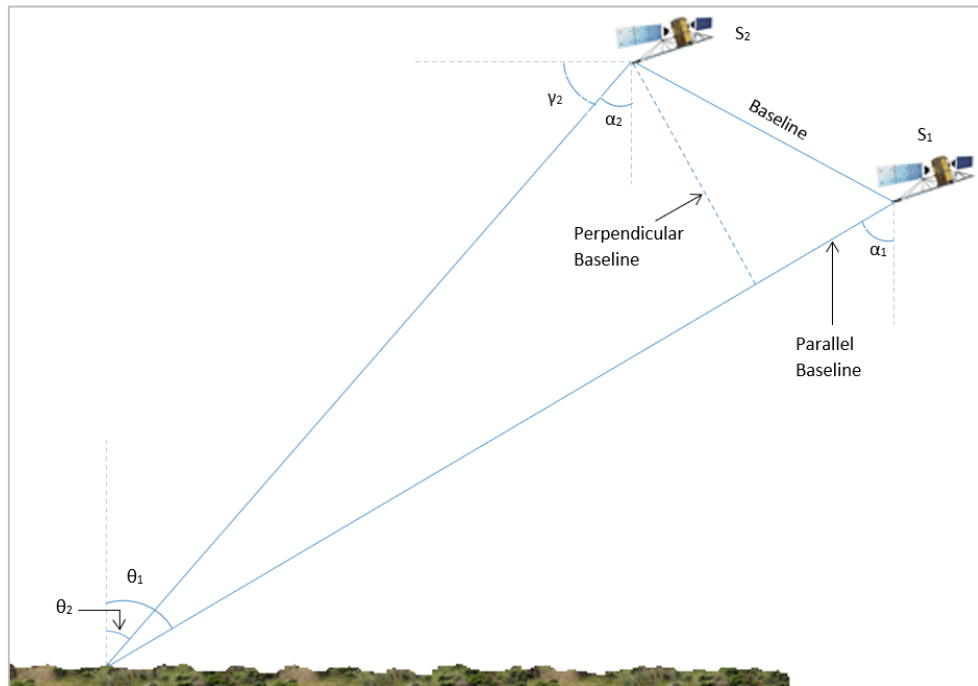


Figure 4: Shows the working of InSAR (PolInSAR in case of Polarimetric data). Data acquisition from different locations generates a baseline useful in estimating vertical structures accurately.

For clear understanding, a point pixel is shown in *figure 4*. The angle which the transmitted signal makes with the horizontal line parallel to the ground is known as the angle of depression, depicted by γ_2 . While the angle made by the signal with the normal at the point of contact is known as the angle of incidence, depicted by θ . Also, there is another angle in consideration, the look angle depicted by α , which is the angle between the transmitted signal and the vertical nadir point at the satellite position. If the surface is flat and there is no angular projection, the look angle and the angle of incidence equates.

Here, we assume that the system has quad polarization, and hence will be able to gather more information using the four types of polarization states. Although, the system may also have single or dual polarization

states. Satellite in its first path gathered backscattered signals from the area. The information gets stored and is visualized as a scattering matrix (S) as a 2x2 matrix, as shown in *equation 2.3*. In the second path, the same satellite gathered backscattered signals from the same area, but with a baseline parameter which can be a spatial baseline, or a temporal baseline, or both. In spatial baseline, there are two subtypes, perpendicular and parallel baseline. The value of perpendicular baseline is very important as, higher the value of perpendicular baseline, more accurate heights of vertical structures are obtained (Ferretti et al., 2007). But a very high value of it increases the decorrelation noise artefacts (Pepe & Calo, 2017). The second satellite orbit path also generated a 2x2 scattering matrix. These scattering matrices depict the relationship between the transmitted signal waves and the backscattered signal wave (Jin & Xu, 2013). A normal 2X2 scattering matrix with the polarization sets is shown in the *equation 2.3*. Information of the scattering process and the scatterer is present in the scattering matrix (Shane R Cloude, 2005).

$$S = \begin{bmatrix} S_{HH} & S_{HV} \\ S_{VH} & S_{VV} \end{bmatrix} \quad (2.3)$$

Upon interaction with various elements, a shift gets induced in the Polarization Orientation Angle (POA), which will be explained in further section, which must be compensated for obtaining an accurate result. Previous studies explained the requirement of de-orientation, the process of compensating for the shift induced in POA (Khatai & Kumar, 2014). In the nomenclature of the PolInSAR field data, the set of data are known as primary and secondary data, or master and slave data, whose scattering matrices are depicted by S_1 and S_2 , respectively.

After generation of the scattering matrices, feature vectors are generated which may either be the Pauli feature vector (K_4^P) or the Lexicographic feature vector (K_4^L). They are the first order derivative of the scattering matrix and are generated by the Pauli spin matrix set $[\Psi_P]$, and the lexicographic basis $[\Psi_L]$, respectively (Shane Robert Cloude & Pottier, 1996; Jin & Xu, 2013). Further, these feature vectors are used to generate the coherence matrix or the covariance matrix, respectively, by the product of feature vectors with their conjugate transpose.

$$[\Psi_L] \equiv \left\{ 2 \begin{bmatrix} 1 & 0 \\ 0 & 0 \end{bmatrix} 2 \begin{bmatrix} 0 & 1 \\ 0 & 0 \end{bmatrix} 2 \begin{bmatrix} 0 & 0 \\ 1 & 0 \end{bmatrix} 2 \begin{bmatrix} 0 & 0 \\ 0 & 1 \end{bmatrix} \right\} \quad (2.4)$$

Equation 2.4 depicts the Lexicographic basis and is used to derive the Lexicographic feature vector (K_4^L).

$$K_4^L = [S_{HH} \ S_{HV} \ S_{VH} \ S_{VV}]^T \quad (2.5)$$

$$[C_4^L] = \langle K_4^L \cdot (K_4^L)^\dagger \rangle \quad (2.6)$$

The product of lexicographic feature vector and its conjugate transpose results into a 4x4 matrix, known as the covariance matrix, depicted by $[C_4^L]$. *Equation 2.7* shows the covariance matrix, where $\langle \dots \rangle$ depicts the ensemble averaging during data processing (Khatai & Kumar, 2014).

$$[C_4^L] = \begin{bmatrix} \langle |S_{HH}|^2 \rangle & \langle S_{HH}S_{HV}^\dagger \rangle & \langle S_{HH}S_{VH}^\dagger \rangle & \langle S_{HH}S_{VV}^\dagger \rangle \\ \langle S_{HV}S_{HH}^\dagger \rangle & \langle |S_{HV}|^2 \rangle & \langle S_{HV}S_{VH}^\dagger \rangle & \langle S_{HV}S_{VV}^\dagger \rangle \\ \langle S_{VH}S_{HH}^\dagger \rangle & \langle S_{VH}S_{HV}^\dagger \rangle & \langle |S_{VH}|^2 \rangle & \langle S_{VH}S_{VV}^\dagger \rangle \\ \langle S_{VV}S_{HH}^\dagger \rangle & \langle S_{VV}S_{HV}^\dagger \rangle & \langle S_{VV}S_{VH}^\dagger \rangle & \langle |S_{VV}|^2 \rangle \end{bmatrix} \quad (2.7)$$

Similarly, when Pauli basis is used for vectorization of the scattering matrix, following are the parameters which are used to generate the coherence matrix. *Equation 2.8* shows the Pauli spin matrix set, which generates the 4x1 Pauli feature vector as shown in *equation 2.9*.

$$[\Psi_P] \equiv \left\{ \sqrt{2} \begin{bmatrix} 1 & 0 \\ 0 & 1 \end{bmatrix} \sqrt{2} \begin{bmatrix} 1 & 0 \\ 0 & -1 \end{bmatrix} \sqrt{2} \begin{bmatrix} 0 & 1 \\ 1 & 0 \end{bmatrix} \sqrt{2} \begin{bmatrix} 0 & -j \\ j & 1 \end{bmatrix} \right\} \quad (2.8)$$

$$K_4^P = \frac{1}{\sqrt{2}} [S_{HH} + S_{VV} \quad S_{VV} - S_{HH} \quad S_{HV} + S_{VH} \quad j(S_{HV} - S_{VH})]^T \quad (2.9)$$

Product of the Pauli feature vector and its conjugate transpose generates the coherence matrix.

$$[T_4^P] = \langle K_4^P \cdot (K_4^P)^\dagger \rangle \quad (2.10)$$

But the coexistence of the transmitter and receiver makes the system a monostatic one, altering the equations due to a few assumptions, such as the backscattering reciprocity where $S_{HV} = S_{VH}$. With the assumption in play, the lexicographic feature vector changes into a 3x1 matrix as,

$$K_3^L = [S_{HH} \quad \sqrt{2}S_{HV} \quad S_{VV}]^T \quad (2.11)$$

Here, the effect of $S_{HV} + S_{VH}$ is normalized and the $\sqrt{2}$ component is obtained. Multiplication of this vector with its conjugate transpose generates a 3x3 covariance matrix $[C_3^L]$ as shown in *equation 2.12*.

$$[C_3^L] = \langle K_3^L \cdot (K_3^L)^\dagger \rangle = \begin{bmatrix} \langle |S_{HH}|^2 \rangle & \sqrt{2}\langle S_{HH}S_{HV}^\dagger \rangle & \langle S_{HH}S_{VV}^\dagger \rangle \\ \sqrt{2}\langle S_{HV}S_{HH}^\dagger \rangle & 2\langle |S_{HV}|^2 \rangle & \sqrt{2}\langle S_{HV}S_{VV}^\dagger \rangle \\ \langle S_{VV}S_{HH}^\dagger \rangle & \sqrt{2}\langle S_{VV}S_{HV}^\dagger \rangle & \langle |S_{VV}|^2 \rangle \end{bmatrix} \quad (2.12)$$

With the backscattering reciprocity condition, and using Pauli basis, the *equation 2.9* reduces to:

$$K_3^P = \frac{1}{\sqrt{2}} [S_{HH} + S_{VV} \quad S_{HH} - S_{VV} \quad 2S_{HV}]^T \quad (2.13)$$

A 3x3 coherence matrix $[T_3^P]$ gets generated when the 3x1 Pauli feature vector gets multiplied with its conjugate transpose.

$$[T_3^P] = \langle K_3^P \cdot (K_3^P)^\dagger \rangle = \frac{1}{2} \begin{bmatrix} \langle |S_{HH} + S_{VV}|^2 \rangle & \langle (S_{HH} + S_{VV})(S_{HH} - S_{VV})^\dagger \rangle & 2\langle (S_{HH} + S_{VV})S_{HV}^\dagger \rangle \\ \langle (S_{HH} + S_{VV})(S_{HH} - S_{VV})^\dagger \rangle & \langle |S_{HH} - S_{VV}|^2 \rangle & 2\langle (S_{HH} - S_{VV})S_{HV}^\dagger \rangle \\ 2\langle S_{HV}(S_{HH} + S_{VV})^\dagger \rangle & 2\langle S_{HV}(S_{HH} - S_{VV})^\dagger \rangle & 4\langle |S_{HV}|^2 \rangle \end{bmatrix} \quad (2.14)$$

$$[T] = \begin{bmatrix} T_{11} & T_{12} & T_{13} \\ T_{21} & T_{22} & T_{23} \\ T_{31} & T_{32} & T_{33} \end{bmatrix} \quad (2.15)$$

2.4.3.1. Polarisation Orientation Angle

Equation 2.15 is the depiction of the coherence matrix in the general form. Using this, coherence estimation is performed to collect information about the different scattering types. But studies in the past have emphasized on the usage of de-orientation step, to compensate for the shift induced in the Polarization Orientation Angle (POA) (Khati & Kumar, 2014). Upon interaction with different targets, a shift gets induced in the POA, which is the angle between semi major axis of the polarized wave and horizontal axis along the line of sight. The same is shown in figure 5.

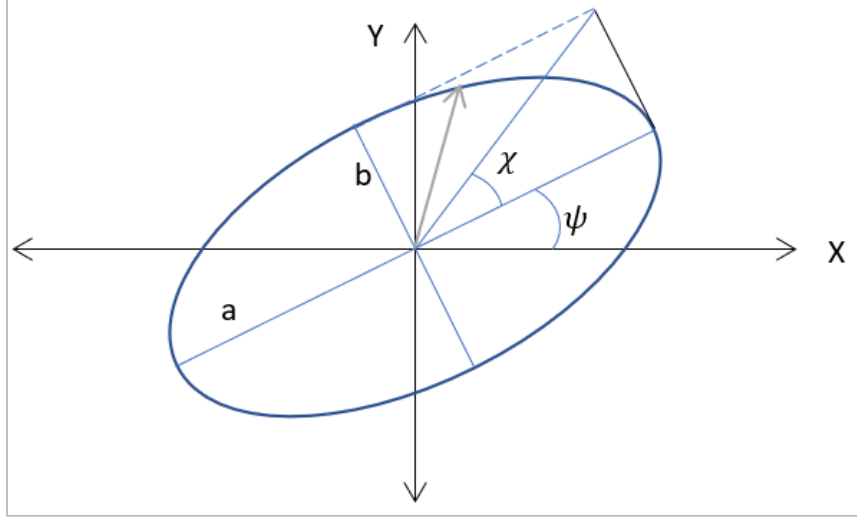


Figure 5: Polarization ellipse is shown in the image. Upon interaction with various features, the POA, denoted by ψ in this figure, changes, altering the power of various scattering types.

In this illustration of Polarization ellipse, the semi major axis is denoted by 'a', while the semi minor axis is denoted by 'b'. The ellipticity angle is denoted by 'χ', while 'ψ' denotes the Polarization Orientation Angle. The total shift is denoted by θ and is equal to.

$$\theta = \frac{1}{4} \left[\tan^{-1} \left(\frac{2R_e(T_{23})}{T_{22} - T_{33}} \right) + \pi \right] \quad (2.16)$$

$$\theta = \frac{1}{4} \left[\tan^{-1} \left(\frac{-4R_e(\langle (S_{HH} - S_{VV})S_{HV}^* \rangle)}{-\langle |S_{HH} - S_{VV}|^2 \rangle + 4\langle |S_{HV}|^2 \rangle} \right) + \pi \right] \quad (2.17)$$

The process of compensation of the total shift, so that the resultant has zero shift, is known as de-orientation. Equations below shows the coherence matrix, generated without a shift, where $[U]$ is the rotation matrix used to compensate for the shift. The final coherence matrix $[\bar{T}]$ has zero shift (Khati & Kumar, 2014).

$$[\bar{T}] = [U][T][U^T] \quad (2.18)$$

$$[U] = \begin{bmatrix} 1 & 0 & 0 \\ 0 & \cos 2\theta & \sin 2\theta \\ 0 & -\sin 2\theta & \cos 2\theta \end{bmatrix} \quad (2.19)$$

It has been observed that the shift induced in POA increases the power of volumetric scattering and decreases the power of double bounce scattering (J. Lee et al., 2011). Some contradictory observations were

made by Khati (Khati & Kumar, 2014), where double bounce scattering power was increasing, and volumetric scattering power was decreasing. Though the study strongly suggested the use of de-orientation step to overcome the shift induced. The study also mentioned that it was not necessary to perform the step for PolInSAR data. Hence, this step was bypassed in this study.

2.4.3.2. PolInSAR T6 Coherency matrix

However, in the concept of PolInSAR, the coherence matrix is a 6x6 matrix T_6 , and denoted as in the below equations. It is generated by the product of scattering vector k_1 and k_2 of the Pauli basis (Shane Robert Cloude & Papathanassiou, 1998; Khati & Kumar, 2014).

$$T_6 = \langle \begin{bmatrix} k_1 \\ k_2 \end{bmatrix} \begin{bmatrix} k_1^\dagger & k_2^\dagger \end{bmatrix} \rangle = \begin{bmatrix} [T_{11}] & [\Omega_{12}] \\ [\Omega_{12}]^\dagger & [T_{22}] \end{bmatrix} \quad (2.20)$$

Where, k_1 and k_2 are the scattering vectors of the Pauli basis of the first and second satellite passes, respectively, both of which are defined below in *equations 2.21 and 2.22*. In the *equation 2.20*, k_1^\dagger depicts the conjugate transpose of k_1 , while k_2^\dagger depicts the conjugate transpose of k_2 .

$$k_1 = [S_{hh}^1 + S_{vv}^1 \quad S_{hh}^1 - S_{vv}^1 \quad 2S_{hv}^1]^T \quad (2.21)$$

$$k_2 = [S_{hh}^2 + S_{vv}^2 \quad S_{hh}^2 - S_{vv}^2 \quad 2S_{hv}^2]^T \quad (2.22)$$

So, the final T_6 coherency matrix is formed as in *equation 2.23*. Here, * denotes the conjugate value.

$$[T_6] = \begin{bmatrix} S_{hh}^1 + S_{vv}^1 \\ S_{hh}^1 - S_{vv}^1 \\ 2S_{hv}^1 \\ S_{hh}^2 + S_{vv}^2 \\ S_{hh}^2 - S_{vv}^2 \\ 2S_{hv}^2 \end{bmatrix} \begin{bmatrix} [S_{hh}^1* + S_{vv}^1* & S_{hh}^1* - S_{vv}^1* & 2S_{hv}^1* & S_{hh}^2* + S_{vv}^2* & S_{hh}^2* - S_{vv}^2* & 2S_{hv}^2*] \end{bmatrix} \quad (2.23)$$

$$[T_{11}] = \begin{bmatrix} \langle |S_{hh}^1 + S_{vv}^1|^2 \rangle & \langle (S_{hh}^1 + S_{vv}^1)(S_{hh}^1 - S_{vv}^1)^* \rangle & 2\langle (S_{hh}^1 + S_{vv}^1)S_{hv}^1* \rangle \\ \langle (S_{hh}^1 - S_{vv}^1)(S_{hh}^1 + S_{vv}^1)^* \rangle & \langle |S_{hh}^1 - S_{vv}^1|^2 \rangle & 2\langle (S_{hh}^1 - S_{vv}^1)S_{hv}^1* \rangle \\ 2\langle S_{hv}^1(S_{hh}^1 + S_{vv}^1)^* \rangle & 2\langle S_{hv}^1(S_{hh}^1 - S_{vv}^1)^* \rangle & \langle 4|S_{hv}^1|^2 \rangle \end{bmatrix} \quad (2.24)$$

$$[T_{22}] = \begin{bmatrix} \langle |S_{hh}^2 + S_{vv}^2|^2 \rangle & \langle (S_{hh}^2 + S_{vv}^2)(S_{hh}^2 - S_{vv}^2)^* \rangle & 2\langle (S_{hh}^2 + S_{vv}^2)S_{hv}^2* \rangle \\ \langle (S_{hh}^2 - S_{vv}^2)(S_{hh}^2 + S_{vv}^2)^* \rangle & \langle |S_{hh}^2 - S_{vv}^2|^2 \rangle & 2\langle (S_{hh}^2 - S_{vv}^2)S_{hv}^2* \rangle \\ 2\langle S_{hv}^2(S_{hh}^2 + S_{vv}^2)^* \rangle & 2\langle S_{hv}^2(S_{hh}^2 - S_{vv}^2)^* \rangle & \langle 4|S_{hv}^2|^2 \rangle \end{bmatrix} \quad (2.25)$$

$$[\Omega_{12}] = \begin{bmatrix} \langle (S_{hh}^1 + S_{vv}^1)(S_{hh}^2* + S_{vv}^2*) \rangle & \langle (S_{hh}^1 + S_{vv}^1)(S_{hh}^2* - S_{vv}^2*) \rangle & 2\langle (S_{hh}^1 + S_{vv}^1)S_{hv}^2* \rangle \\ \langle (S_{hh}^1 - S_{vv}^1)(S_{hh}^2* + S_{vv}^2*) \rangle & \langle (S_{hh}^1 - S_{vv}^1)(S_{hh}^2* - S_{vv}^2*) \rangle & 2\langle (S_{hh}^1 - S_{vv}^1)S_{hv}^2* \rangle \\ 2\langle S_{hv}^1(S_{hh}^2* + S_{vv}^2*) \rangle & 2\langle S_{hv}^1(S_{hh}^2* - S_{vv}^2*) \rangle & \langle 4S_{hv}^1S_{hv}^2* \rangle \end{bmatrix} \quad (2.26)$$

In the *equation 2.20*, the matrices $[T_{11}]$ and $[T_{22}]$ are Hermitian matrix, which are the complex squared matrix that are equal to its conjugate transpose matrix. While $[T_{11}]$ consist of the polarimetric information of the first satellite pass, $[T_{22}]$ consist of the polarimetric information of the second satellite pass. Both these matrices are shown in *equation 2.24 and 2.25*, respectively. $[\Omega_{12}]$ is a non-Hermitian matrix, shown in

equation 2.26, and consist of the polarimetric and interferometric information of both the satellite passes (Khatai & Kumar, 2014).

2.4.3.3. Vertical wavenumber

Since the relationship between the interferometric phase (ϕ) and the height of scatterers (h) is represented by the vertical wavenumber (k_z) (Ghosh et al., 2018; Khatai & Kumar, 2014), it becomes very important to generate the k_z file while retrieving the forest height using PolInSAR method. The relation between them is shown in the *equation 2.27* (Ghosh et al., 2018).

$$\phi = k_z h \quad (2.27)$$

The vertical wavenumber depends upon the effective perpendicular baseline (B_{\perp}) which is a projection of the spatial baseline on the slant range (Ferretti et al., 2007), the wavelength (λ) of the electromagnetic signal used in the PolInSAR process, the incidence angles of the two passes, and the sensor to ground pixel distance (R). Hence, the value of k_z will be pixel wise. The formulae generally used to generate it are in the *equations 2.28 and 2.29*. Studies suggested the value of k_z must be chosen wisely as a higher value could saturate the coherence for some forest heights, while lower value of it won't let the coherence segregate the forest heights (Ghosh et al., 2018; Kugler et al., 2015). The best component to experiment with is the perpendicular baseline term, which could influence the range of values of desired k_z . The generated k_z is then used to retrieve the forest height which is further validated with the in-situ observations or other accurate airborne or spaceborne missions.

The distance between the sensor and the ground pixel, depicted by R , is obtained by multiplying the speed of the electromagnetic wave with half of the time taken by wave to transmit and receive the signals from ground (S. Kumar et al., 2020). While θ is the incidence angles of the primary data, and $\Delta\theta$ is the difference between incidence angle of corresponding pixels of the primary and the secondary data.

$$k_z = \frac{4\pi B_{\perp}}{\lambda R \sin \theta} \quad (2.28)$$

$$k_z = \frac{4\pi \Delta\theta}{\lambda \sin \theta} \quad (2.29)$$

where,

$$\theta = \frac{\theta_1 + \theta_2}{2} \quad \text{and} \quad \Delta\theta = \theta_1 - \theta_2.$$

However, the baseline component must be chosen carefully as it is directly related with the volumetric decorrelation (Krieger et al., 2005). Higher the baseline value, larger will be the decorrelation which is not desired for parameter estimation. In interferometric SAR and polarimetric SAR interferometry, in monostatic systems where satellite data is acquired on two different time periods, an additional decorrelation is observed known as the temporal decorrelation, which is mainly due to alteration of different target properties and environmental processes that may occur in between the two acquisitions. The environmental processes that may include severe weather conditions such as extreme wind, drought (Aghababaei et al., 2020) or some other calamity such as deforestation. Usually, such conditions occur over a larger period (months or even years in some cases). Though in monostatic systems temporal decorrelation must not be

ignored, but for the ease of study, we ignored this factor in this study. A range of height bias induced in the retrieved forest height may be from 0 to 4 meters for a value of vertical wavenumber of around 0.2 (Krieger et al., 2005). The forest of our study area is very old, and the trees are mostly matured, hence we could assume there is negligible effects due to temporal decorrelation. Also, the temporal baseline of the pair of data for all the three satellites is less than a month, hence we could assume very low, or no effects.

2.4.3.4. Coherence optimization

When multi-polarized data such as a Dual polarized or a Quad polarized data is present in the PolInSAR system, there are possibilities of multiple polarization combinations that can be used in interferometric processing. The idea behind the process of coherence optimization is to evaluate the polarization for retrieving the highest coherence (Shane Robert Cloude & Papathanassiou, 1998). A better estimation of phase can be obtained with a higher value of coherence (Ghosh et al., 2018). Various scattering mechanisms can be associated with a quad polarized data. For applications of forest, such as obtaining the forest height, out of the three main scatterings, volume scattering is in abundance due to undulated and non-uniform tree canopy surface. Hence for forest regions, the HV (cross) polarization gives the best result as it contains the maximum information about volume scattering. For obtaining the tree height, the two set of coherences must be chosen so that there is sufficient interferometric phase separation between the phase of top of the canopy and that of the ground.

A unit circle is used to estimate the phase and coherence amplitude by projecting these values for different polarization combinations. A coherence region is thus generated by combining all these coherence values. This region helps in determining the set of two scattering mechanisms that have the maximum interferometric coherence separation (Ghosh et al., 2018). Such a coherence region within a unit circle of phase and amplitude values is shown in *figure 6*. PolInSAR coherence is shown in the *equation 2.30*.

$$\gamma = \frac{\langle \omega_1^\dagger [\Omega_{12}] \omega_2 \rangle}{\sqrt{\langle \omega_1^\dagger [T_{11}] \omega_1 \rangle \langle \omega_2^\dagger [T_{22}] \omega_2 \rangle}} \quad (2.30)$$

Here, ω_1 and ω_2 are the two desired scattering mechanisms that will be having maximum interferometric coherence separation. $[T_{11}]$ and $[T_{22}]$ are the two Hermitian matrices shown in *equations 2.24 and 2.25*, respectively. $[\Omega_{12}]$ is the matrix consisting of polarimetric and interferometric information as shown in *equation 2.26*.

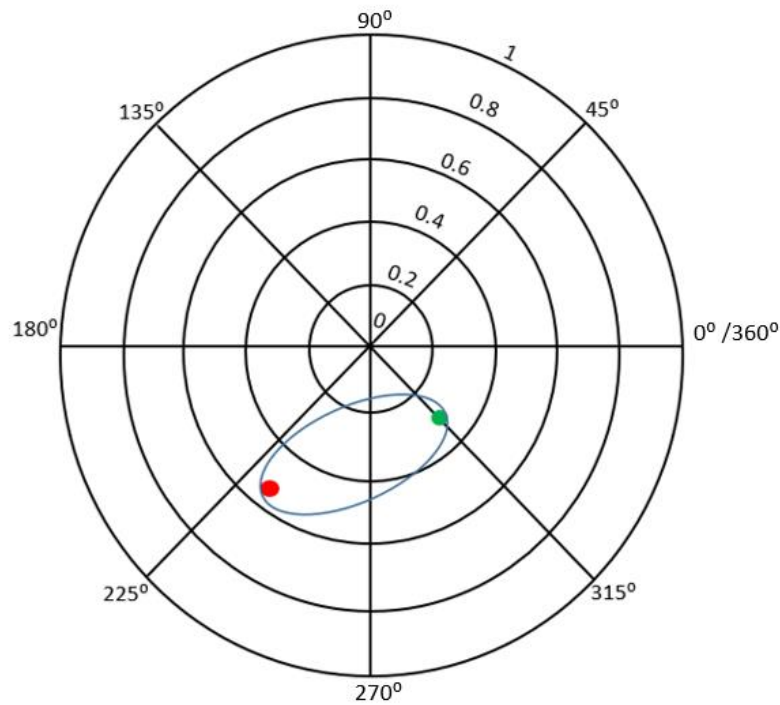


Figure 6: An illustration of a unit circle with phase and coherence values and coherence region that contains all possible polarization combinations. In this example, the green coloured dot depicts the coherence value of HV polarisation while the red coloured dot depicts the coherence value of HH polarisation in linear basis. The blue coloured shape consists of coherence values of all possible polarisations in the linear basis and is defined as the coherence region.

2.5. Decomposition techniques in SAR

Decomposition is performed on the coherence matrix where it gets divided based on different scattering types (Parida & Mandal, 2020). Various decomposition techniques have been developed over the years such as the H/A/ α , Yamaguchi, Freeman-Durden decompositions. According to the article by Cloude and Pottier (Shane Robert Cloude & Pottier, 1996) target decomposition techniques are mainly classified into 3 classes; Huynen type, based on coherent theorems, and based on eigenvector decomposition of the coherence or covariance matrix.

Coherent decomposition models are applied where features exhibiting similar properties are present. But in real scenario, it is very difficult to obtain an area which has same properties and instead expect a pixel (or an area) to possess different backscattering properties. Therefore, incoherent decomposition techniques are applied to areas which are heterogeneous, meaning consisting of different types of scatterers. There are mainly pure and complex scatterers, of which forest areas are considered in the complex scatterer because of their property of having different scattering types. The different scattering types vary with different decomposition models, such as the Freeman-Durden decomposition considers mainly three types of scatterings: the surface scattering, the double bounce scattering, and the volumetric scattering. In the context of forest, it is considered as a complex scatterer because of different types of features present, which may backscatter to give varied information. Surface scattering usually occurs from the ground, double bounce

scattering from the tree trunk-ground interaction point, and volumetric scattering from the top of the canopy of the tree, all of which are illustrated in *figure 7*.

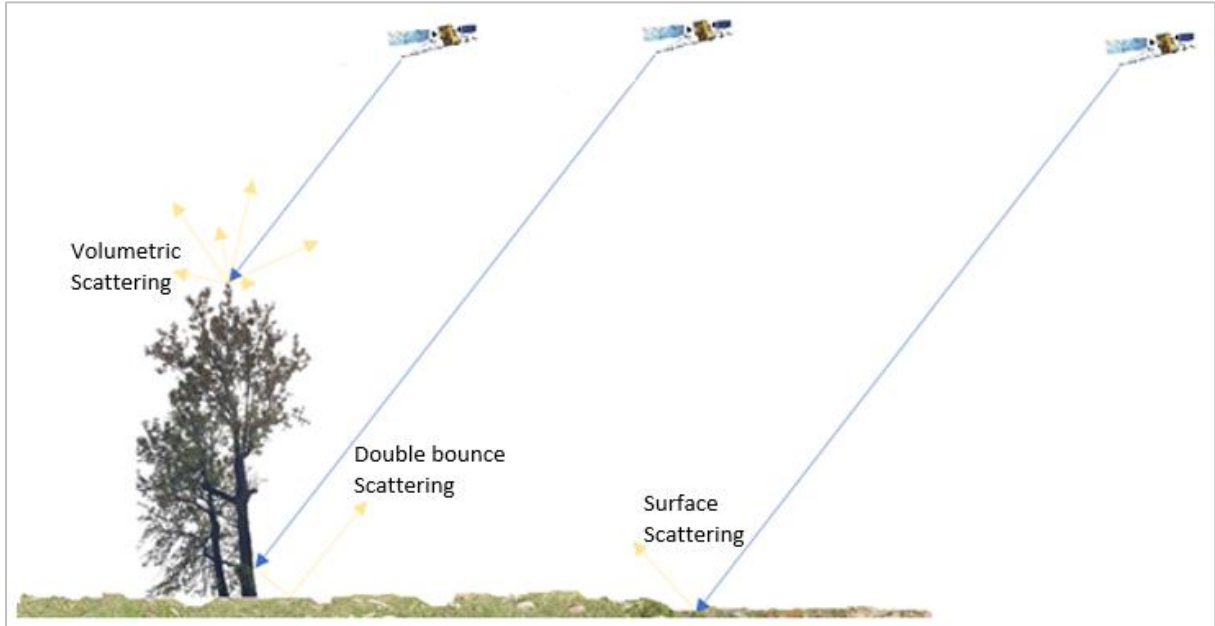


Figure 7: Different types of scatterings

There are some other types of scattering too, which are used in other decomposition models such as the Yamaguchi decomposition, which have a fourth type of scattering apart from the above three, known as the helix scattering, which is useful in urban areas (Khatai & Kumar, 2014). Although that is present in the four component Yamaguchi decomposition. The concept behind helix scattering is that it opposes the assumption of the reflection symmetry condition, an assumption used in three component decompositions, in which $\langle S_{HH}S_{HV}^\dagger \rangle \approx \langle S_{VV}S_{HV}^\dagger \rangle \approx 0$ in the coherence matrix was assumed. With this, $\langle S_{HH}S_{HV}^\dagger \rangle \neq 0$ and $\langle S_{VV}S_{HV}^\dagger \rangle \neq 0$ were used to better describe the urban areas (Yamaguchi et al., 2005).

Depending upon the wavelength, the transmitted signals may penetrate some objects, such as leaves. TerraSAR-X satellite which has X band frequency waves, have the least wavelength amongst the one used in this study and has almost no penetration capability. On the other hand, RADARSAT-2 satellite has the C band frequency waves and has feeble penetration capability, backscattering from the twigs, branches and even from the bottom parts of the trees apart from the top of the canopy. The third satellite used in this study is ALOS PALSAR-2 with L band frequency waves and has great amount of penetration and much of the backscatter bypasses the top of the canopy leaves, and backscatters from twigs, branches, and trunk of the tree.

2.6. Inversion models for estimation of forest height

Various algorithms and techniques have been used in the past to accurately estimate the forest height. One of the techniques used for such is DEM differencing where information from the scattering through top of

the canopy is compared with the information from the scattering through ground (Li et al., 2019). However, the technique was much dependent upon the wavelength of the signals used in the study as scattering from the ground was either possible through canopy gaps, or with the use of high wavelength waves having penetration capability. Most of the studies using airborne sensor, especially LiDAR, to estimate height of vertical structures used the technique of DEM differencing as it had possibility of showing higher accuracy in the estimated forest height.

Other ways of obtaining the height of vertical structures such as forest was through the use of inversion models, such as the Random Volume over Ground (RVoG) (S R Cloude & Papathanassiou, 2003; Tobias Mette & Knoke, 2006). Other techniques are the Three Stage Inversion (TSI) model and the Four Stage Inversion (FSI) model (Managhebi & Maghsoudi, 2018). While the effect of temporal decorrelation was not accounted for in the TSI model, the use of same in the FSI model increased the accuracy of the forest height obtained (Managhebi & Maghsoudi, 2018). The temporal decorrelation is mainly affected by structure of the targets and by the environmental processes that occur in between the two acquisitions (S. Lee et al., 2009). In the TSI technique, complex coherences are observed in a complex plane in different polarizations, each having a magnitude and phase value. Using the least square line fit algorithm, difference between the model predicted value and observed value is minimized (S R Cloude & Papathanassiou, 2003). Further, the true ground phase is calculated using the ground to volume scattering ratio, which is low for a pixel having more volumetric scattering component as compared to the surface scattering component, and high for a pixel having more surface scattering component. The height is estimated subsequently.

2.6.1. Three Stage Inversion model

The basis of a study by Cloude and Papathanassiou (S R Cloude & Papathanassiou, 2003) was a two-layer vegetation model which could derive the complex interferometric coherence, denoted by γ , for a random volume over ground, as shown in *equation 2.31*. The two-layer model is shown in *figure 8*, where the two layers, namely the bottom layer and the top layer, are present above the ground which is at an elevation of $z=0$. The forest canopy, whose height is h_v , is assumed to have the extent from $z=z_0$ to $z=z_0+h_v$.

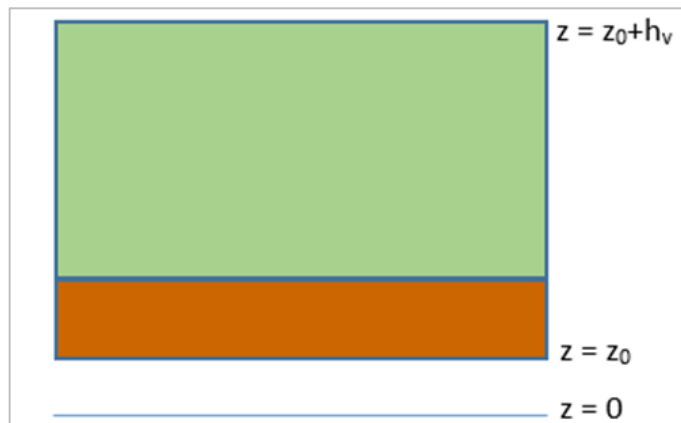


Figure 8: Schematic diagram of the three-stage inversion model.

$$\gamma = \frac{\omega^\dagger (I_2^V e^{i\Phi_2} + T_g e^{i\Phi_1} e^{(-2\sigma h_v)/\cos \theta_0}) \omega}{\omega^\dagger (I_1^V + T_g e^{(-2\sigma h_v)/\cos \theta_0}) \omega} \quad (2.31)$$

where,

$$I_1^V = e^{(-2\sigma h_v)/\cos \theta_0} \int_0^{h_v} e^{2\sigma z'/\cos \theta_0} T_V dz' \quad (2.32)$$

$$I_2^V = e^{(-2\sigma h_v)/\cos \theta_0} \int_0^{h_v} e^{2\sigma z'/\cos \theta_0} e^{ik_z z'} T_V dz' \quad (2.33)$$

$$T_V = m_v \begin{bmatrix} 1 & 0 & 0 \\ 0 & \mu & 0 \\ 0 & 0 & \mu \end{bmatrix} \quad 0 \leq \mu \leq 0.5 \quad (2.34)$$

$$T_g = m_g \begin{bmatrix} 1 & t_{12} & 0 \\ t_{12}^* & t_{22} & 0 \\ 0 & 0 & t_{33} \end{bmatrix} \quad (2.35)$$

In these equations, Φ_1 is the phase centre of the bottom layer, and it is assumed to be equal to Φ_2 as the canopy extends from ground to top. T_V is a 3x3 diagonal coherence matrix for volumetric scattering, while T_g is a 3x3 reflection symmetric ground scattering coherence matrix (Khati & Kumar, 2014).

The complex coherence is dependent on polarization, which can be represented as a straight line in the complex plane as shown in *equation 2.36*.

$$\gamma(\omega) = e^{i\Phi_1} (\gamma_v + L(\omega)(1 - \gamma_v)) \quad 0 \leq L(\omega) \leq 1 \quad (2.36)$$

where,

$$L(\omega) = \frac{\mu(\omega)}{1 + \mu(\omega)} \text{ and } \mu(\omega) = \frac{2\sigma \omega^\dagger T_g \omega}{\cos \theta_0 (e^{(2\sigma h_v/\cos \theta_0)} - 1) \omega^\dagger T_V \omega}$$

$$\gamma_v = \frac{2\sigma}{\cos \theta_0 (e^{(2\sigma h_v/\cos \theta_0)} - 1)} \int_0^{h_v} e^{ik_z z'} e^{2\sigma z'/\cos \theta_0} dz' \quad (2.37)$$

In these equations, ω is a unitary complex vector, γ is the interferometric complex coherence, Φ is the interferometric phase of ground topography, $\mu(\omega)$ is the ground to volume scattering ratio, θ_0 is the angle of incidence, and σ is the attenuation of waves induced as it passes through the forest tree canopy (S. Kumar et al., 2020). A graphical representation of the inversion of *equation 2.36* is shown in *figure 9*.

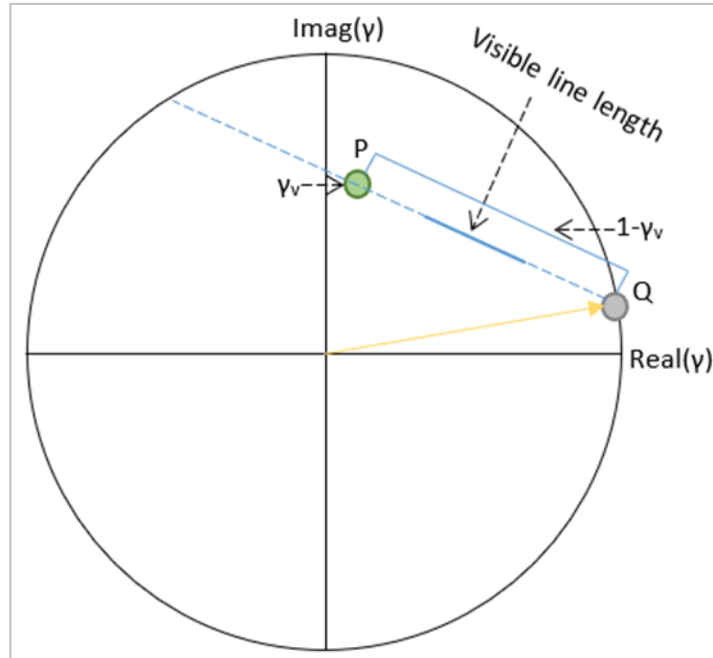


Figure 9: representation of inversion of γ in a unit circle.

The unit circle is intersected by the line at two points, out of which one is the true ground phase (here in the *figure 9*, it is shown as point Q), and the other solution must be rejected. A point in the line where ground to volume scattering ratio is zero depicts the top of the canopy phase, which is also the volume coherence, depicted as point P in *figure 9*. Using these, the tree height could be estimated. The three stages of the Three Stage Inversion model are described below.

STAGE 1: Least Squares line fit

The complex coherences in all possible polarizations are plotted on the complex plane and a best fit line is calculated. The line intersects the complex plane at two locations, out of which one is the true ground phase. The same is obtained using vegetation bias removal step which is the second stage of the process.

STAGE 2: Vegetation bias removal

The ground to volume scattering ratio is used in this step to estimate the true ground phase. The idea behind it is that the ratio will be closer to 0 when the pixel has more volumetric scattering component than the ground scattering component, while it will be near to 1 when more surface scattering is observed than the volumetric scattering in the pixel. Volumetric scattering is mainly associated with HV polarization (for linear basis), or HV+VH polarization (for Pauli basis). Hence, the intersection point which is farthest from such coherences will depict the true ground phase.

STAGE 3: Height and extinction estimation

Using *equation 2.37*, with a fixed value of the mean wave extinction, σ , a relation between the complex coherence, γ_v and height, h_v is obtained and the curves at various values of σ are plotted on a unit circle. The possible values of γ_v are those where the curves intersect the coherence best fit line. For all such points, ground to volume scattering ratio is obtained. Since μ can only be a positive number between 0 and 1, all other points are filtered out. With these steps, the height of the trees is obtained (Khatai & Kumar, 2014).

Detailed explanation could be found in the original paper of Cloude and Papathanassiou (S R Cloude & Papathanassiou, 2003).

2.6.2. Coherence Amplitude Inversion model

For all the SAR sensors of various wavelengths, backscattered signals from forest regions always have the component of the top of the canopy, and nearby branches of the trees. Because of an unstable structure of the canopy, the overall coherence obtained is very less. For stable and hard surfaces, the coherence values are much higher. These hard surfaces in forest regions maybe tree branches. The tree height in SAR systems is obtained using interferometric phase difference of the top and bottom layer but retrieving information from ground in a forest region is difficult for an X-band TerraSAR-X satellite because of its no penetration capability due to its low wavelength. So, to overcome the problem of the interferometric phase coherence, an amplitude-based approach was proposed where ground is identified with polarimetric channels having low surface to volume ratio (S. Kumar et al., 2020). The Coherence Amplitude Inversion method is shown in *equation 2.38*.

$$\min_{h_v} \left\{ F = \left| \left| \tilde{\gamma}_{\omega_v} \right| - \left| \frac{p e^{p_1 h_v} - 1}{p_1 e^{p h_v} - 1} \right| \right| \right\} \quad \text{where } \begin{cases} p = \frac{2\sigma}{\cos \theta} \\ p_1 = p + ik_z \end{cases} \quad (2.38)$$

Here in the equation, the function F is minimized for inversion-based modelling, $\tilde{\gamma}_{\omega_v}$ depicts the volume only coherence, σ represents the mean wave extinction and h_v depicts the height of the trees in the canopy (S. Kumar et al., 2020).

3. STUDY AREA

Area chosen for the study is the forest area in the Manali city of Himachal Pradesh state in India. The forests, which are relatively old, are located at $32^{\circ}14'23.07''$ N and $77^{\circ}11'22''$ E, and $32^{\circ}15'01.58''$ N and $77^{\circ}11'16.06''$ E. *Figure 10* shows the map consisting of the forest and its nearby areas. The forest regions named as Ram Bagh and Van Vihar are the two on the left of the riverbed of river Beas, sandwiching the Manali city which is in the middle of the map. Both are denoted by dark red colour, as per the standard False Colour Composite (FCC) of the Sentinel-2B data. While the area of Ram Bagh is 338267 square meters, the area of Van Vihar is 174213 square meters. The main tree species found in the region are *Deodar*, while *Pine* and *Thuja* trees can also be found.

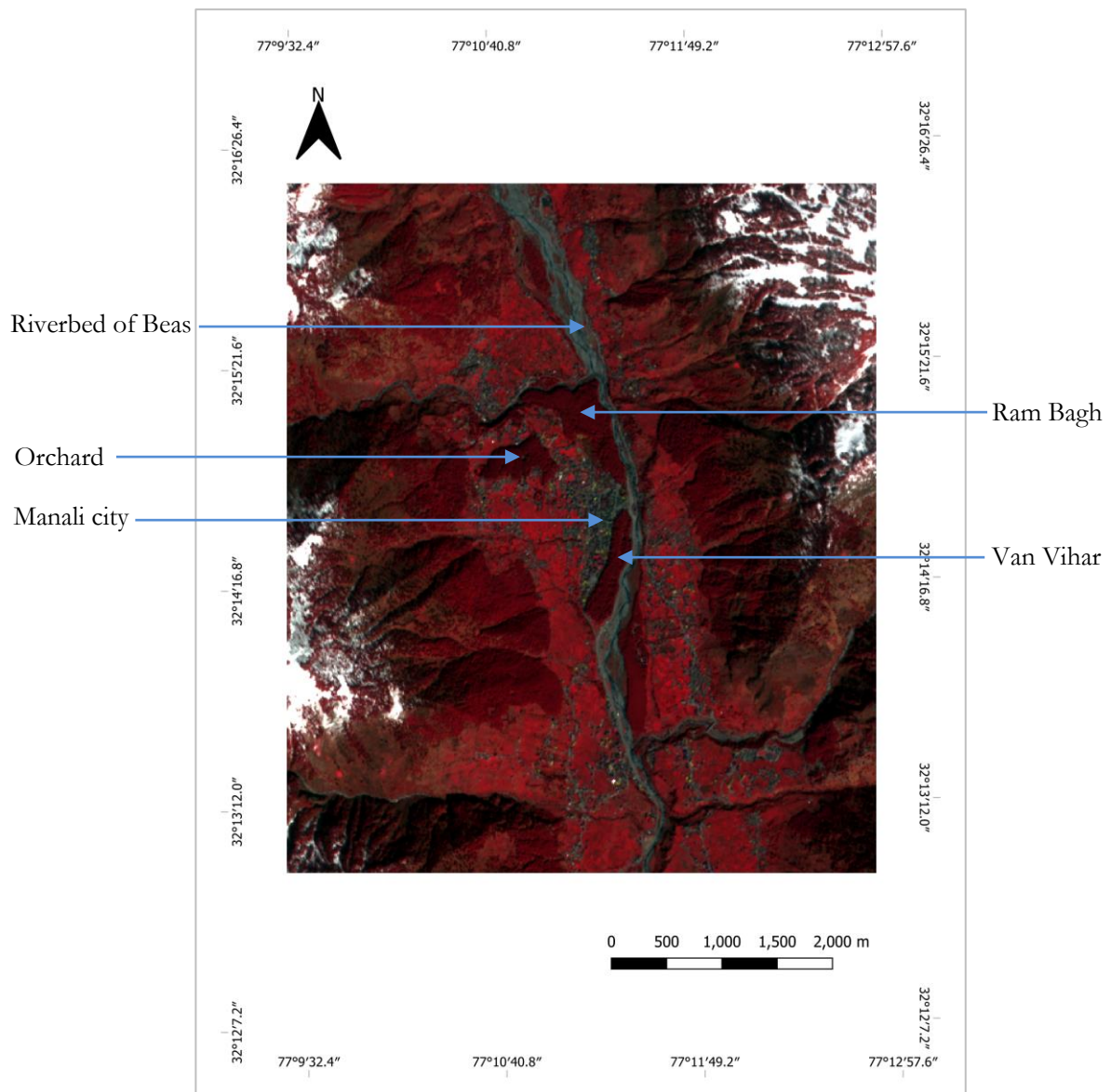


Figure 10: Standard False Colour Composite image of the region obtained using Sentinel-2B optical satellite.

3.1. Dataset

This study focuses on PolInSAR data of three frequencies: X, C, and L band. Quad polarized data of the TerraSAR-X satellite is used for estimation of forest height through X band. Data was acquired on a descending orbit pass in the year 2015, with a temporal baseline of 22 days. The wavelength of the data is 3.10 cm. Similarly, quad polarized data of RADARSAT-2 and ALOS-2 PALSAR-2 satellites are being used for C band and L band, respectively, with the former being acquired in the year 2012 and the latter in the year 2015. The temporal baseline of the L band data is 28 days. All the sensor parameters are shown in the *table 1*. Further, for validation of the results, GEDI data may be used to relate the findings of the model with the global forest height canopy map.

Table 1: Parameters of the dataset used in this study.

Parameter	TerraSAR-X		RADARSAT-2		ALOS-2 PALSAR-2	
	Primary	Secondary	Primary	Secondary	Primary	Secondary
<i>Acquisition</i>	Primary	Secondary	Primary	Secondary	Primary	Secondary
<i>Date of acquisition</i>	12-Feb-15	21-Jan-15	01-Dec-12	07-Nov-12	24-Apr-15	27-Mar-15
<i>Frequency band</i>	X- band		C- band		L- band	
<i>Wavelength</i>	3.1 cm		5.54 cm		24.24 cm	
<i>Frequency</i>	9.64 GHz		5.40 GHz		1.23 GHz	
<i>Polarization</i>	Quad Polarization (HH+HV+VH+VV)					
<i>Near range incidence angle</i>	37.898°	37.925°	30.2622°	30.2639°	32.3249°	32.3208°
<i>Far range incidence angle</i>	39.683°	39.711°	31.9857°	31.9873°	35.3218°	35.3181°
<i>Perpendicular baseline</i>	265.78 m		147.66 m		145.07 m	
<i>Temporal baseline</i>	22 days		24 days		28 days	

Apart from this, the Sentinel 2-B satellite data was used for optical imagery of the Manali forests. The spatial resolution of the data is 10 meters, while the date it was acquired on is 23 March 2021.

3.2. Field data

Field data was acquired in the year 2012 by Dr. Shashi Kumar with an aim to co-acquire the data with the RADARSAT-2 satellite, whose satellite pass was supposed to happen over the region on 1 December 2012. Some of the field photographs have been shown in *figures 11, 12, 13 and 14*. Although the data of TerraSAR-X and ALOS-2 were of the year 2015, with the temporal gap of 3 years, a slight change is expected in the height of the trees, which can be correlated since the trees are old and already matured. A total of 8 plots, each of area 0.1 hectare, were chosen in the two forest ranges. The plots were squared plots with a side length of 31.62 m. Using a laser dendrometer (RD 1000), as shown in hands of Dr. Shashi Kumar in *figure 11*, all the tree heights within the plots were obtained. Tree height of all the trees in the region were in the

range of 35 to 50 meters. This knowledge was helpful in determination of the baseline and calculation of the vertical wavenumber.



Figure 11: Figure showing Dr. Shashi Kumar using a laser dendrometer RD1000 to obtain the tree heights within a plot of 0.1 hectare. Image was taken on 27 November 2012.



Figure 12: Figure showing the gaps between trees which could help the non-penetrating waves detect ground information. Image was taken on 27 November 2012.



Figure 13: A field visit photo depicting the height of the trees in the region, which could increase up to 50 meters. Though, most of the trees were about 40 meters tall. Image was taken on 27 November 2012.



Figure 14: The region was undulating with tree ranges too having topographic variations because of mountains. Image was taken on 30 November 2012, a day before the satellite pass.

3.3. Global Ecosystem Dynamics Investigation (GEDI) data

Aboard the International Space Station (ISS), GEDI mission uses LiDAR technology to derive forest parameters, such as the forest height, for the whole planet. A study by Dr. Shashi Kumar (S. Kumar et al., 2020) used GEDI derived forest height data to validate their results of the obtained forest heights. The study revealed that correlation of the derived results with the GEDI data was not satisfactory as the GEDI data had underestimated the forest height values at many locations. The forest canopy height map is of the year 2019, while our data are of the years 2012 and 2015.

4. METHODOLOGY

The present work focuses on the use of satellites of three different frequencies: TerraSAR-X, RADARSAT-2, and ALOS-2 PALSAR-2 for the estimating the height of forest in the Manali forest ranges namely, Van Vihar and Ram Bagh. An estimate of the height of features in the area is required for the estimation of baseline, which is an important step in calculation of the vertical wavenumber (k_z). Apart from this, a field visit to the study area serves the purpose of field values which are useful in the validation of results. In the following section, the methodology implemented in this study has been explained in brief.

4.1. Co-registration of image pair

Pre-processing is the major step in a study where the input data is processed into a desired usable data which can be interpret by the system. The first step was to perform the radiometric calibration to represent the real radar backscattered values in the images. It is essential to perform this step when quantitative use of the data is required. For the satellites used in this study, the absolute radiometric calibration was performed in the ESA software SeNtinel Applications Platform (SNAP) with the incident angle correction, antenna pattern gain correction, range spreading loss correction, and calibration constant correction had already been done in the satellite products (*ESA-SNAP. Help Contents*, n.d.).

Since interferometry deals with two satellite data, co-registration was performed in the next step, where the focus was to ensure that the analysis performed was for the same set of pixels in both the primary and the secondary data. In this step, an appropriate master data is chosen amongst the two images while naming the other image as slave, which would then reproject and register itself with the extent of the master image. Also, this step was useful to determine the phase difference accurately between the two sets of data. After this step, all the scenes in the primary and the secondary data were stacked into the geometry of the primary data, and backscattered value from a pixel in both the primary and the secondary represented the information from the same ground feature. Further, multi-looking was performed to visualise square pixels with appropriate range and azimuth looks. However, the aim of this process was just to visualise the satellite image with square pixels and was not used in this study otherwise.

4.2. Generation of k_z number

The 2π ambiguity height, defined as the height corresponding to a 2π phase change, is also an important component as its value determines the accuracy of vertical structures such as trees. For accurate height results, the value of the height of ambiguity must be greater than the longest tree in the region (Joshi & Kumar, 2017; Minh et al., 2014). The vertical wavenumber file was finally generated using the estimated baseline, the slant range, and the incidence angle. Since slant range values and incidence angle varies for each pixel, a range of k_z values were obtained.

4.3. T6 coherency matrix

The processing step initiated with the generation of scattering matrix for both, the primary and the secondary data. This scattering matrix was a 2x2 matrix consisting of information about the scatterers and the process of scattering. With the fully polarimetric data of all four possible polarization combinations, such as HH, HV, VH, and VV, each pixel exhibits different amount of contribution from different polarization combination. In the following equations, S_1 represents the scattering matrix of the Primary data, while S_2 depicts the scattering matrix of the secondary data.

$$S_1 = \begin{bmatrix} S_{HH}^1 & S_{HV}^1 \\ S_{VH}^1 & S_{VV}^1 \end{bmatrix} \quad S_2 = \begin{bmatrix} S_{HH}^2 & S_{HV}^2 \\ S_{VH}^2 & S_{VV}^2 \end{bmatrix}$$

The first order derivative of the scattering matrix, known as the Pauli feature vector, was generated using the Pauli spin matrix set, Ψ_P (equation 2.8). The Pauli spin matrix set consisted of four 2x2 complex matrices (Shane Robert Cloude & Papathanassiou, 1998). The generated Pauli feature vector is shown in the equation 2.9. Since the system is a monostatic system, we assumed the condition of reciprocity where $S_{HV} = S_{VH}$, making this matrix a 3x1 matrix, as depicted in equation 2.13.

The feature vectors of the primary and secondary data were combined to form a 6x1 matrix and multiplied with their conjugate transpose to generate a 6x6 coherency matrix. Following equations show the methodology of the same. Pauli feature vector of primary data is denoted as k_1 , while that of secondary data is denoted as k_2 .

$$k_1 = [S_{HH}^1 + S_{VV}^1 \quad S_{HH}^1 - S_{VV}^1 \quad 2S_{HV}^1]^T \quad (4.1)$$

$$k_2 = [S_{HH}^2 + S_{VV}^2 \quad S_{HH}^2 - S_{VV}^2 \quad 2S_{HV}^2]^T \quad (4.2)$$

The coherency matrix T_6 was generated using equation 4.3. In the equation, k_1^\dagger depicts the conjugate transpose of k_1 , while k_2^\dagger depicts the conjugate transpose of k_2 . The finally generated T6 matrix is shown in equation 2.23, where * denotes the conjugate value.

$$T_6 = \begin{bmatrix} k_1 \\ k_2 \end{bmatrix} \begin{bmatrix} k_1^\dagger & k_2^\dagger \end{bmatrix} = \begin{bmatrix} [T_{11}] & [\Omega_{12}] \\ [\Omega_{12}]^\dagger & [T_{22}] \end{bmatrix} \quad (4.3)$$

Here, matrices T_{11} and T_{22} are Hermitian matrices consisting of polarimetric information of the data of the first and second pass, respectively. While Ω_{12} is a matrix consisting of interferometric information of the data from first and second pass (S. Kumar et al., 2020).

4.4. Complex coherence

Further, the complex coherences in different polarization basis such as linear, Pauli, circular, and optimal basis were computed. Forest height was then obtained using the previously calculated vertical wavenumber file and these complex coherences. For the coherence amplitude inversion technique, various combinations of polarisation were used to distinguish the backscatter from the top of the canopy with that from the surface. Such as in Pauli basis, HV +VH depicted the top of the canopy, HH+VV depicted the surface

backscatter, and HH-VV depicted the double bounce scattering. Similarly in linear basis, while HV determined the top of the canopy backscatter, VV determined the surface backscattering.

4.5. Forest height estimation using Three Stage Inversion and Coherence Amplitude Inversion

Using the multiple coherences obtained and the generated k_z file, the forest height was estimated with steps as explained in the 2.6.1 section. For coherence amplitude inversion model in height estimation, the requirement was to select the coherence pair that would represent the top of the canopy and ground level. So, HV+VH was used as the volumetric component to represent the top of the canopy backscatter, while HH+VV was used as the surface scattering component to represent the backscatter from ground. HH-VV could have also been used since the signals strike the ground at one point, but it was not chosen because of uncertainty of the signals hitting the tree trunk first or the ground first, which could have introduced an error. Also, double bounce scattering is dominant in regions such as the dry riverbed, and building-ground interaction, apart from the tree trunk-ground interaction.

4.6. Range doppler terrain correction and masking

In mountainous regions, features with an elevation tend to have topographic distortions when they are away from than nadir of the SAR sensor. Also, because of a tilt of the sensor, the satellite images tend to have topographic distortions, which are minimized by implementing the step of range doppler terrain correction (*ESA-SNAP. Help Contents*, n.d.). Since the study area was in the mountainous regions, the terrain correction was the next step, for which, a 30 m Copernicus DEM was used to make the images look like a real-world replica.

For the selection of the desired area of interest, an optical satellite image was used to digitize the two forest ranges of our study area. The open source QGIS software was used for this step. Because of its high spatial resolution of 10 meter, which ensured lesser possibilities of any feature loss, the Sentinel 2B satellite was used for this purpose. A cloud free data was downloaded to have the least interference from clouds since optical data is susceptible to atmospheric particles. Using this vector data, masking was performed in the SNAP software, where the non-forest region were masked out while the desired area of interest was obtained.

4.7. Validation of results

The 2019 global forest canopy height map for the North Asian region was downloaded for validating with the field data of the area, and with the forest height maps generated using the Three Stage Inversion and Coherence Amplitude Inversion methods. Also, the field data acquired by Dr. Shashi Kumar in the year 2012 was used for validating the results obtained in this study. Due to a coarser spatial resolution of the RADARSAT-2 satellite, lesser number of pixels could accommodate within a field plot of 0.1 hectare. So, forest height of 5 pixels per plot are taken and averaged to establish the modelled forest height of the plot.

Similarly, because of higher spatial resolution of ALOS-2 and TerraSAR-X satellites, 10 pixels per plot are used to establish an averaged forest height of a plot. A flowchart, shown in *figure 15*, has been made for a general overview of the steps involved and processes followed in this study.

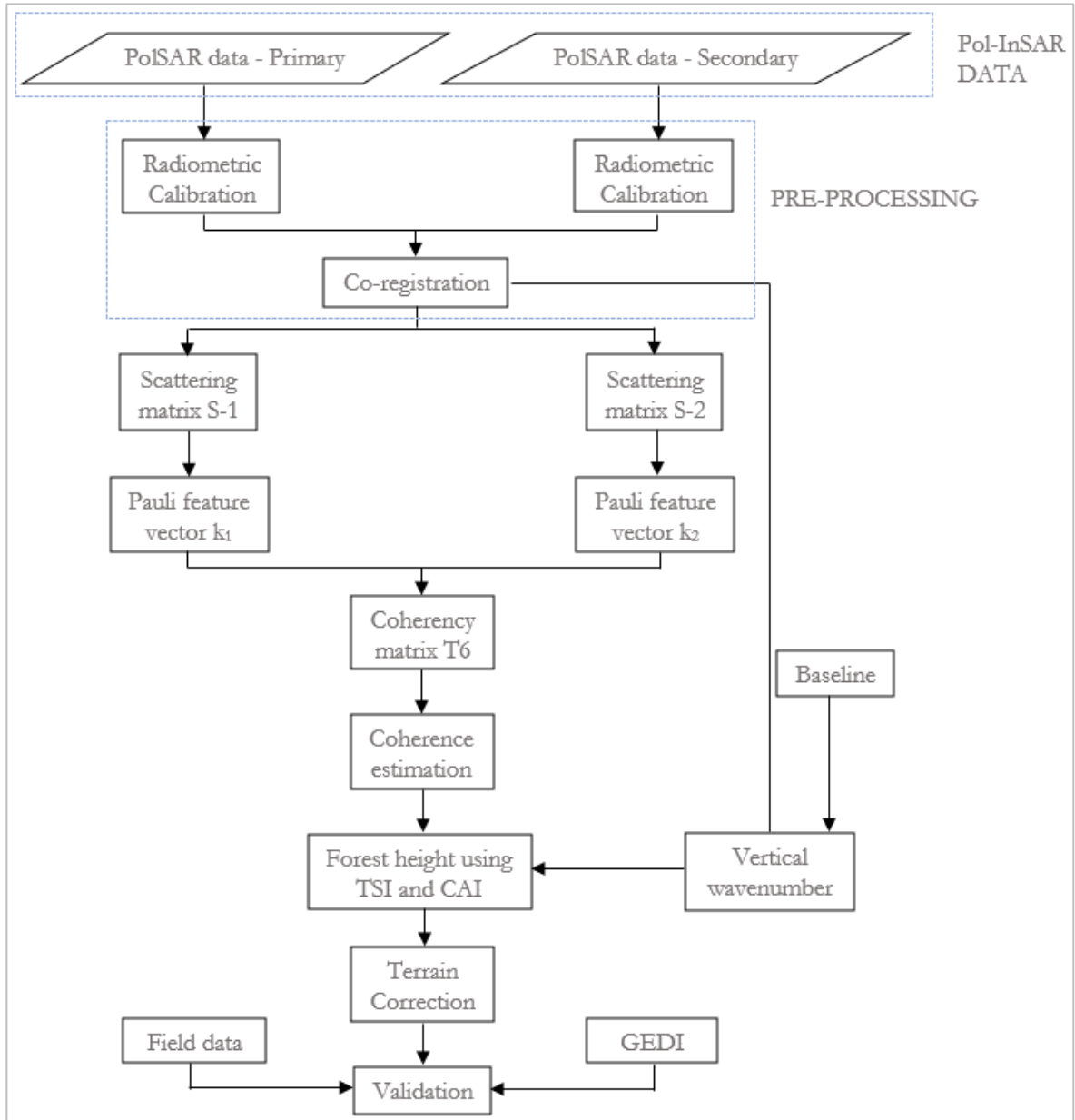


Figure 15: Flowchart explaining the methodology of this study.

5. RESULTS AND DISCUSSION

A study to retrieve the forest height of the forests of Manali; Ram Bagh, and Van Vihar, was carried out using the SAR operating satellites; TerraSAR-X, RADARSAT-2, and ALOS-2 PALSAR-2, which consist of sensors working in the X, C, and L band wavelength, respectively. The findings and observations of the study are described in this section.

5.1. Shift due to co-registration

Going by the methodology, the first pre-processing step was the conversion of the pixel values into real radar backscattered values. After the calibration of both the primary and the secondary polarimetric data, the master data was chosen to be the one with lesser pixels amongst the two image pairs. Upon the coarse and the fine co-registration of the image pairs were completed, shift was induced in the slave image as the pixels located outside the extent of the master image were substituted with no value.

The processing initiated with the generation of scattering matrices S1 and S2 for the two sets of images. Their Pauli RGB images are shown in the following figures. The second (right) image of *figure 16* below, showing the Pauli RGB image of the secondary acquisition of RADARSAT-2 satellite, reveals few black columns on the left side and few rows on the bottom depicting the shift in the columns and rows, respectively, because of co-registration. Figure below shows significant volumetric scattering in the scene, depicted by green colour in the images. The footprint of all 3 satellite images consists mostly of mountainous forest regions with few small villages being the only man-made structures apart from the Manali city. The scene also covers the Beas River, with a riverbed full of small rocks and boulders. The Pauli image of RADARSAT-2 shows very feeble double bounce scattering depicted by red colour in the images, reflecting the location of Manali city, making it easier to spot it in the images. The surface scattering shown in blue colour in the images, is produced as a result of backscatter from a plane surface leading to a specular-like reflection property. Surface scattering is reflected mostly in the river area because of the water flowing in the channel, while at some locations, there is also double bounce and volumetric scattering occurring in the river area because of backscatter from multiple stones. The Pauli RGB images of RADARSAT-2 also shows dominant surface scattering in some parts of mountains, which might have been because of direct projection of incidence wave on the tilted surface, prompting the wave to reflect through normal to the point of contact. The area of interest, forest regions in Manali shows significant volumetric scattering component, with few pixels of double bounce scattering, and very less surface scattering. Clearly, backscatter from the top of the canopy results in multiple striking of the wave, leading to volumetric scattering. Locations where penetrating C band waves of RADARSAT-2 strike the tree trunk, then ground, and then to the receiver leads to a double bounce scattering. At other places, with specular-like reflection, surface scattering is shown.

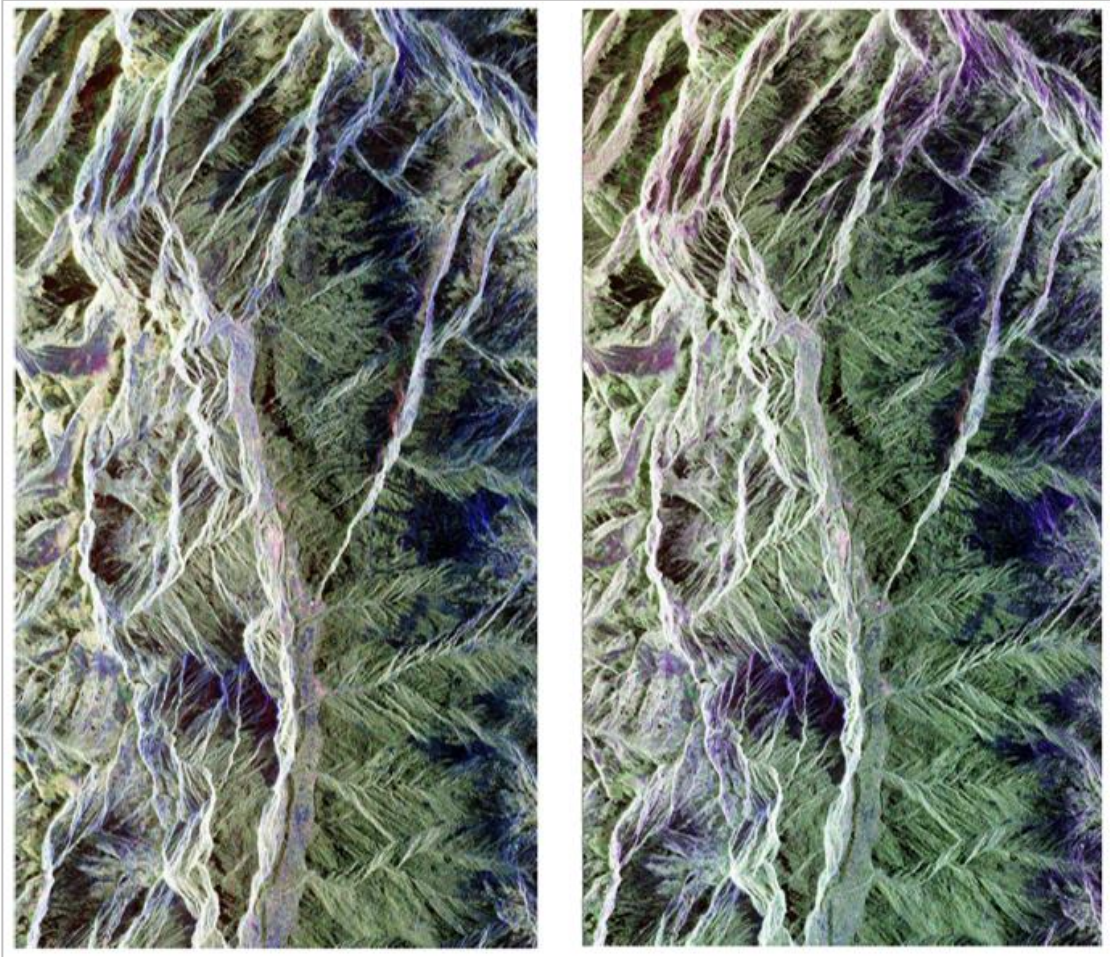


Figure 16: Pauli RGB images of RADARSAT-2 data. Left side: S1 scattering matrix, right side: S2 scattering matrix. Here, red: double bounce scattering component, blue: surface scattering component, and green: volumetric scattering component.

The Pauli RGB images of ALOS-2, shown in *figure 17*, too consists mostly of mountainous forested regions with just Manali being the only city with man-made structures. The range doppler terrain correction was not performed earlier, hence the following images appear inverted. Just like RADARSAT-2, these images are also dominated by the volumetric scattering component, while the double bounce component is present only in the city area. River consists only of the blue and red colour, with very less volumetric component. In comparison with other satellite images, the images of ALOS-2 have more frequency of occurrence of white and black pixels. While white pixels represented presence of all the three scattering components in equal amount, the black pixels represented absence of all the three scattering components. The black pixels, being shadowed region, were present only on one side of the mountains. Another drastic change in the images was the replacement of surface scattering component at multiple locations in Pauli RGB image of first acquisition to double bounce scattering component at those locations in Pauli RGB image of second acquisition.



Figure 17: Pauli RGB images of ALOS-2 data. Left side: S1 scattering matrix, right side: S2 scattering matrix. Note that, image is inverted vertically because terrain correction was not performed in this step. Here, red: double bounce scattering component, blue: surface scattering component, green: volumetric scattering component, and white: presence of all the scattering components equally.

For TerraSAR-X data, the Pauli RGB images, as shown in the *figure 18* below, are also having almost similar properties as that of ALOS-2. There is significant surface scattering shown in blue colour in the image of first acquisition, which is compensated as double bounce scattering in the image of second acquisition. This is also not terrain corrected and hence the image looks inverted. However, the area of interest shows appropriate backscattering components with the two forest regions in Manali displaying volumetric component, and the urban area displaying double bounce scattering, which are shown in the following sections.

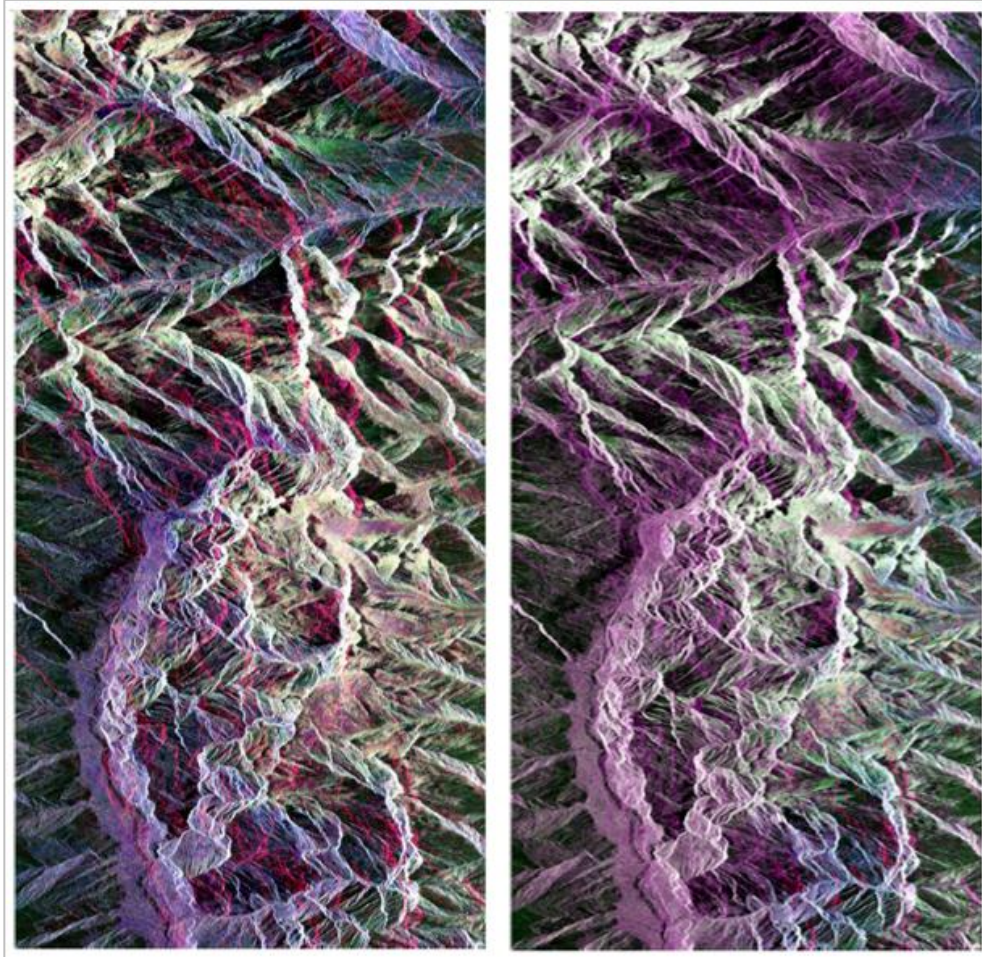


Figure 18: Pauli RGB images of TerraSAR-X data. Left side: S1 scattering matrix, right side: S2 scattering matrix. Note that, image is inverted horizontally because terrain correction was not performed in this step. Here, red: double bounce scattering component, blue: surface scattering component, green: volumetric scattering component.

5.2. Obtaining the T6 matrix

Multi-looking was performed on the co-registered image pairs to convert the pixels into square pixels with appropriate range and azimuth looks. For RADARSAT-2 images, a ground range square pixel of 10.14 meter was obtained with a range look of 1 and an azimuth look of 2. With same number of azimuth and range looks, a ground range square pixel size of 5.77 meters was obtained for ALOS-2 satellite images. However, for TerraSAR-X, the azimuth and range look were unitary, and the ground range pixel size remained 2.49 meters. The scattering matrices S1 and S2 were generated, and the process followed up with the generation of the Pauli feature vectors. In a PolInSAR system, the T6 coherency matrix constitutes the polarisation and interferometric information, which was generated using the Pauli feature vectors, as explained in the methodology section. Subset of the multi-looked Pauli RGB images of the [T11] and [T22] components are shown in the following *figures 19, 20, and 21*, for visual understanding of the scene. As explained earlier, the 3x3 [T11] matrix depicts the polarisation property of the first pass image, while the [T22] matrix depicts the polarisation property of the second pass image.

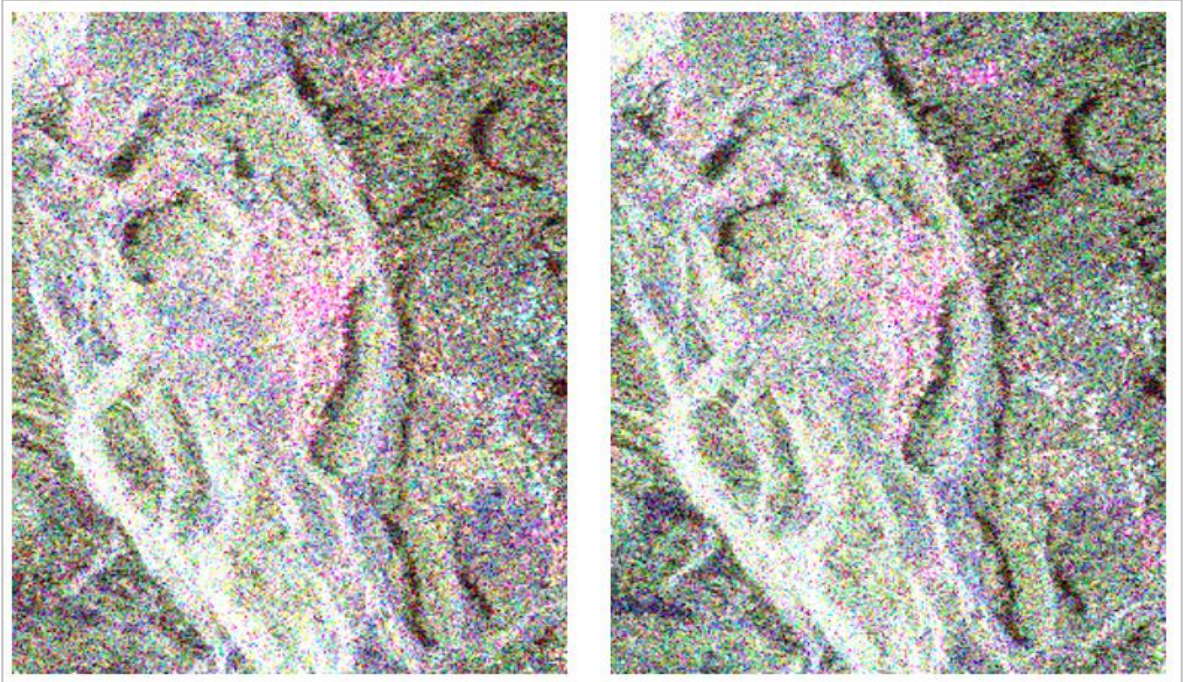


Figure 19: Zoomed in portion of multilooked Pauli RGB image of RADARSAT-2 data after the generation of T6 coherency matrix. Left: T1, right: T2. Significant double bounce scattering (red coloured pixels) can be seen in the Manali city with a dominant volumetric scattering (in green colours) in the forest areas. Surface scattering in blue colours can also be seen in many parts of the image.

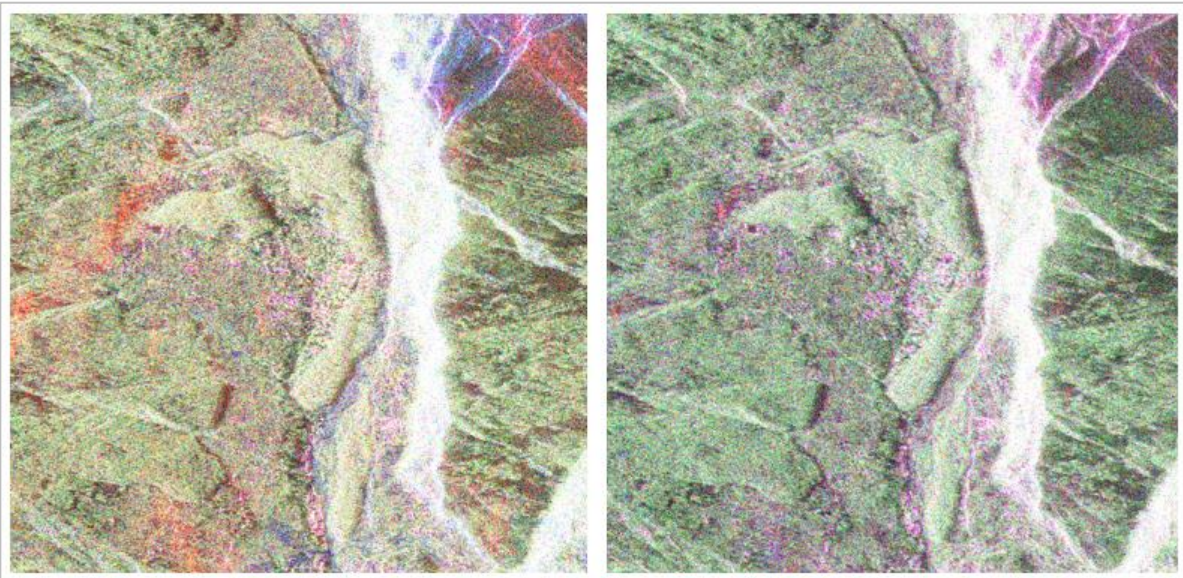


Figure 20: Zoomed in portion of multilooked Pauli RGB image of ALOS-2 data after the generation of T6 coherency matrix. Left: T1, right: T2. Whitish colours imply the presence of all the three types of scattering in the area. Forests have only volumetric scattering (green coloured pixels), while urban area has dominant double bounce scattering along with volumetric scattering at some places.

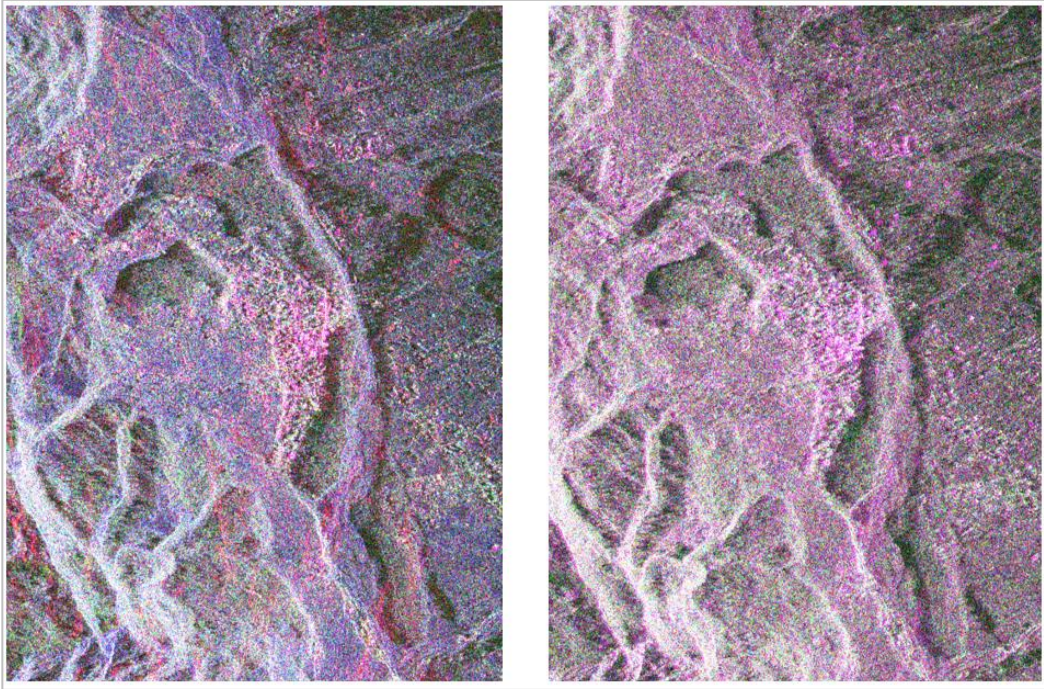


Figure 21: Zoomed in portion of multilooked Pauli RGB image of TerraSAR-X data after the generation of T6 coherency matrix. Left: T1, right: T2. While T1 shows significant surface scattering all over the area, the same area gets substituted to double bounce scattering. Though, urban area cannot be distinguished looking at the T2 RGB image, forests can still be distinguished easily.

5.3. Baseline estimation and k_z calculation

The tables below show the parameters of each satellite used to estimate the baseline component. The temporal decorrelation due to temporal gap in second acquisition cannot be compensated and hence must be ignored in the study. Since the trees in the region are matured, we can expect almost no changes in the forest region during that time gap.

Table 2: Parameters of RADARSAT-2 satellite.

PARAMETERS OF RADARSAT-2	VALUES
Perpendicular baseline	147.66 meters
Temporal baseline	24 days
2π Height of ambiguity	60 meters
Estimated baseline	216.717 meters

Table 3: Parameters of ALOS-2 satellite.

PARAMETERS OF ALOS-2	VALUES
Perpendicular baseline	145.07 meters
Temporal baseline	28 days
2π Height of ambiguity	60 meters
Estimated baseline	843.76 meters

Table 4: Parameters of TerraSAR-X data.

PARAMETERS OF TerraSAR-X	VALUES
Perpendicular baseline	269.872 meters
Temporal baseline	24 days
2π Height of ambiguity	60 meters
Estimated baseline	103.399 meters

Using the baseline component along with the wavelength, slant range and incidence angle, the value of vertical wavenumber (k_z) was calculated. For TerraSAR-X it was in the range of 0.101 and 0.108. The value of k_z for ALOS-2 satellite data was in the range of 0.099 and 0.11, while for RADARSAT-2, its value was between 0.101 and 0.108.

5.4. Complex coherences in various polarisation basis

From the generated T6 coherence matrix, the complex coherences in various polarisation basis were obtained, using the PolSARpro software, for the three satellite data pairs. *Equation 2.30* shows the two possible polarisation pairs, ω_1 and ω_2 , that must have maximum separation to nominate the best possible polarisation that could represent the ground and top of the canopy.

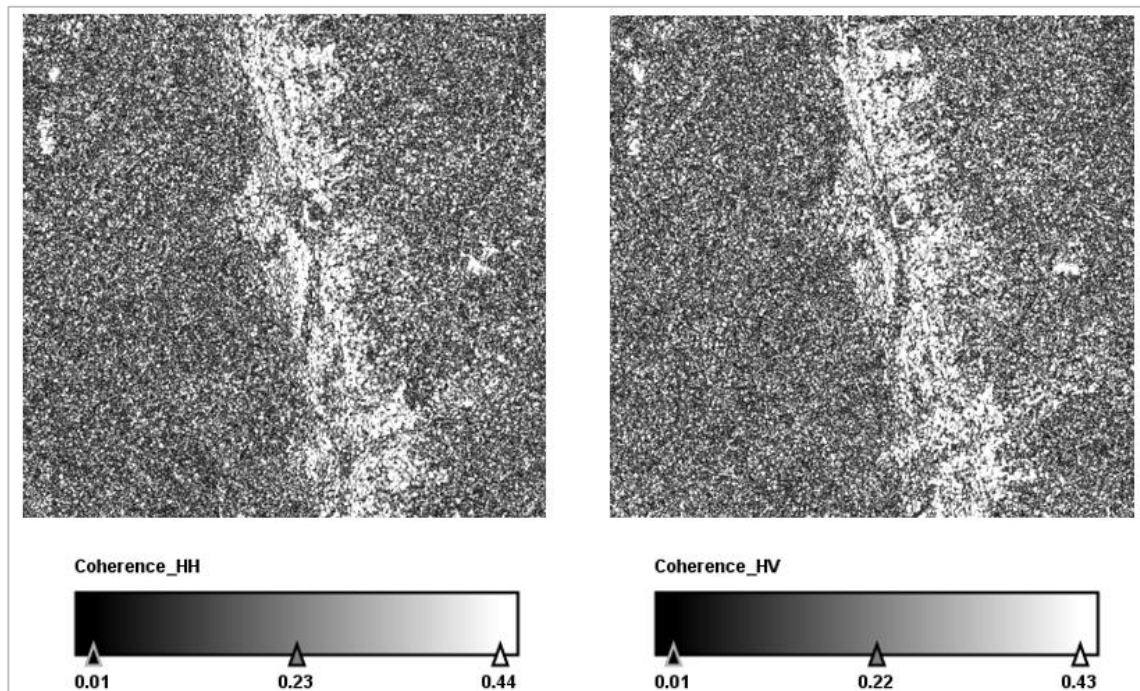


Figure 22: Subset of coherence values of HH (left) and HV (right) components of the linear polarisation basis for RADARSAT-2 satellite.

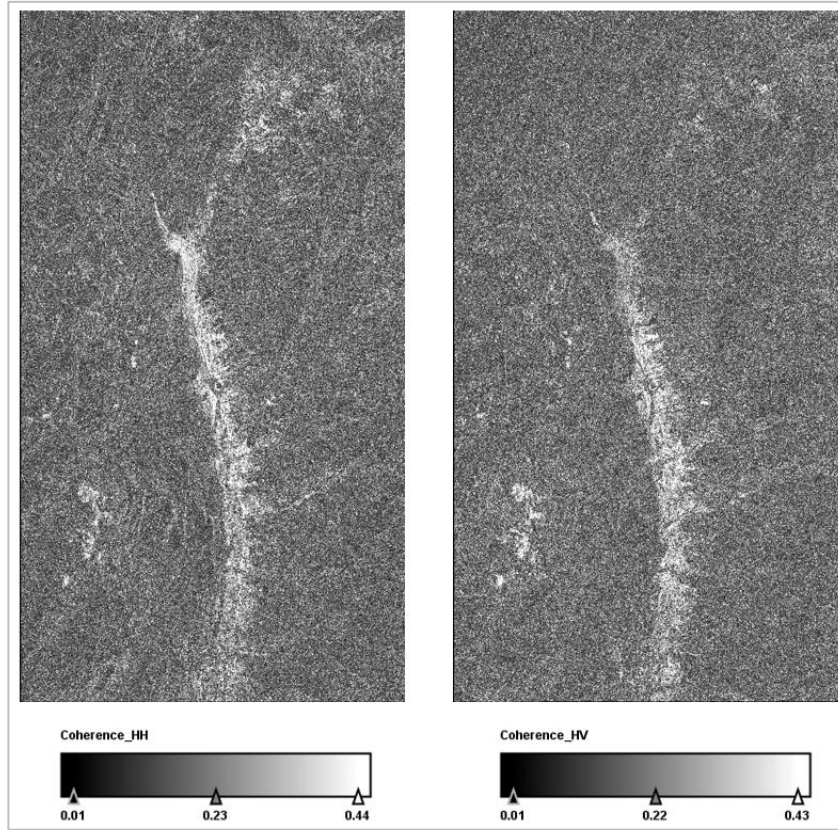


Figure 23: Coherence values of HH (left) and HV (right) components of the linear polarisation basis for RADARSAT-2 satellite. 95% of pixels lie between a range of coherence value 0.01 and 0.44 for both HH and HV polarisation combination.

For RADARSAT-2 data, the complex coherences of the three different polarization combinations of the linear polarisation basis, depicted by HH and HV are shown in the *figure 23*, while VV is shown in the *figure 24*, along with the RGB colour composite image of the coherences in these polarisations, where HH is shown in the red colour, corresponding to the double bounce scattering, VV is shown in the blue colour corresponding to the surface scattering, while HV is shown in the green colour corresponding to the volumetric scattering. A histogram of the coherences in the linear polarisation basis is also shown in *figure 25*. The histogram shows all the three polarization combinations having almost the similar coherence values, with VV having slightly lesser than HH and HV.

A subset of the full image showing the part of the Manali city, and its forest is shown in the *figures 22 and 26*. It shows the forests having one of the lowest coherence amplitude values, mainly because of the temporal decorrelation (Shane Robert Cloude & Papathanassiou, 1998; Khati & Kumar, 2014). Apart from it, the fact that forest regions offers volumetric scattering the most, because of multiple backscatter from the top of the canopy, the volumetric decorrelation factor increases giving the area a low coherence value (Khati & Kumar, 2014; Sadeghi et al., 2011). Other features in the region such as the dry riverbed and the urban areas have relatively high coherence amplitude since there are minimum changes in those regions. The temporal decorrelation in such regions is lowest. In the figure, because of vicinity of multiple urban settlements, which

led to multiple scattering and bouncing of the wave, the original double bounce scattering components got compensated by their volumetric counterparts. in the urban region of HV polarised coherence map.

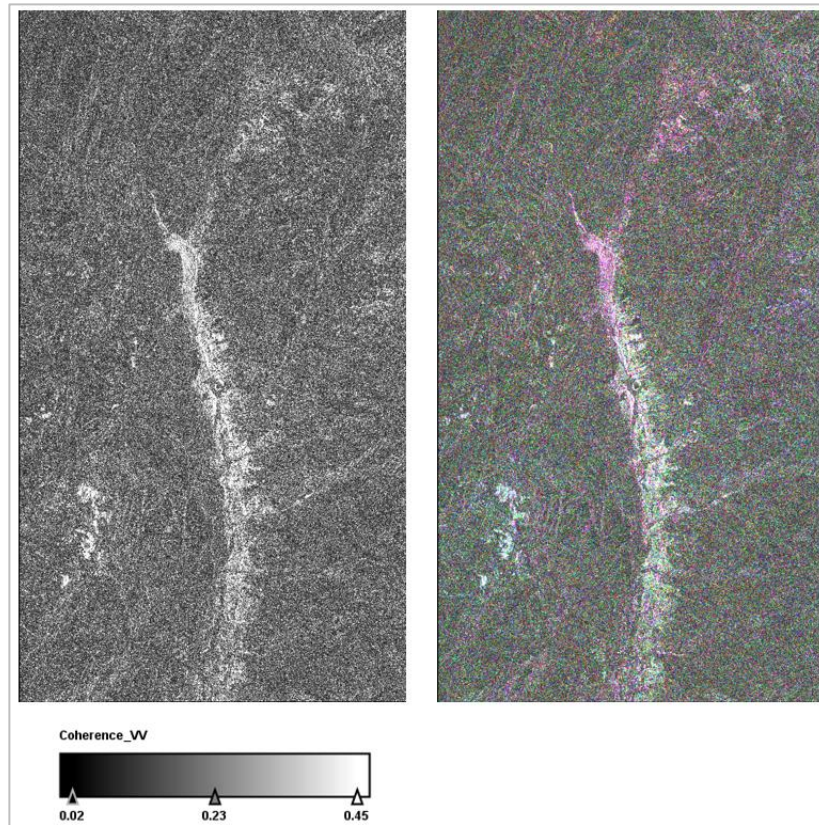


Figure 24: Left: Coherence values of VV component of the linear polarisation basis for RADARSAT-2 satellite. Range of coherence is between 0.02 and 0.45 for this polarisation combination. Right: RGB composite image for interpretation of the different scatterings in linear polarisation basis, with red representing the double bounce scattering (HH), green representing the volumetric scattering (HV) and blue representing the surface scattering (VV).

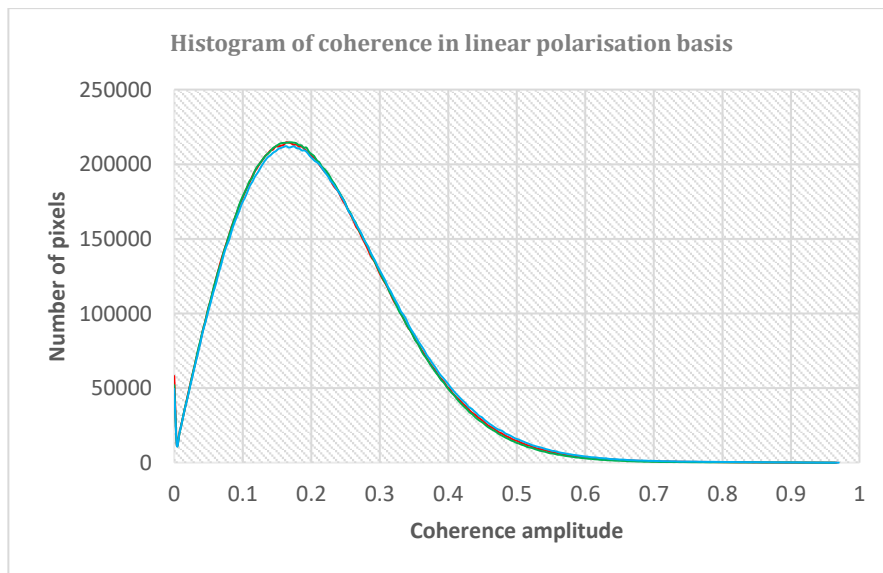


Figure 25: Histogram showing frequency of various components of linear polarisation basis with their coherence values for RADARSAT-2. Red represents HH, green represents HV, and blue represents VV.

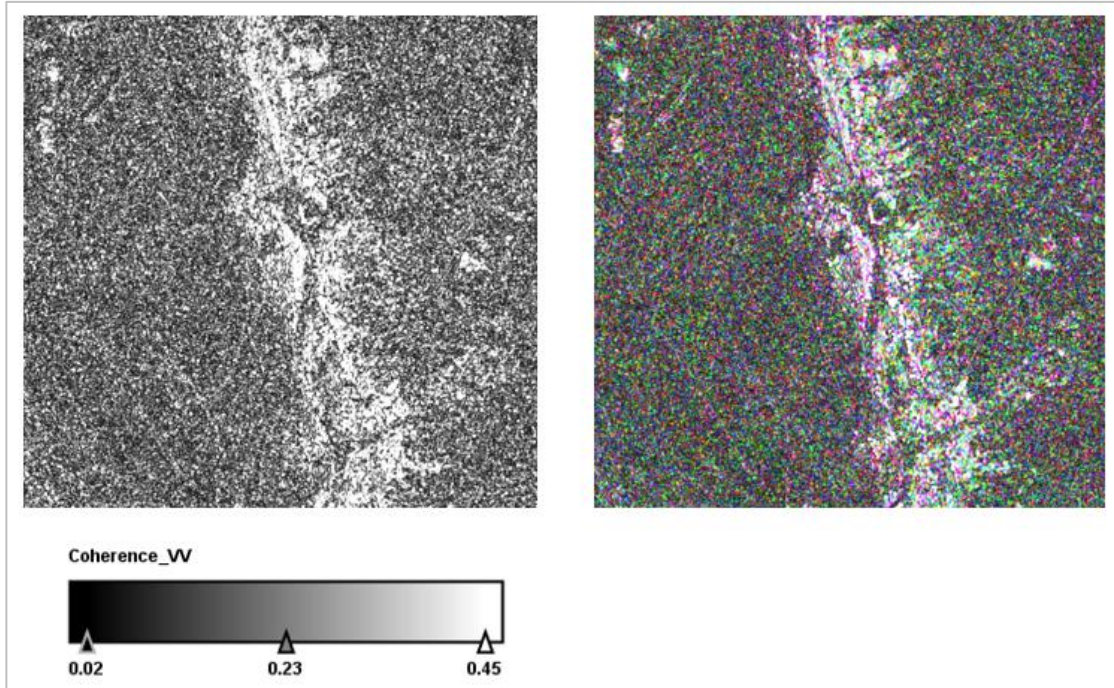


Figure 26: Subset of **left:** coherence values of VV component of the linear polarisation basis for RADARSAT-2 satellite, and **right:** RGB composite image of linear polarisation basis. Red: double bounce scattering, Green: volumetric scattering, Blue: surface scattering. Features such as the forests of Manali, Manali city, Apple orchards in the city are clearly visible in RGB image.

For the same satellite, the complex coherences of the three different polarization combinations of the Pauli polarisation basis, depicted by HH+VV and HV+VH are shown in the *figure 27*, while HH-VV along with their RGB colour composite image is shown in the *figure 29*. There, HH-VV is shown in the red colour, corresponding to the double bounce scattering, HH+VV is shown in the blue colour corresponding to the surface scattering, while HV+VH is shown in the green colour corresponding to the volumetric scattering. Significant surface scattering is observed at multiple locations, especially near the riverbed. A histogram of the coherences in the Pauli polarisation basis is also shown in *figure 31*.

A subset of the full image showing the part of the Manali city, and its forest are shown in the *figures 28 and 30*. Urban areas and dry riverbed have the maximum coherence values in the HH+VV polarisation combination, while forest shows very low coherence in all the three polarisation combinations because of temporal decorrelation (Shane Robert Cloude & Papathanassiou, 1998; Khati & Kumar, 2014) and volumetric decorrelation (Khati & Kumar, 2014; Sadeghi et al., 2011). Unlike the previous linear polarisation basis, the urban area in this region exhibits surface scattering component apart from its usual double bounce scattering. Even the river channel can be observed clearly upon seeing the blue coloured surface scattering component next to the Manali forests.

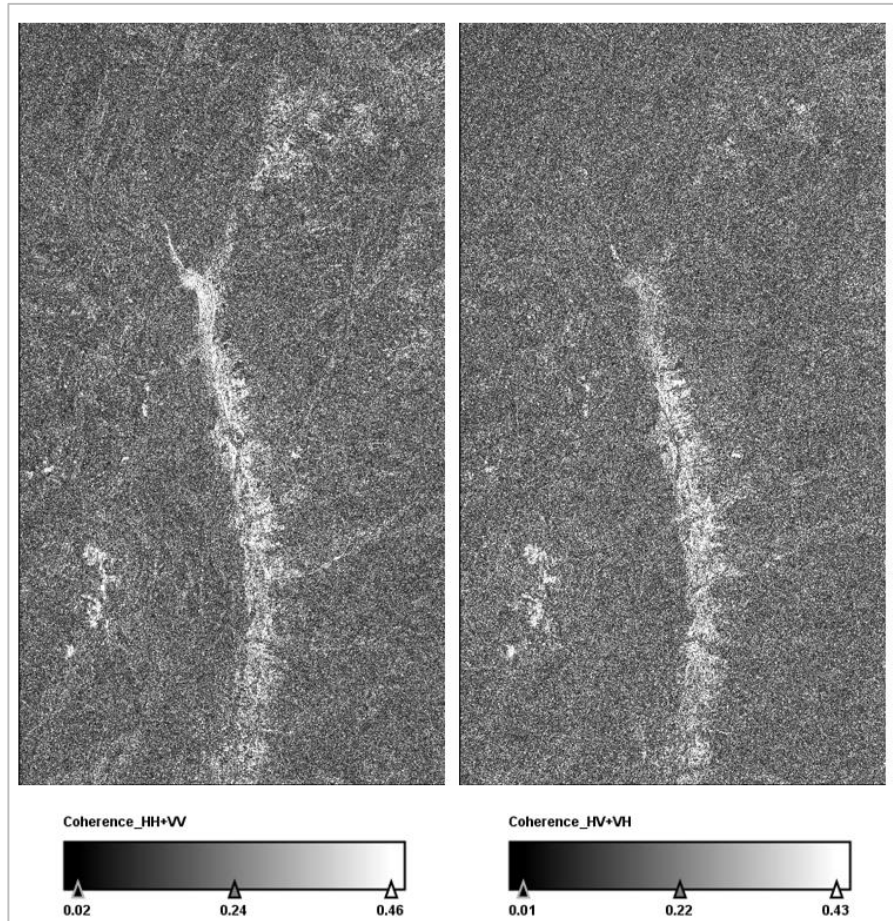


Figure 27: Coherence values of HH+VV (left), with 95% of pixels within the range of 0.02 and 0.46 coherence, and HV+VH (right), with 95% of pixels within the range of 0.01 and 0.43 coherence, components of the Pauli polarisation basis for RADARSAT-2 satellite.

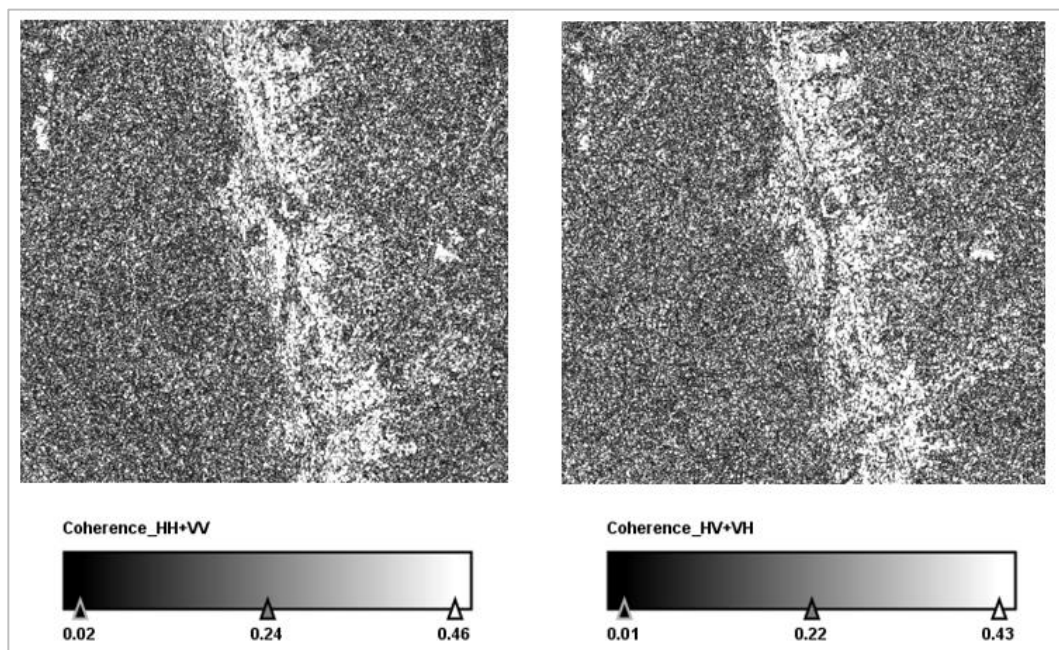


Figure 28: Subset of coherence values of HH+VV (left) and HV+VH (right) components of the Pauli polarisation basis for RADARSAT-2 satellite.

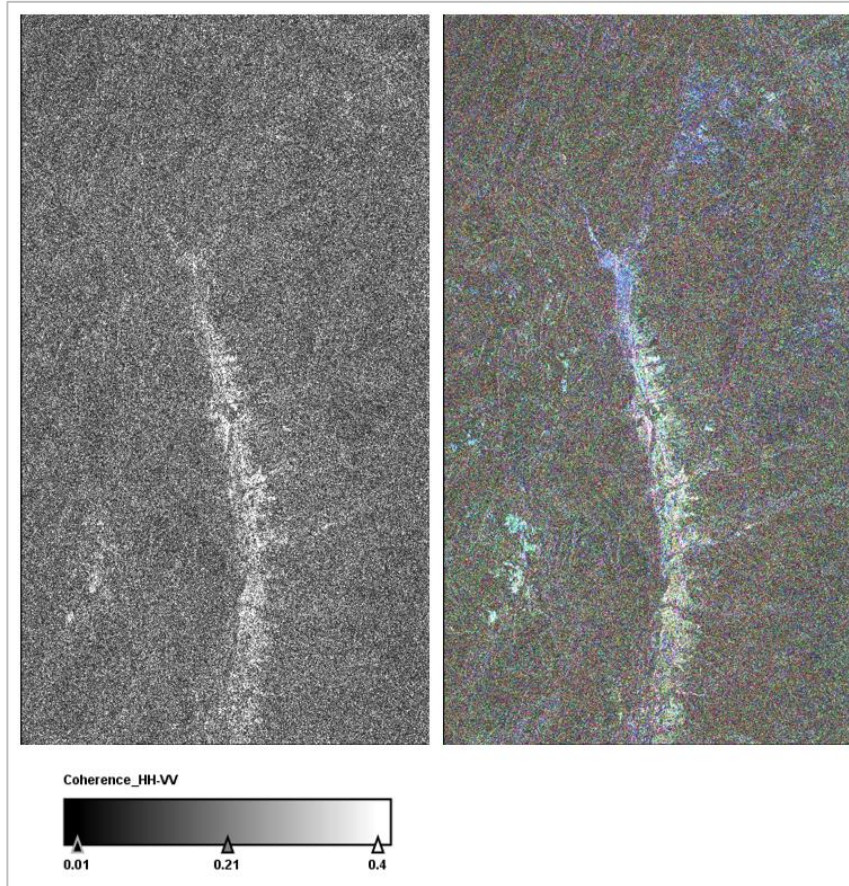


Figure 29: Left: Coherence values of HH-VV, with 95% of pixels within 0.01 and 0.4 coherence value, component of the Pauli polarisation basis for RADARSAT-2 satellite. Right: RGB composite image for interpretation of the different scatterings in Pauli polarisation basis, with red representing HH-VV, blue representing HH+VV, and green representing HV+VH.

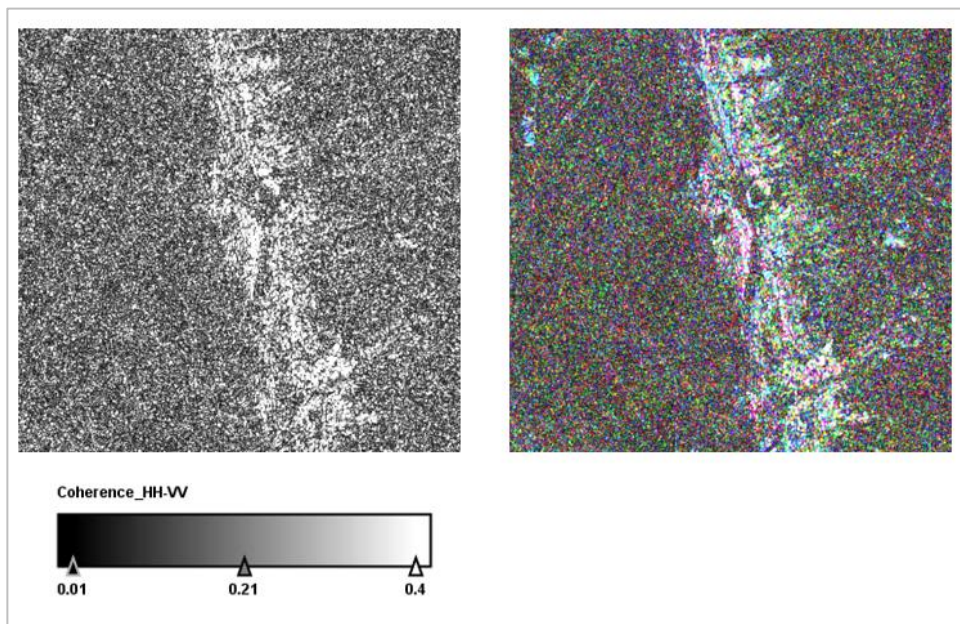


Figure 30: Subset of left: coherence values of HH-VV component of the Pauli polarisation basis for RADARSAT-2 satellite, and right: RGB composite image of Pauli polarisation basis. The main difference with the linear basis RGB composite is that this has higher surface scattering component (in blue colour).

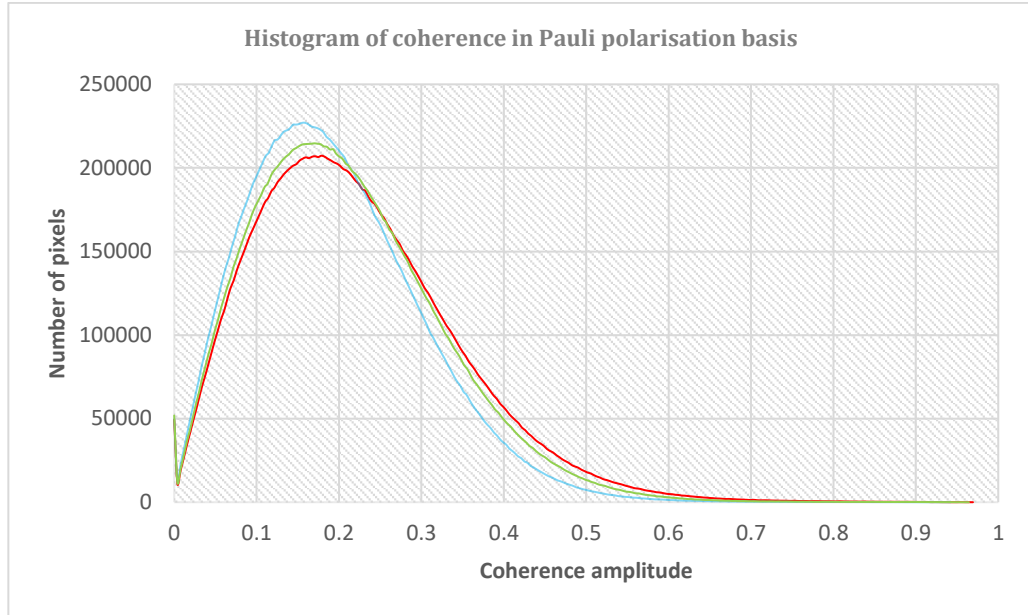


Figure 31: Histogram showing frequency of various components of Pauli polarisation basis with their coherence values for RADARSAT-2. Red represents HH-VV, green represents HV+VH, and blue represents HH+VV.

The third polarisation basis, circular polarisation basis was then used which consist of three polarisation combinations, namely LL, LR, and RR. While LL and LR are shown in *figure 32*, the RR along with their RGB colour composite is shown in the *figure 34*. The RGB composite consist of LL depicted as the double bounce scattering component with red colour, LR depicted as the volumetric component with green colour, while RR depicted the surface scattering with blue colour. A histogram of the coherences in the circular polarisation basis is also shown in *figure 33*. In LL and RR component coherence maps, the dry riverbed region has a very low coherence value, which suggests the presence of water since water exhibits low coherence value due to temporal decorrelation (Shane Robert Cloude & Papathanassiou, 1998; Khati & Kumar, 2014). The RGB composite image clearly shows the dominance of LR component, even in the dry riverbed regions. Urban area in this basis is shown as all white region, so the presence of all the scattering with high coherence value is the possibility. Alike the previous two polarisation basis, the volumetric component in forest regions exhibit the lowest coherence due to temporal and volumetric decorrelation.

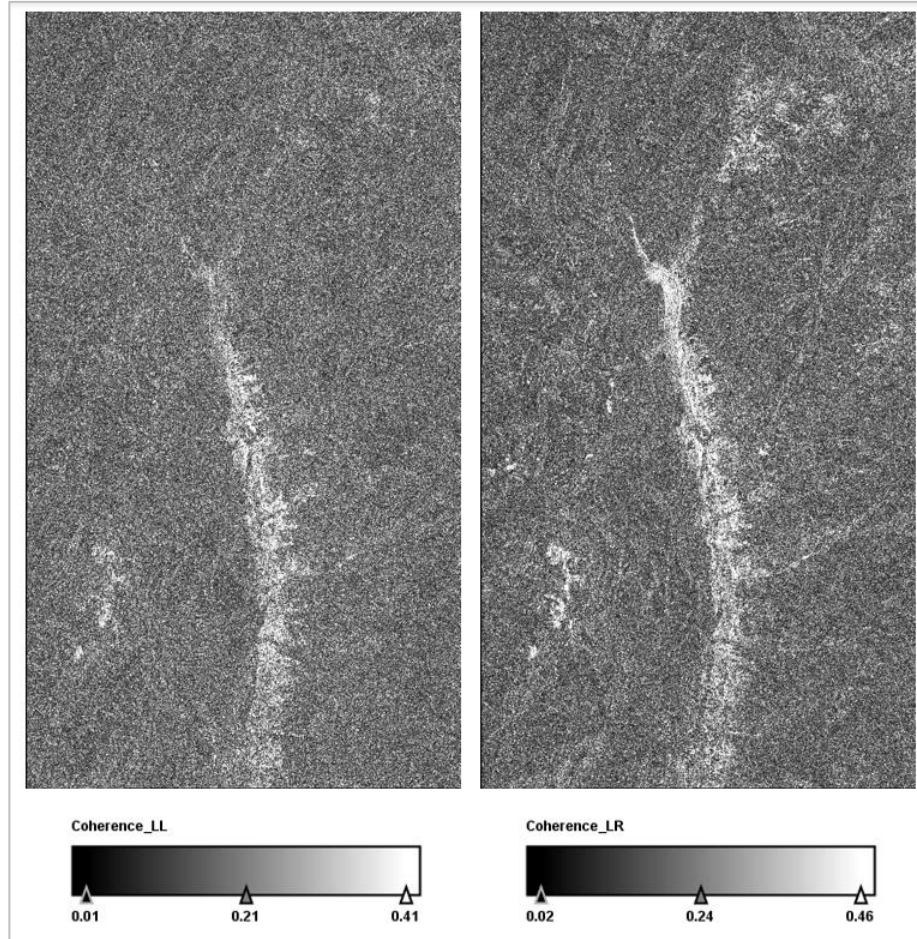


Figure 32: Coherence values of LL (left), with 95% of pixels within the range of 0.01 and 0.41 coherence, and LR (right), with 95% of pixels within the range of 0.02 and 0.46 coherence, components of the circular polarisation basis for RADARSAT-2 satellite.

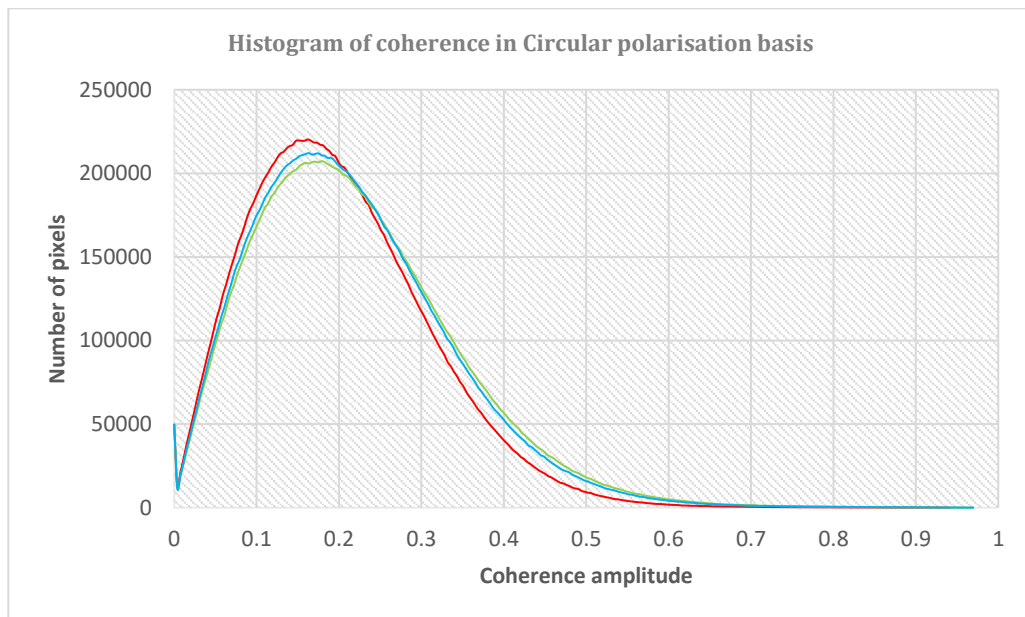


Figure 33: Histogram showing frequency of various components of circular polarisation basis with their coherence values for RADARSAT-2. Red represents LL, green represents LR, and blue represents RR.

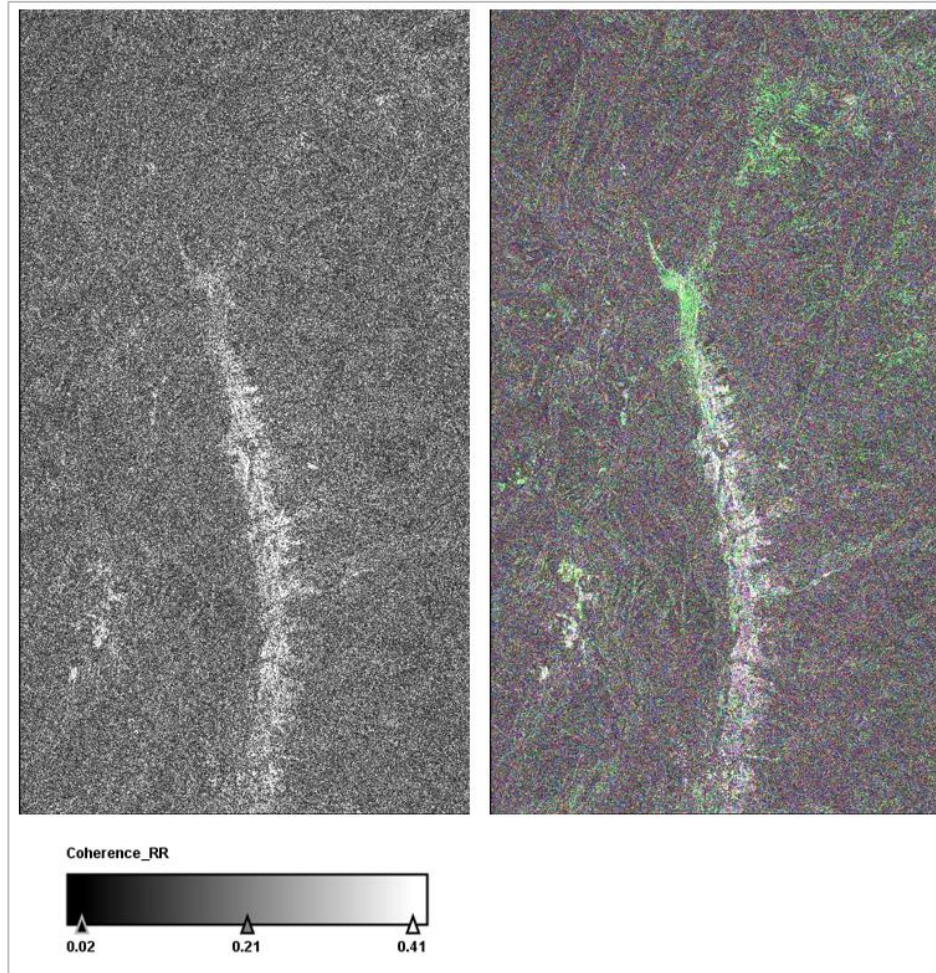


Figure 34: Left: Coherence values of RR, with 95% of pixels within 0.02 and 0.41 coherence value, component of the circular polarisation basis for RADARSAT-2 satellite. Right: RGB composite image for interpretation of the different scatterings in circular polarisation basis, with red representing LL, blue representing RR, and green representing LR.

The last polarisation basis used on the RADARSAT-2 data was the optimal basis with three polarisation combinations, namely Opt1, Opt2, and Opt3. Distinctive from all the other basis, this basis uses the concept of dividing combinations based on their coherence amplitude. This can be seen in the histogram, *figure 36*, of the coherences in these three-polarisation combination. While Opt1 has the highest coherence values, Opt3 has the lowest with Opt2 coming in between. Another property of the optimal basis shows a great number of pixels having coherence value 1, which can be seen in the histogram as well. The RGB composite image, as shown in *figure 37*, suggest an all-white urban and dry riverbed region. The coherence values of these regions in the three polarisation combinations also shows the highest coherence values. The pixels with coherence 1 may be these urban regions or dry riverbed channels.

Opt1 and Opt2 are shown in *figure 35*, while Opt3 along with the RGB composite image are shown in *figure 37*. Based on the coherence values, the three combinations can be divided in the manner that Opt1 could represent the maximum coherence exhibiting feature, such as that exhibited in the urban areas or dry riverbed due to double bounce scattering. Opt2 ranges between 0.15 and 0.49 coherence values, which could represent the volumetric scattering, with forest areas depicting the lowest coherences, while multiple striking

in dense urban areas depicting highest coherence in this combination. Opt3, with the lowest coherence value must be the surface scattering that usually depicts water surface.

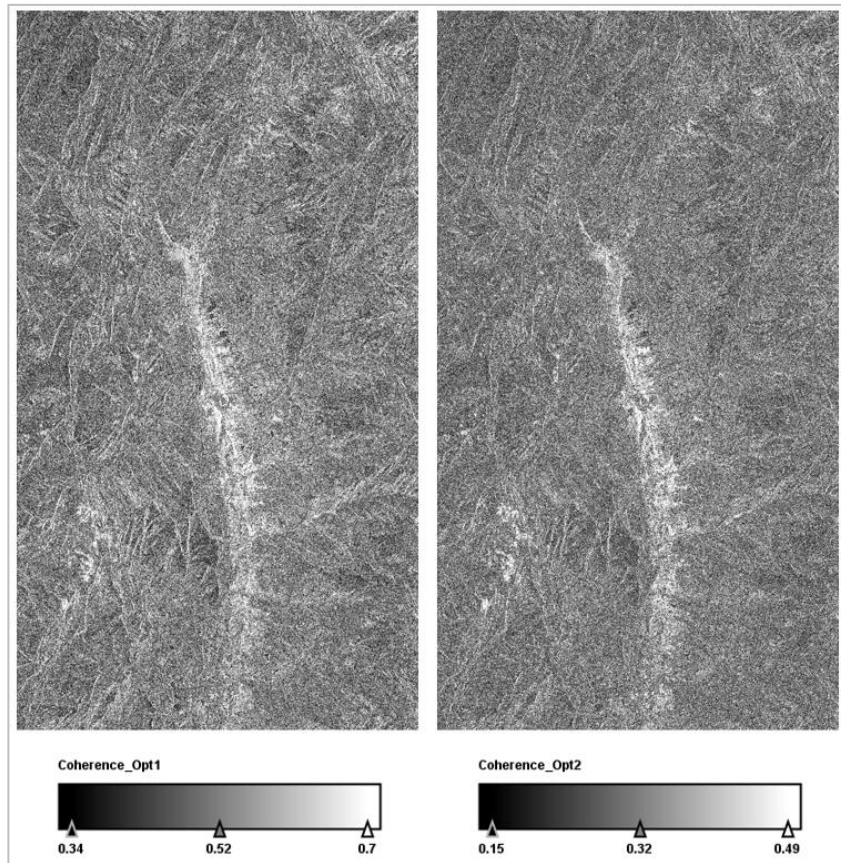


Figure 35: Coherence values of Opt1 (left), with 95% of pixels within the range of 0.34 and 0.7 coherence, and Opt2 (right), with 95% of pixels within the range of 0.15 and 0.49 coherence, components of the optimal polarisation basis for RADARSAT-2 satellite.

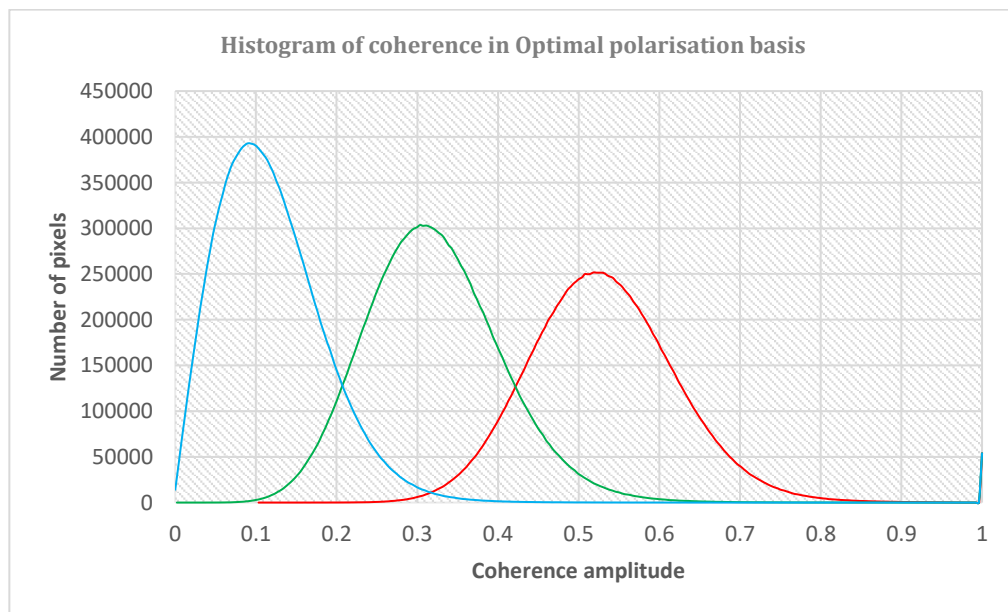


Figure 36: Histogram showing frequency of various components of optimal polarisation basis with their coherence values for RADARSAT-2. Red represents Opt1, green represents Opt2, and blue represents Opt3.

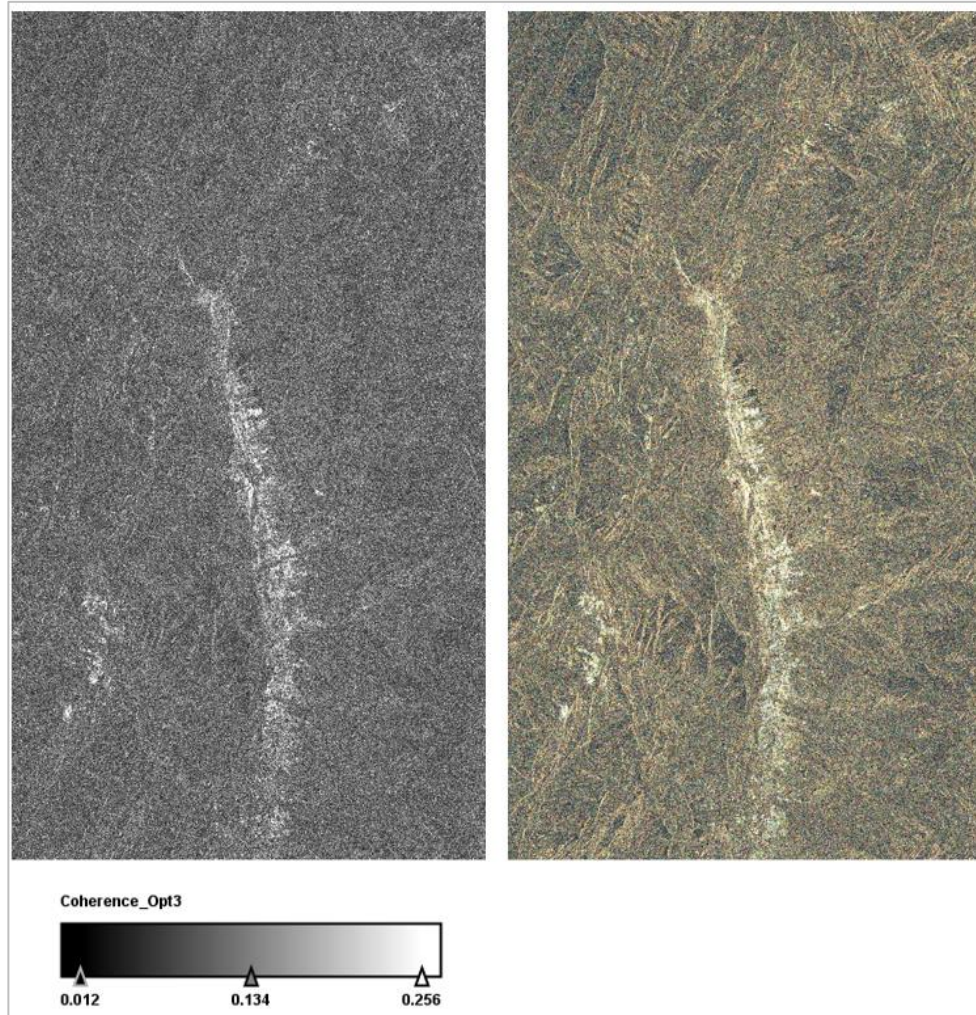


Figure 37: Left: Coherence values of Opt3, with 95% of pixels within 0.012 and 0.256 coherence value, component of the optimal polarisation basis for RADARSAT-2 satellite. Right: RGB composite image for interpretation of the different scatterings in optimal polarisation basis, with red representing Opt1, blue representing Opt3, and green representing Opt2.

For ALOS-2 data, *figure 38* shows the coherence values of various polarisation combinations of the linear polarisation basis. Manali is located in hills and is covered with thick forest ranges on all sides. Thus, the satellite imagery consisted mostly of forest areas. Just like the coherence values of the previous satellite image, even this shows a high coherence value in urban areas and the riverbed in HV and VV polarisation combinations. The RGB composite of linear polarisation basis in *figure 38 (iv)* depicts the riverbed and the urban areas having a bluish green colour, white could represent the presence of surface scattering from plane surfaces and volumetric scattering from dense urban locality, or from multiple striking of the wave at the stones in the dry riverbed. The histogram shown in *figure 39* shows the domination of the double bounce scattering pixels (shown in red colour).

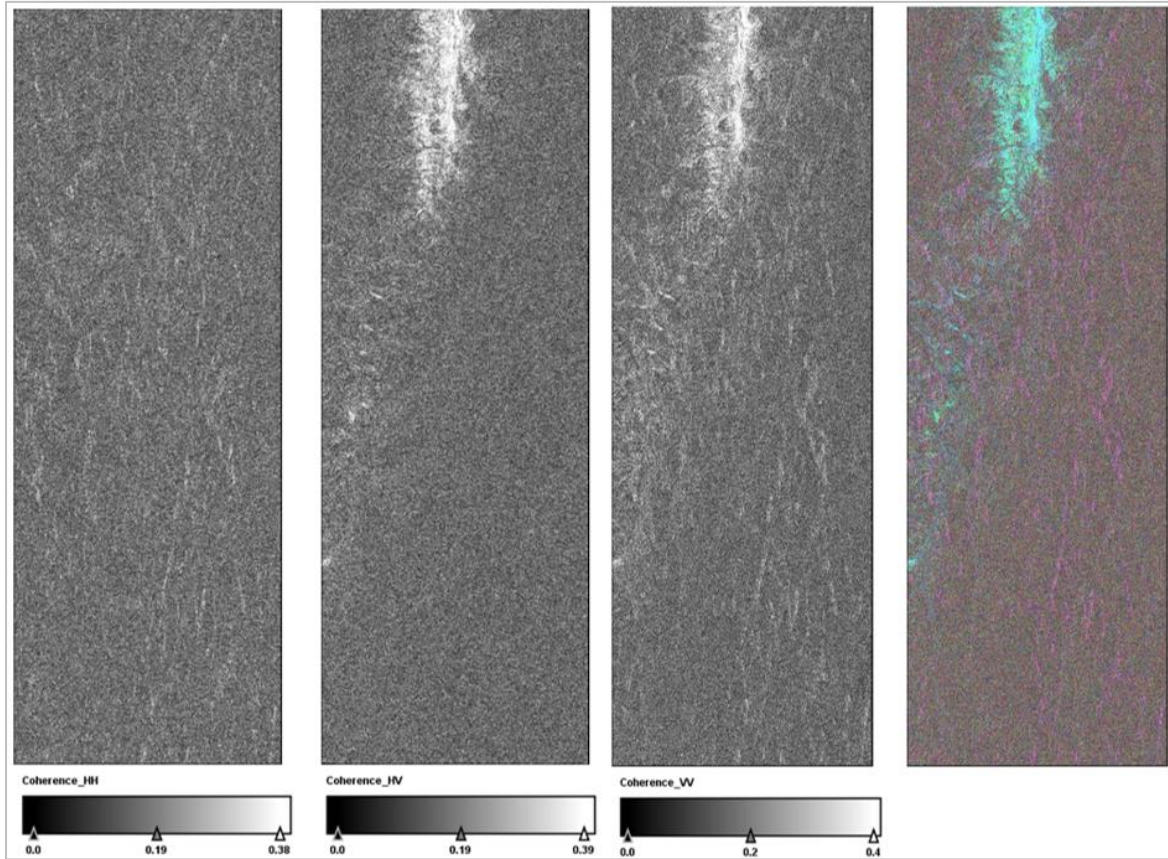


Figure 38: Coherence values of HH (i), HV (ii), and VV (iii) components of the linear polarisation basis for ALOS-2 satellite. 95% of pixels lie between a range of coherence value 0 and 0.38, 0 and 0.39, and 0 and 0.4, for HH, HV, and VV polarisation combination. RGC composite image (iv) for interpretation of the different scatterings in linear polarisation basis, with red representing the double bounce scattering (HH), green representing the volumetric scattering (HV) and blue representing the surface scattering (VV).

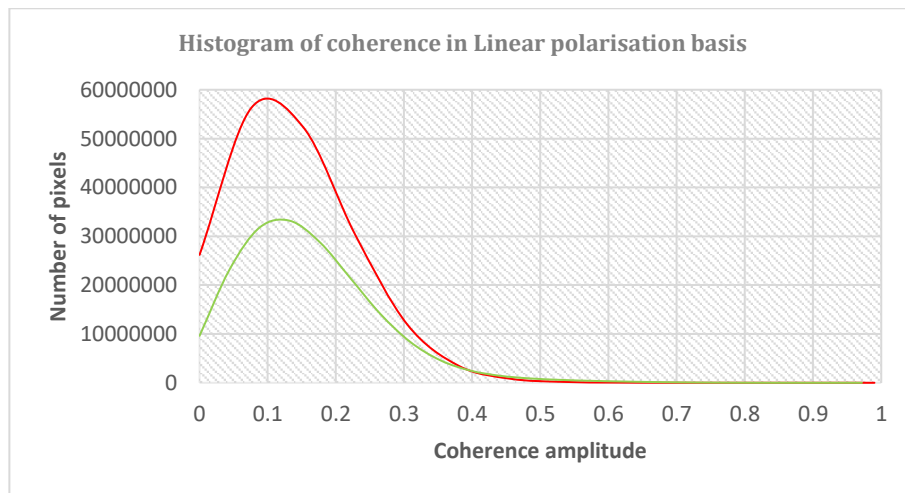


Figure 39: Histogram showing frequency of various components of linear polarisation basis with their coherence values for ALOS-2. Red represents HH, and green represents HV.

In Pauli polarisation basis, most of the features have similar information as that of the linear polarisation basis. The double bounce scattering components of both the basis, HH of linear, and HH-VV of Pauli, had the lowest coherence values. Both had low coherence even for the urban area and the riverbed. Just like the

previous polarisation basis, even in this, the river channel is clearly described by a set of blue coloured pixels, which exhibit the surface scattering property. The coherences in various combinations are shown in *figure 40*, while the histogram is shown in *figure 41*.

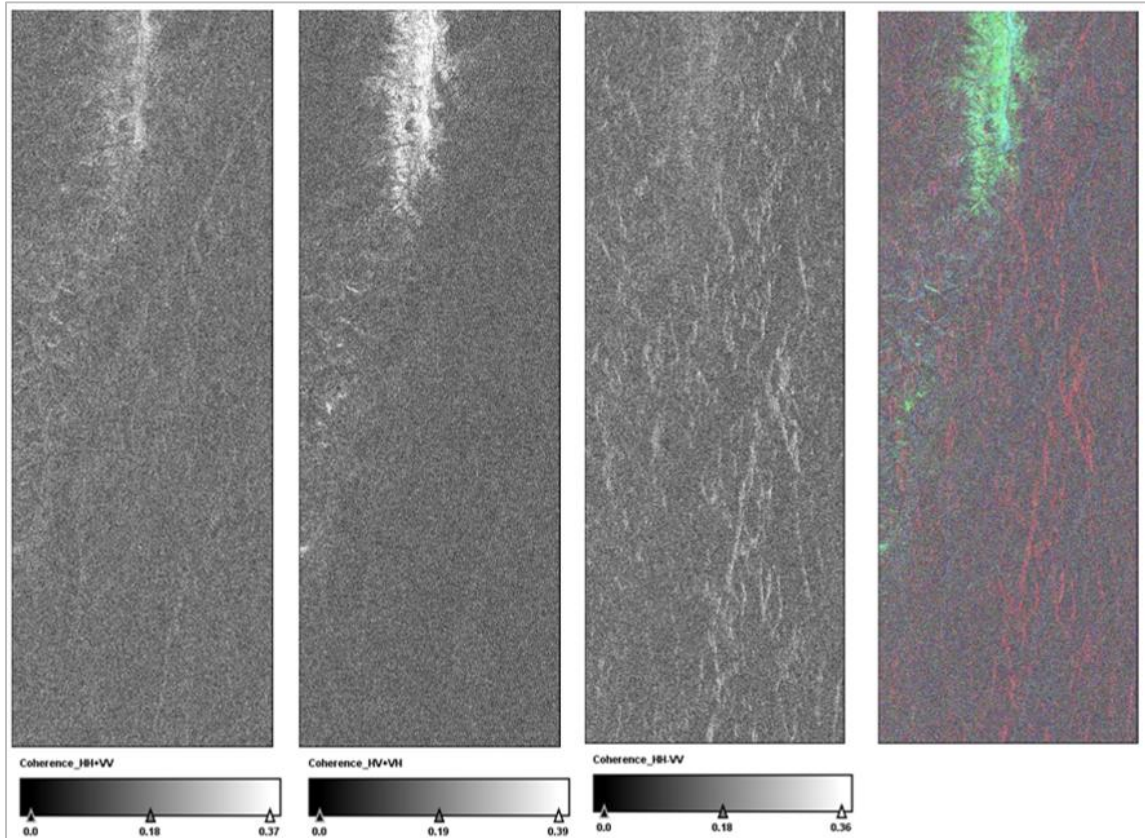


Figure 40: Coherence values of HH+VV (i), with 95% of pixels within the range of 0 and 0.37 coherence, HV+VH (ii), with 95% of pixels within the range of 0 and 0.39 coherence, HH-VV (iii), with 95% of pixels within 0 and 0.36 coherence value and components of the Pauli polarisation basis for ALOS-2 satellite. RGB composite image (iv) for interpretation of the different scatterings in Pauli polarisation basis, with red representing HH-VV, blue representing HH+VV, and green representing HV+VH.

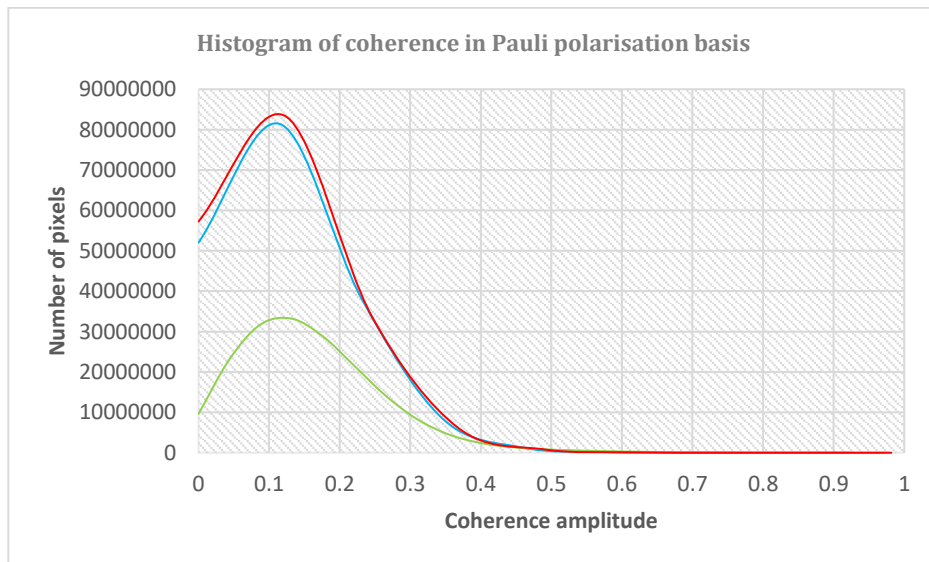


Figure 41: Histogram showing frequency of various components of Pauli polarisation basis with their coherence values for ALOS-2. Red represents HH-VV, and green represents HV+VH, and blue represent HH+VV.

In the circular polarisation basis, the only difference is the higher frequency of occurrence of the volumetric component, LR, as compared to the volumetric components of the previous two basis. This also has a superior occurrence that its counterparts, the double bounce component, described by LL and shown in red colour in the histogram and the surface scattering component, described by RR and shown in the blue colour in the following histogram. The same can be seen in *figure 42*, where the green coloured line shows the frequency of occurrence.

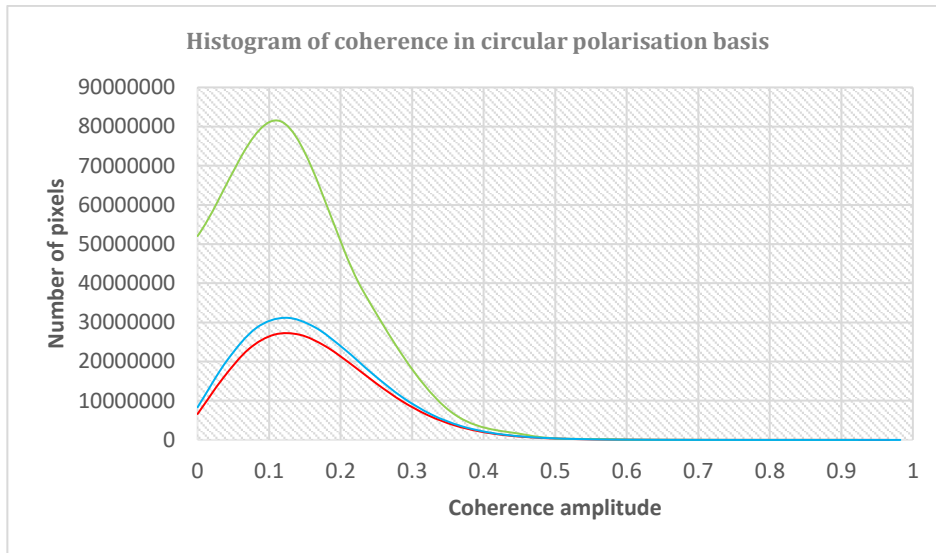


Figure 42: Histogram showing frequency of various components of circular polarisation basis with their coherence values for ALOS-2. Red represents LL, and green represents LR, and blue represent RR.

The last basis used in the ALOS-2 data was the optimal basis, which is divided into different combinations based on the value of coherence (Khatri & Kumar, 2014). The Opt1 combination has the highest coherence value, shown as the red colour in the following histogram (*figure 43*), followed by the Opt2 which has a peak at around 0.27, while the lowest coherence is given to Opt3 whose peak can be seen at less than 0.1. The double bounce has the most number of pixels in this basis

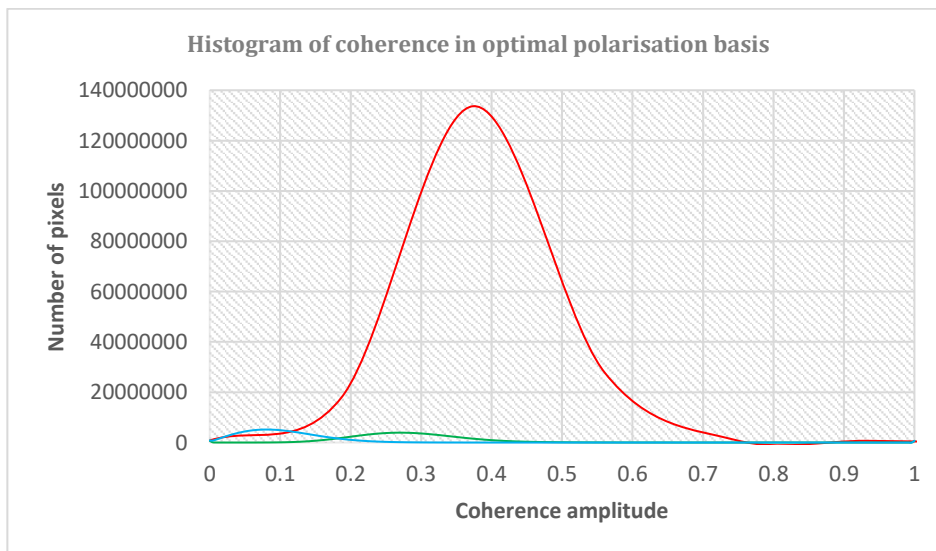


Figure 43: Histogram showing frequency of various components of optimal polarisation basis with their coherence values for ALOS-2. Red represents Opt1, and green represents Opt2, and blue represent Opt3.

5.5. Forest height

Using the complex coherences in different polarization basis, and the generated k_z file, forest height was obtained for the Three Stage Inversion process. For Coherence Amplitude Inversion process, backscattering from the top of the canopy and the ground was assumed to be from the Pauli basis with HV+VH representing the top of the canopy (the volumetric scattering component), while HH+VV representing the ground surface (the surface scattering component). Both the techniques used the ground to volume scattering ratio, where a higher value of this ratio implied influence of ground scattering (surface scattering) more, while a lower value of this ratio meant presence of volumetric component (means backscatter is more from the top of the canopy). The generated forest maps thus consisted of height values stored in their pixels, with pixel dimensions depending upon the type of data. While RADARSAT-2 and ALOS-2 had a coarser spatial resolution, TerraSAR-X data had a much finer spatial resolution. Thus, it was concluded that a greater number of tree heights were averaged and stored in a single pixel in RADARSAT-2 data, prompting to the loss of data. In comparison to it, lesser number of trees were averaged in a single pixel in ALOS-2 and the least number of trees were averaged in a single pixel in TerraSAR-X data.

The height map of the forests in Manali city along with the nearby regions, using the RADARSAT-2 data showed the models had estimated heights for dry riverbed and urban area as well which is a flaw in these techniques. Khati in his study (Khati & Kumar, 2014), suggested a new improvised method of estimating height of forests, without estimating the height of urban areas and dry riverbeds. It was a two-step process where at first, based on the coherence values, features were segregated, and then finally using the different backscattering intensities of such features, water and urban areas got delineated from the forest region. For example, water usually has the lowest coherence value, followed by forest areas, with urban areas having the maximum coherence because of temporal decorrelation. But still interference between water and forest remains, which can be overcome using the second step. Water, having a specular reflection backscatters the least, while urban areas and permanent structures have the most backscatter due to double bounce scattering. Forest lies in between the two because of volumetric scattering component in them. Using the T11 component of the T6 matrix shown in *equation 2.24*, a threshold of 0.1 is chosen so that backscatter intensity below this remains for water, while any value above it (and below that of the double bounce scattering) could be assigned to forest areas. A subset image showing the forest height maps of the two ranges, Ram Bagh, and Van Vihar for both the techniques using RADARSAT-2 data is in the *figure 44*.

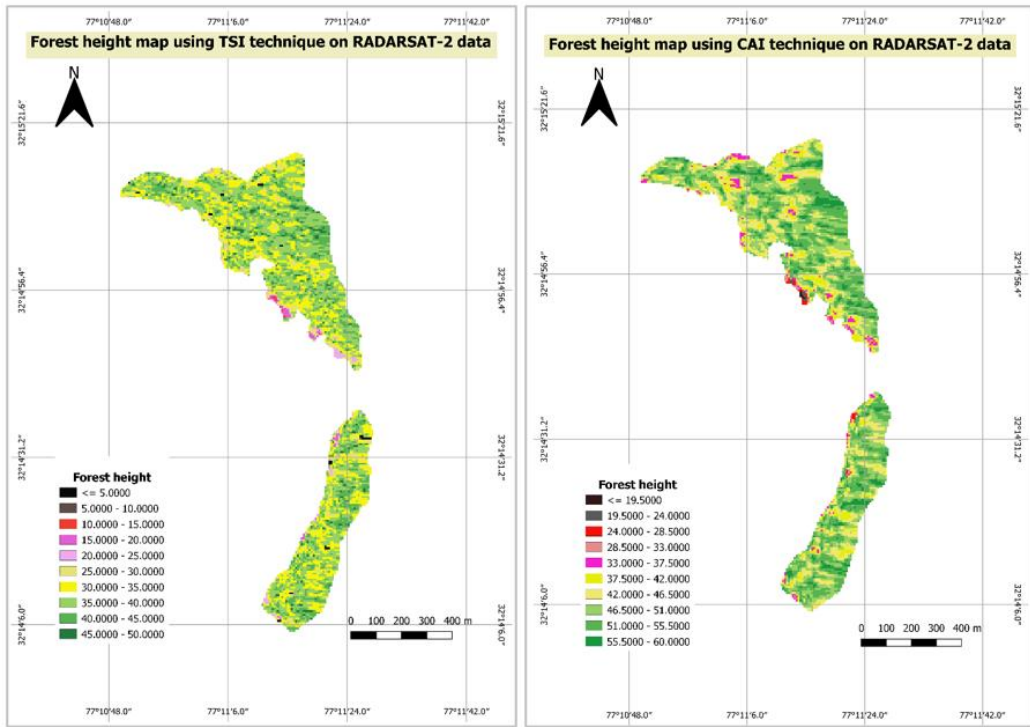


Figure 44: Height map of the Manali forest using (i) TSI technique (ii) CAI technique, on RADARSAT-2 data.

Using ALOS-2 data, the height maps generated of the Manali forests are shown in the *figure 45*, which represents only the desired area of interest. The same problem occurred in these images as well, as a height was being assigned to the urban area and the dry riverbed.

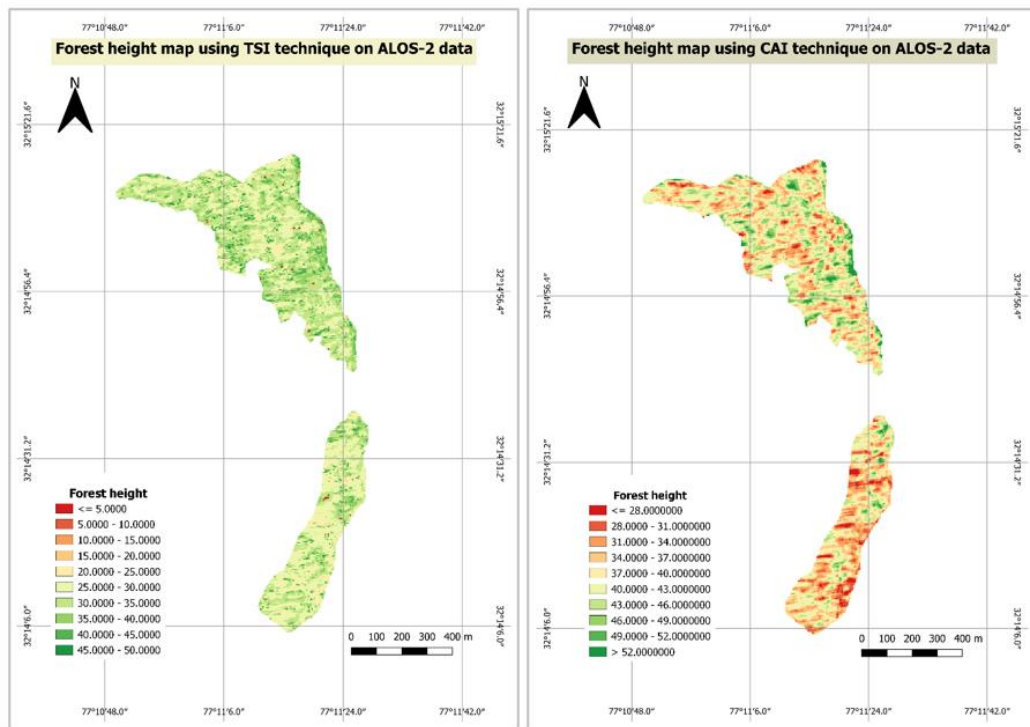


Figure 45: Height map of the Manali forest using (i) TSI technique (ii) CAI technique, on ALOS-2 data.

Forest height maps were also generated using the two techniques on TerraSAR-X data and the maps generated are as shown in the *figure 46*. The problem of estimating height values in dry riverbed and urban centres persisted here as well, which could be resolved using the improved three stage inversion method.

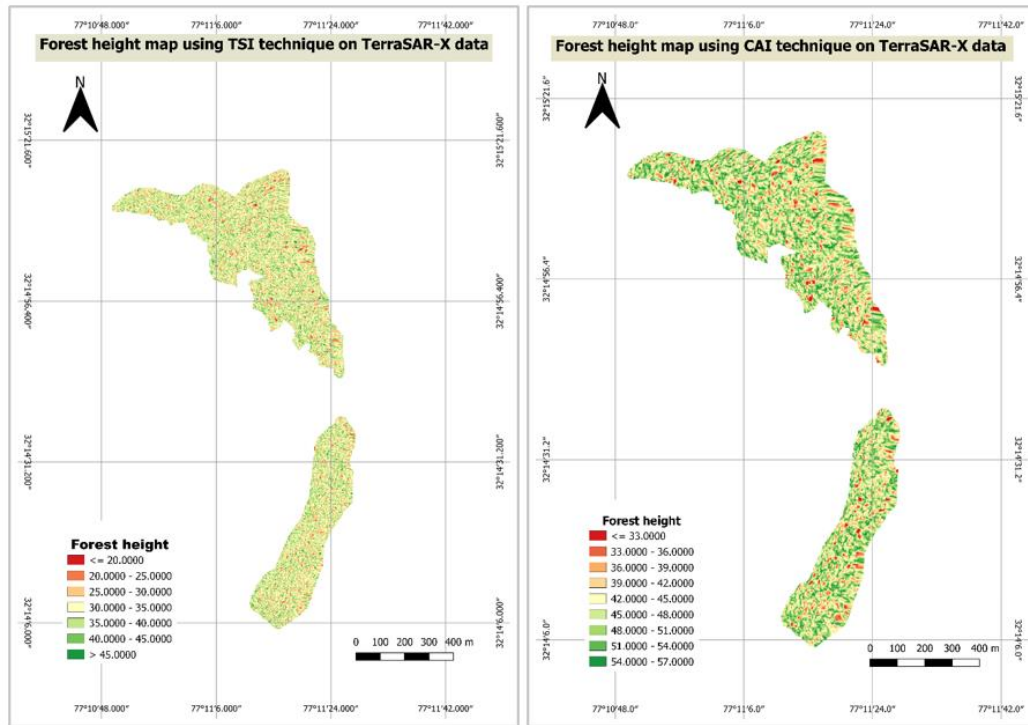


Figure 46: Height map of the Manali forest using (i) TSI technique (ii) CAI technique, on TerraSAR-X data.

The takeaway from the generated height maps is that for all the satellites, the generated forest height using Coherence Amplitude Inversion was more than that for the Three Stage Inversion method. The validation with ground truth and GEDI derived forest height maps is in the following sections.

5.6. Validation of the obtained forest height

The final step was to validate the results obtained using the field measurement plots of the tree height calculated in the field visit by Dr. Shashi Kumar in the year 2012. Further GEDI product, the forest canopy height map was chosen, and appropriate subset was taken to filter out the unrequired part of the image. This too was compared with the results obtained to study whether GEDI data can be used as an alternative to field visits for calculating the forest height.

5.6.1. Using field values

As mentioned earlier in section 3.2, field data was carried out in the region at 8 different locations in the year 2012. Each plot consisted of multiple trees, but a single ‘averaged value’ was given to the plot for convenience. Hence the validation also included multiple pixel values within the location of the field plot,

with the number of pixels chosen based upon the spatial resolution of the map. An explanation regarding selection of pixels is shown in the section 4.6.

The plot of the TSI modelled forest height for RADARSAT-2 satellite with the corresponding field calculated height is shown in *figure 47*. In the plots, blue dots represent the 8 plots of the observation, the blue coloured line is the trend line of the 8 plots, and the line depicted in yellow colour is the 45-degree line. Points closer to the yellow line reflects a better accuracy as compared to points further away from it. The numerical values on the axes reflect the tree height (or plot height in case of multiple trees) in meters.

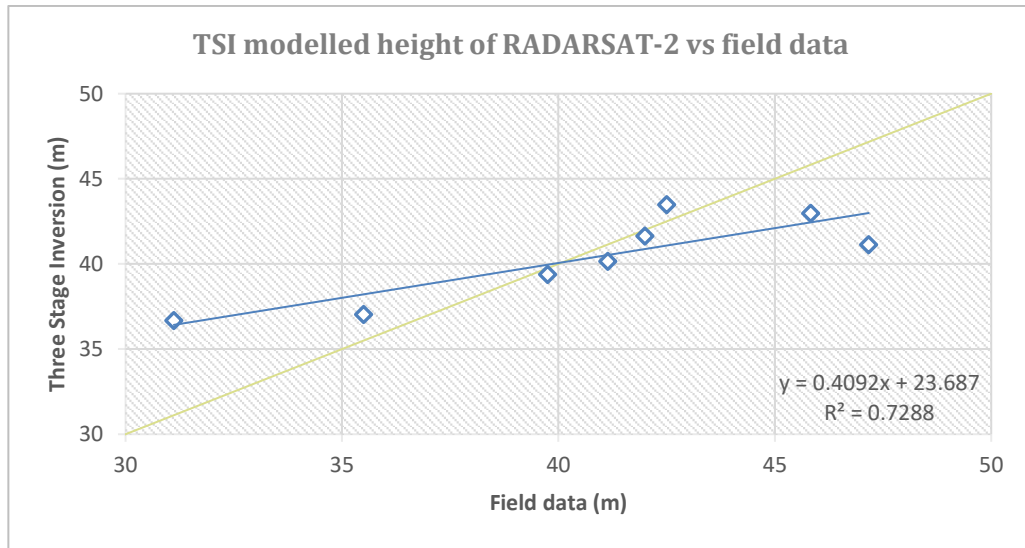


Figure 47: Plot showing the relation between the estimated forest height using TSI technique on RADARSAT-2 data and the field calculated height. The yellow line is the 45° angle line, while the blue line is the trend line.

An accuracy of 94.03% with a correlation of 0.85 were obtained when the Three Stage Inversion technique was used on the RADARSAT-2 data and compared with the field values. However, when the Coherence Amplitude Inversion technique was used to obtain the forest height, the accuracy and the correlation decreased to 84.52% and 0.64, respectively. The below *figure 48* shows the plot of forest height obtained when the Coherence Amplitude Inversion technique applied on RADARSAT-2 data was compared with the field values. The root mean square error (RMSE) for the estimate forest height using RADARSAT-2 satellite data was 3.16 m and 6.75 m, when using the TSI and CAI techniques, respectively.

The coefficient of determination, represented by R^2 , which shows how well the model has predicted the values, based on original values. For TSI technique, the value of R^2 was 0.73, while for CAI technique it was 0.40, both of which are shown in their respective figure plots.

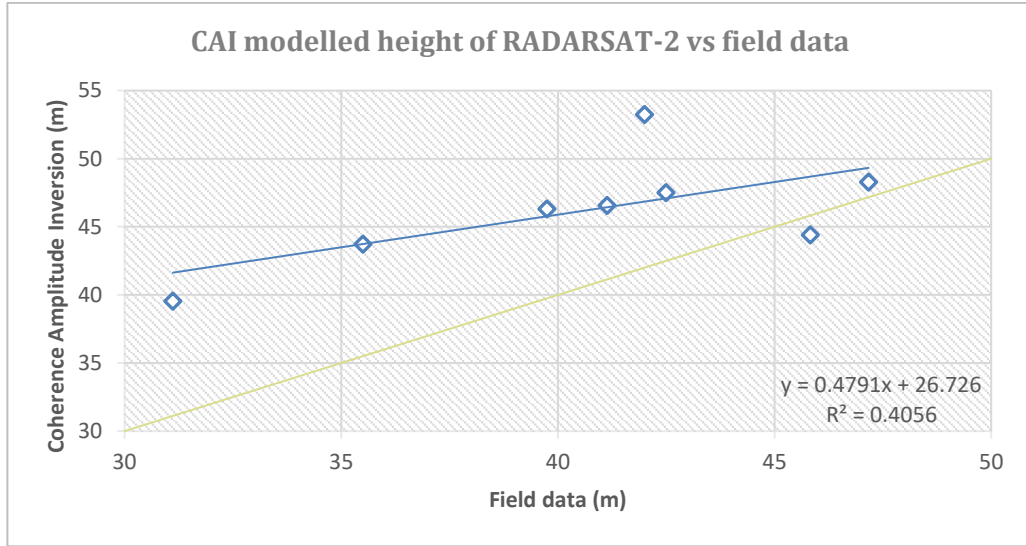


Figure 48: Plot showing the relation between the estimated forest height using CAI technique on RADARSAT-2 data and the field calculated height. As per the points, the model seemed to have overestimated the height.

For forest height map generated using ALOS-2 data, following are the plots in *figures 49 and 50*, depicting the accuracy of the obtained heights. While the accuracy using the Three Stage Inversion technique was 91.14%, using Coherence Amplitude Inversion technique, it increased to 92.22%. Though, the correlation decreased for both the techniques as it correlated just 46.27% for TSI technique and 57.62% for CAI. The RMSE for the estimate forest height using ALOS-2 satellite data was 5.6 m and 4.3 m, when using the TSI and CAI techniques, respectively. The R^2 value was 0.21 and 0.33 for TSI and CAI technique, respectively.

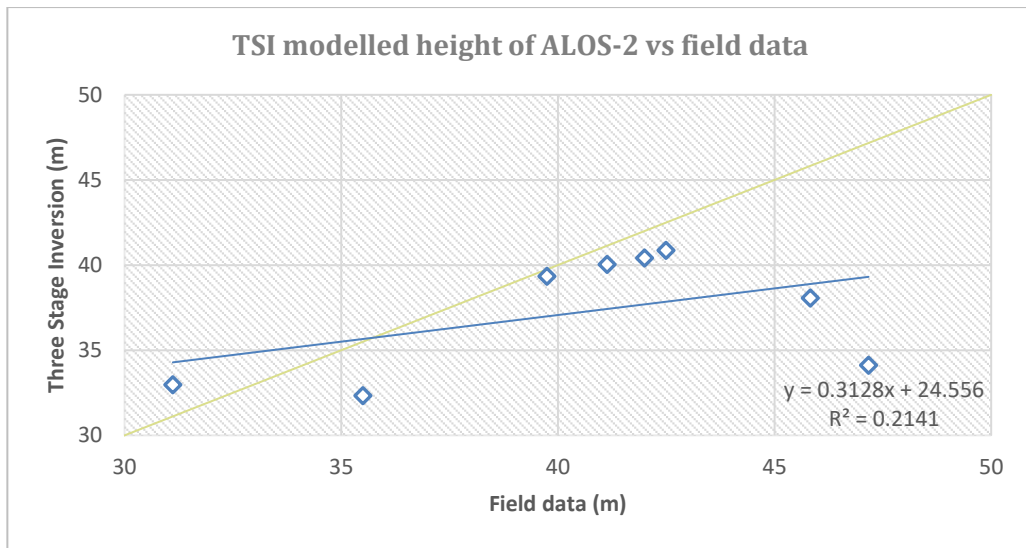


Figure 49: Plot showing the relation between the estimated forest height using TSI technique on ALOS-2 data and the field calculated height.

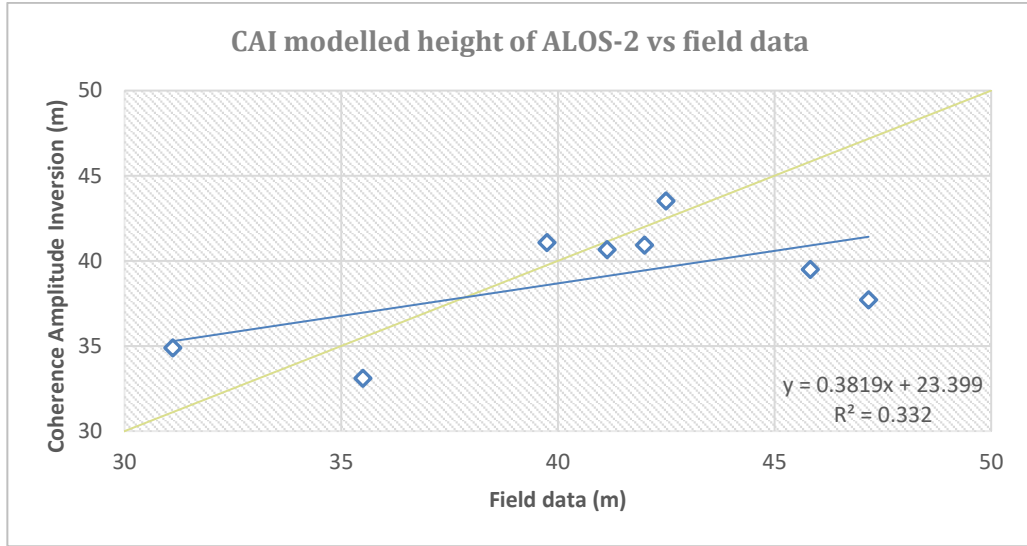


Figure 50: Plot showing the relation between the estimated forest height using CAI technique on ALOS-2 data and the field calculated height.

The accuracy of the forest height obtained when TSI technique was applied on TerraSAR-X data was 95.66%, while the correlation for the same was 0.96. With CAI technique applied on the same data, the accuracy was found to be 90.2% with a correlation of 0.91. The plots comparing the field data with the modelled height have been shown in the following *figures 51 and 52*. The RMSE for the estimate forest height using TerraSAR-X satellite data was 2.1 m and 4.3 m and R^2 value was 0.91 and 0.82, when using the TSI and CAI techniques, respectively.

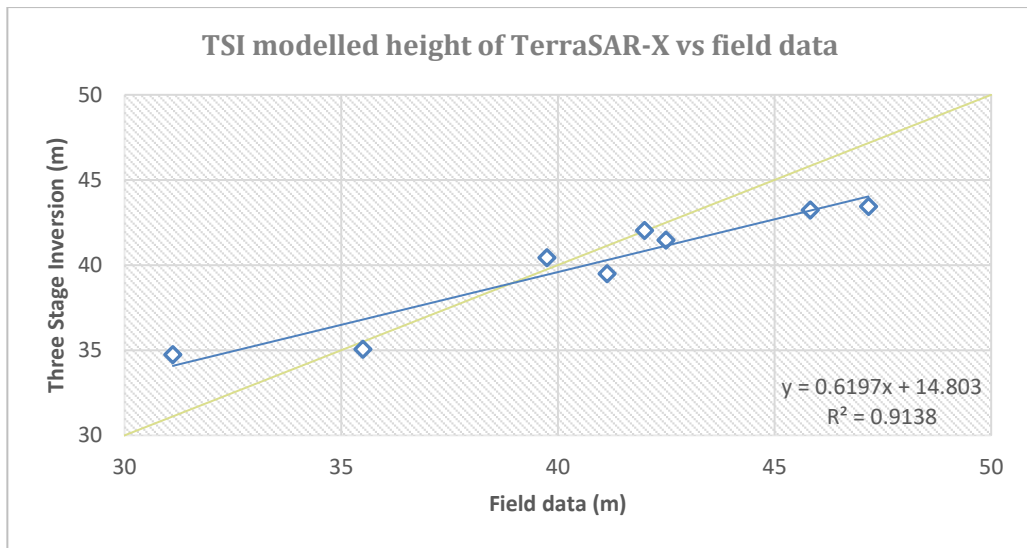


Figure 51: Plot showing the relation between the estimated forest height using TSI technique on TerraSAR-X data and the field calculated height. All the points closer to the yellow line denotes the high accuracy of the model derived height.

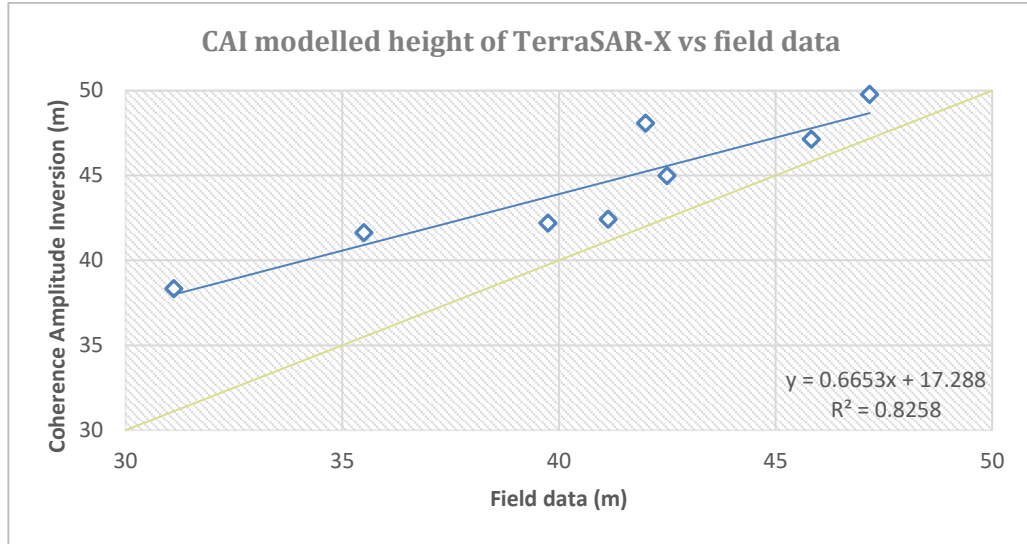


Figure 52: Plot showing the relation between the estimated forest height using CAI technique on TerraSAR-X data and the field calculated height. Again, the CAI technique seemed to have overestimated the height of trees.

5.6.2. Using GEDI data

The global forest canopy height map was downloaded as mentioned in section 4.6 and a subset of the raster was taken in accordance with the study area. Same is shown in *figure 53*, which reflects the maximum height of trees in the region to be within the range of 32 meters and 36 meters. Since the ISS bound system is associated with the Landsat data, the spatial resolution of the obtained GEDI product is poor at 30 meters. A field plot in the in-situ observations was roughly about the same with the length of a side being 31.62 meters. A similar approach was taken in comparing the modelled height with the GEDI product height and the results are shown in the following plots.

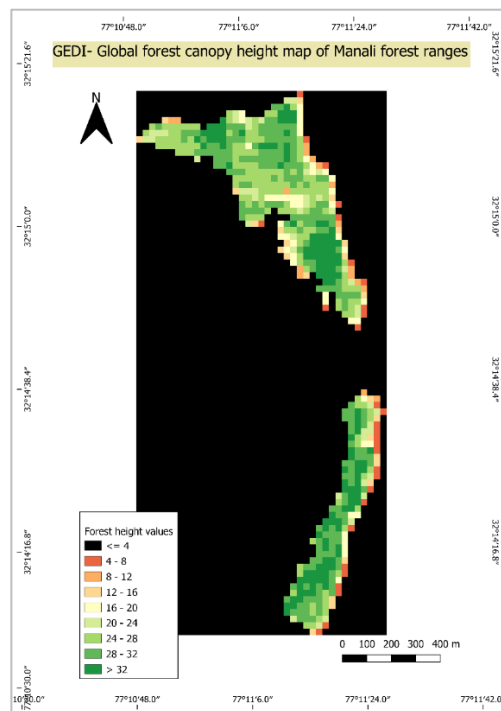


Figure 53: GEDI derived forest canopy height map of the year 2019. Downloaded from the authorised GEDI page, subset was taken using vector data in QGIS software.

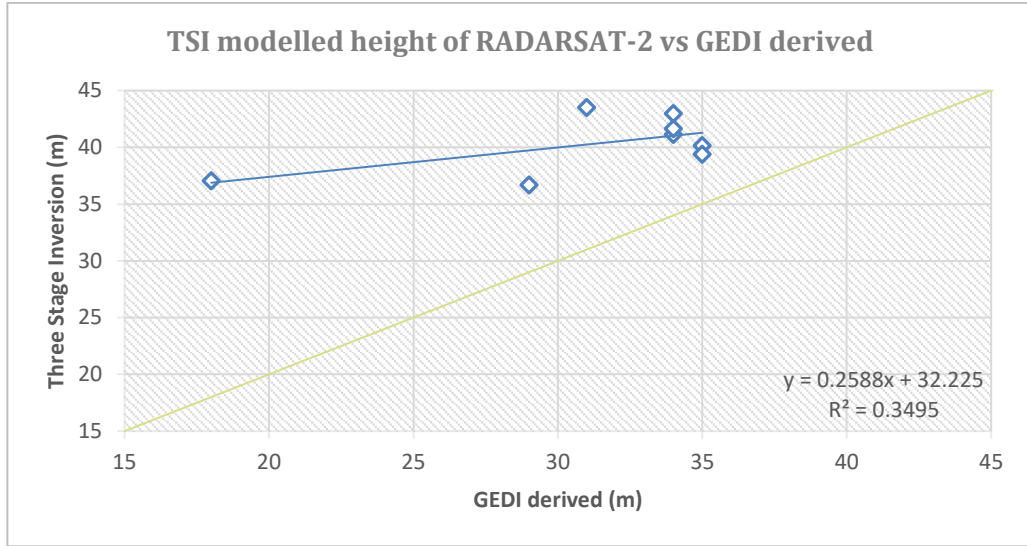


Figure 54: Plot showing the relation between the estimated forest height using TSI technique on RADARSAT-2 data and the GEDI derived height data.

A set of 5 values per plot were taken in the modelled forest height using RADARSAT-2 data. An accuracy of 67.01% was obtained when the forest height obtained using the Three Stage Inversion technique was compared with the GEDI derived forest height, along with a correlation of 0.59. On the other hand, the accuracy obtained using Coherence Amplitude Inversion method decreased to just 51.99% with a correlation of 0.44. Both the plots are shown in *figure 54 and 55*, respectively.

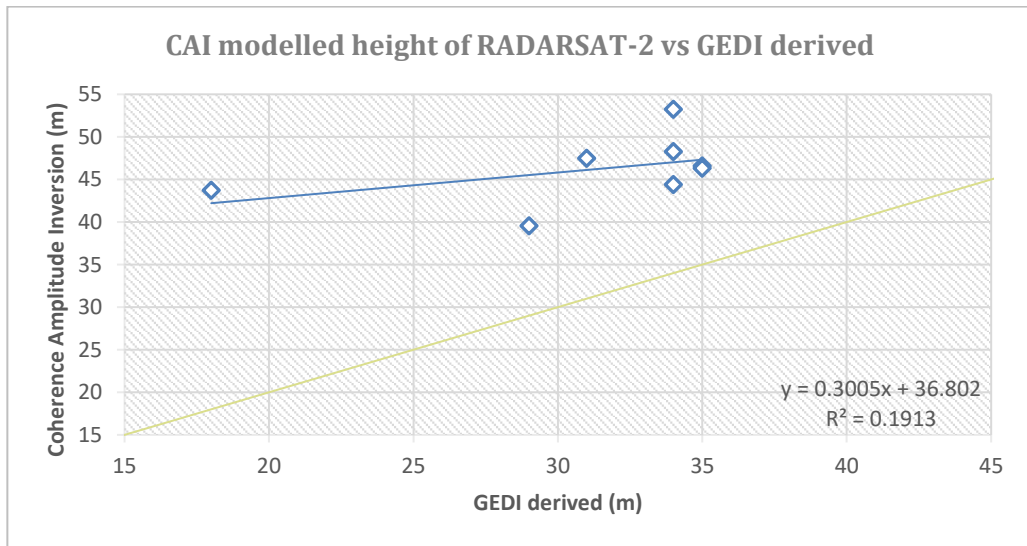


Figure 55: Plot showing the relation between the estimated forest height using CAI technique on RADARSAT-2 data and the GEDI derived height data.

For ALOS-2 data, the number of pixels taken for validation increased to 10 per plot because of a higher spatial resolution. In comparison to the RADARSAT-2 data, the accuracy upon using the ALOS-2 data increased with its value being 77.13% when using TSI technique, and 71.83% when using CAI technique.

The corresponding correlation values too increased with the value being 0.66 when using the TSI technique, and 0.74 when using the CAI technique. *Figures 56 and 57* shows the plots of the model estimated height using ALOS-2 data with GEDI derived height.

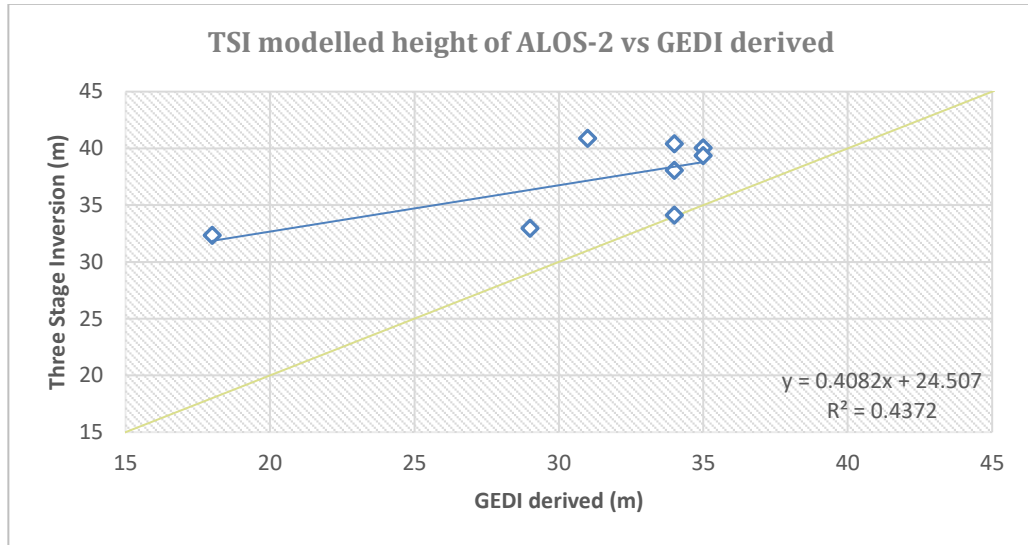


Figure 56: Plot showing the relation between the estimated forest height using TSI technique on ALOS-2 data and the GEDI derived height data.

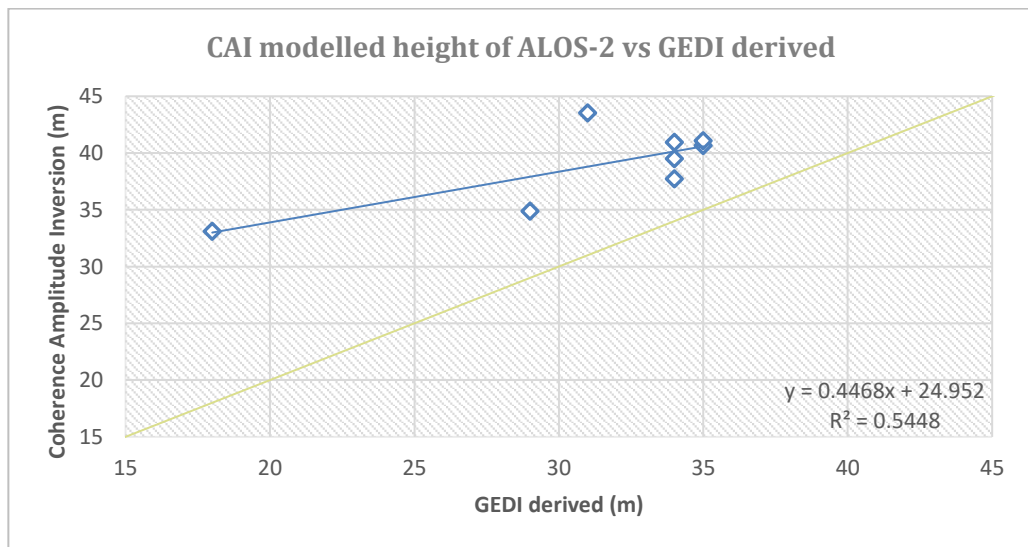


Figure 57: Plot showing the relation between the estimated forest height using CAI technique on ALOS-2 data and the GEDI derived height data.

Alike ALOS-2, 10 number of pixels per plot were taken for validating the forest height obtained using TerraSAR-X data. Although the accuracy again downgraded this time as it was only 68.13% with a correlation value of 0.73 when using the TSI method, shown in *figure 58*, and 56.81% with a correlation value of 0.43 when using the CAI method, shown in *figure 59*, in estimating the forest height. Below are the

plots showing variation of the modelled heights obtained using TerraSAR-X data with the GEDI derived forest height.

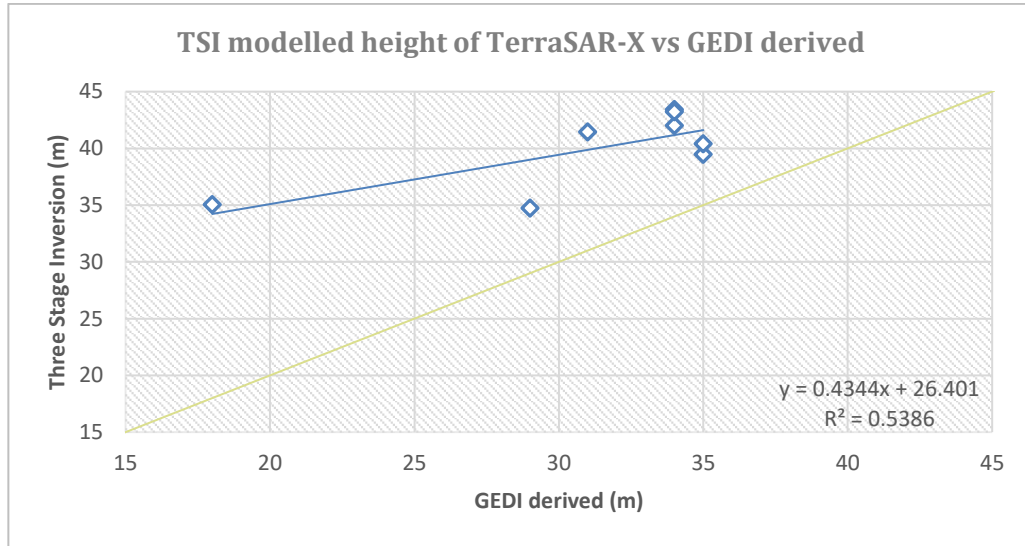


Figure 58: Plot showing the relation between the estimated forest height using TSI technique on TerraSAR-X data and the GEDI derived height data.

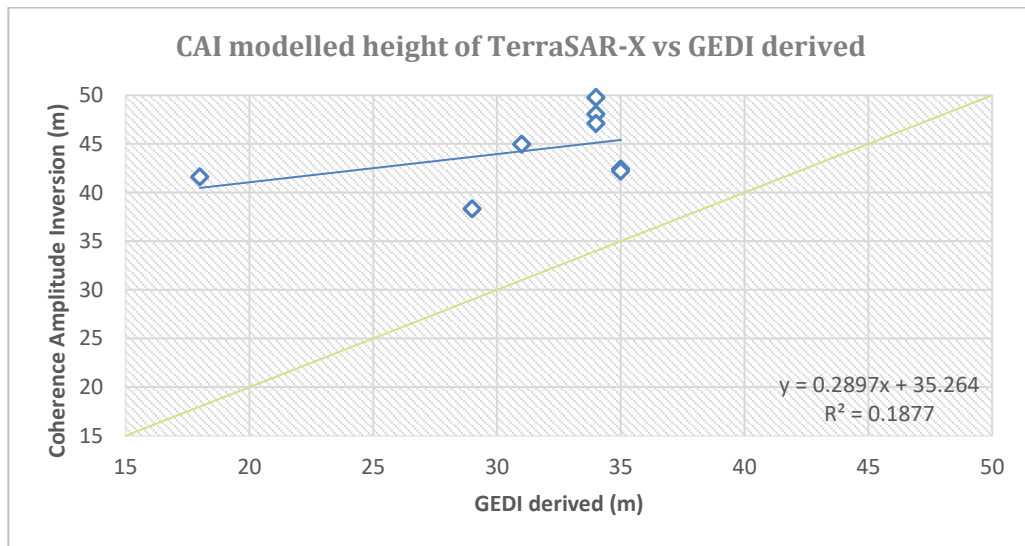


Figure 59: Plot showing the relation between the estimated forest height using CAI technique on TerraSAR-X data and the GEDI derived height data.

The trend in validating using the GEDI derived forest height maps revealed that either their system has underestimated the forest height in all the 8 field locations, or both the techniques, the Three Stage Inversion, and the Coherence Amplitude Inversion, have overestimated the forest height values. The same can be resolved when the GEDI derived values are compared with the field values.

5.6.3. Comparing field values with GEDI derived height

Field data are still the most reliable source of information. Though it poses lots of challenges such as it takes a lot of time to conduct, is costly in the long run, some area may not be accessible, etc. On the contrary,

remote sensing helps in removing all these flaws, but at the cost of accuracy. Even in this scenario, as the *figure 60*, below suggest, the GEDI derived forest height maps have underestimated the tree heights at all the 8 points when compared with the corresponding field values. Thus, it can be concluded that the ISS bound GEDI system that generated the global forest height maps in the year 2019 underestimated the forest height values. So, it may not be reliable to use that data if field visits are possible.

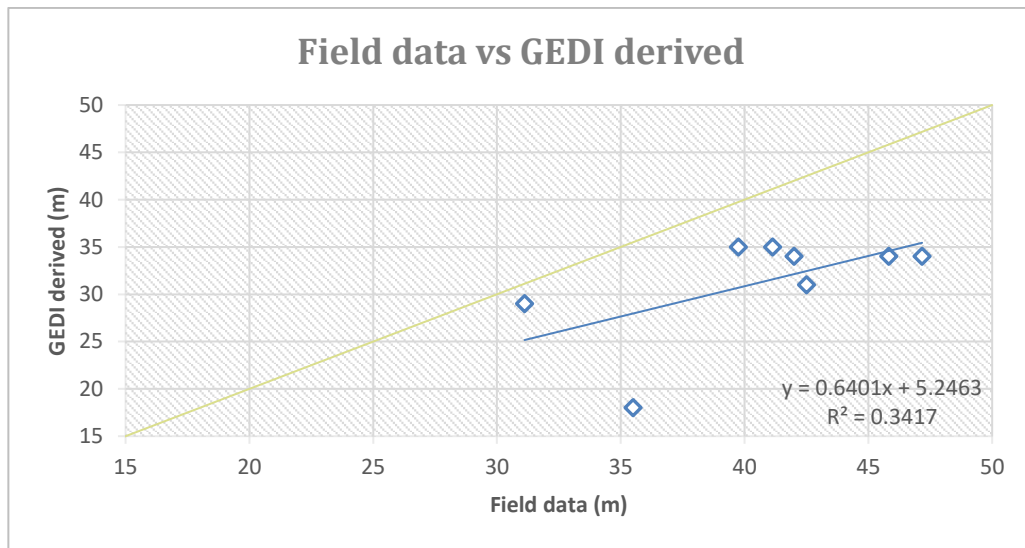


Figure 60: Plot showing the relation between the GEDI derived height data and the field calculated height data. The plot clearly shows the underestimated height of GEDI product, Global Forest Canopy Height map 2019.

5.7. Sources of error

Keeping in mind the scope of the study, necessary assumptions were taken at some points in the study, which could make up to the sources of error. This section aims to cover up for the inevitable things that could not be compensated for.

The satellite data pairs had temporal gap of about a month, which could have induced the temporal decorrelation factor in the forests. But, since the repeat pass of the 3 spaceborne satellites is less than about a month, this thing couldn't have been resolved.

The field study of the forests was performed by Dr. Shashi Kumar in the year 2012 (due to the Corona outbreak, field visit could not happen which was scheduled in May 2021), while the satellite data were of the year 2012 and 2015. In 3 years of time, it is possible that topography of the forest would have changed, which could be in terms of their height, or their presence. With land use change happening all over the world, it is possible that during the time gap, multiple trees would have felled or because of natural disasters the trees would have vanished. This could have been a serious problem for validating the results as tree heights could have changed in the gap of 3 years, even though they were matured.

Another flaw in the study was the use of GEDI product, the forest canopy height map of the year 2019, which increases the gap with the satellite data of the years 2012 and 2015. A decent correlation graph could

have been plotted showing how the tree heights in the region have altered over the gap of 7 years, but the GEDI product underestimated the forest height at many locations.

A study by Khati (Khati & Kumar, 2014) suggested the use of the improved three stage inversion model for estimation of forest height, that would compensate for the inaccurate heights being shown in river and urban areas. Considering the time frame of the study, that was also not performed.

6. CONCLUSIONS AND RECOMMENDATIONS

6.1. Conclusions

Forest height of the Manali forest range were obtained using three stage inversion and coherence amplitude inversion techniques and verified through field data. For the X band data, accuracy obtained was 95.66% with a correlation of 0.96 and an RMSE of 2.1 meters, when TSI technique was used. For the same data, the accuracy reduced to 90.02% with a correlation of 0.91, and the RMSE increased to 4.3 meters while using the CAI technique. For the C band data, when the TSI technique was used to estimate the forest height, 94.03% of accuracy was obtained with a correlation of 0.85 and an RMSE of 3.16 meters. The accuracy, correlation, and the RMSE changed to 84.52%, 0.64, and 6.75 meters, respectively, when the technique used was CAI. While, for the L band data, the accuracy of the maps generated was 91.14% and 92.22% upon using TSI and CAI techniques, respectively. The RMSE errors also were considerable in this data with errors being 5.6 meters in TSI technique and 4.3 meters in CAI technique.

Table 5: Observation of TSI derived forest heights of the 3 satellites when validated with field values.

Parameter	TerraSAR-X	RADARSAT-2	ALOS-2 PALSAR-2
<i>Accuracy</i>	95.66%	94.03%	91.14%
<i>Correlation value</i>	0.96	0.85	0.46
<i>Coefficient of determination (R²)</i>	0.91	0.73	0.21
<i>RMSE</i>	2.1 meters	3.16 meters	5.6 meters

Table 6: Observation of CAI derived forest heights of the 3 satellites when validated with field values.

Parameter	TerraSAR-X	RADARSAT-2	ALOS-2 PALSAR-2
<i>Accuracy</i>	90.02%	84.52%	92.22%
<i>Correlation value</i>	0.91	0.64	0.57
<i>Coefficient of determination (R²)</i>	0.82	0.4	0.33
<i>RMSE</i>	4.3 meters	6.75 meters	4.3 meters

Based on all these statistics and other sensor properties such as the spatial and temporal resolution, we may conclude as to which sensor could be the best suitable for obtaining the forest height. Since X band satellite TerraSAR-X had the most accuracy while using TSI technique and a decent accuracy while using CAI technique, it could possibly be the best satellite sensor for the purpose of obtaining tree heights. Even the value of RMSE is one of the lowest for the height obtained using both of these techniques. This was followed by the L band data ALOS-2 PALSAR-2, which had a decent accuracy and lower value of RMSE,

as compared to RADARSAT-2 data. Last in the queue would be RADARSAT-2 with the lowest accuracy and the highest RMSE value amongst the three data.

Amongst TSI and CAI, based on the accuracy and the RMSE of the model generated forest heights, we may conclude that TSI model generates forest height maps more accurately with a lesser RMSE. Also, with the use of the improved three stage inversion model used by Khati (Khati & Kumar, 2014), the inaccurate height values given to river and urban features could be replaced with original height values.

We may also comment on the forest canopy height map of GEDI, which was used to verify the height results obtained through the PolInSAR technique. Upon comparison with the field data, it was concluded that the GEDI product had underestimated the height at several locations. At some locations with a normal height of the tree, the model has not estimated the forest height.

Although many authors believed P band to be the most suitable frequency band in SAR sensor for estimating forest parameters (Santoro, 2003), this study showed for the height of trees, X band sensor is the most suitable as it not only had the most accuracy amongst the three satellite data used, but also the RMSE value is one of the lowest. Even though its penetrating capability is very less, due to its very high spatial resolution, the ground information was obtained at the X band sensor through the canopy gaps (shown in *figure 12*) which enabled TerraSAR-X to have the most accurate results amongst the three satellites.

6.2. Recommendations

For obtaining the best results of the canopy height, the improved three stage inversion (Khati & Kumar, 2014) is a must step that would first bifurcate on the basis of coherence values and then based on the radar backscatter intensity, separate water features from forest features. Thus, accurate height of all the features would be obtained.

The study was validated using field values from 8 different locations within the 2 forest ranges, which are very less. It is recommended to conduct another field visit to the area and have a greater number of plots to verify the results obtained through models.

LIST OF REFERENCES

- Aghababaei, H., Ferraioli, G., Ferro-famil, L., Huang, Y., Alessandro, M. M. D., Pascazio, V., Schirinzi, G., & Tebaldini, S. (2020). *Forest SAR Tomography: Principles and Applications*.
- Aghabalaei, A., Ebadi, H., & Maghsoudi, Y. (2020). *Forest height estimation based on the RVOG inversion model and the PolInSAR decomposition technique*. 1161. <https://doi.org/10.1080/01431161.2019.1694726>
- Asopa, U., & Kumar, S. (2020). *UAVSAR Tomography for Vertical Profile Generation of Tropical Forest of Mondak National Park , Gabon*. 0–2. <https://doi.org/10.1029/2020EA001230>
- Attema, E. P. W., & Ulaby, F. T. (1978). *Vegetation modeled as a water cloud*. 13(2), 357–364.
- Babu, A., & Kumar, S. (2018). *TREE CANOPY HEIGHT ESTIMATION USING MULTI BASELINE RVOG TREE CANOPY HEIGHT ESTIMATION USING MULTI BASELINE RVOG INVERSION*. November. <https://doi.org/10.5194/isprs-archives-XLII-5-605-2018>
- Brown, S. (1997). *Estimating biomass and biomass change of tropical forests. a primer*. Forest Resources Assessment publication. <https://www.fao.org/3/W4095E/W4095E00.htm>
- Chandola, S., Kumar, S., & Tolpekin, V. A. (2014). *Polarimetric SAR Interferometry for Forest Aboveground Biomass Estimation* (Issue March).
- Chen, W., Zheng, Q., Xiang, H., & Chen, X. (2021). *Forest Canopy Height Estimation Using Polarimetric Interferometric Synthetic Aperture Radar (PolInSAR) Technology Based on Full-Polarized ALOS / PALSAR Data*.
- Cloude, S R, & Papathanassiou, K. P. (2003). *Three-stage inversion process for polarimetric SAR interferometry*. I(3), 125–134.
- Cloude, Shane R. (2005). *POL-InSAR TRAINING COURSE*. 1–44.
- Cloude, Shane R. (2006). *Polarization coherence tomography*. 41(August). <https://doi.org/10.1029/2005RS003436>
- Cloude, Shane Robert, & Papathanassiou, K. P. (1998). *Polarimetric SAR Interferometry*. 36(5), 1551–1565.
- Cloude, Shane Robert, & Pottier, E. (1996). *A review of Target Decomposition theorems in Radar Polarimetry*. 34(2).
- Deep, S., & Kushwaha, S. P. S. (2020). *Urbanization , Urban Sprawl and Environment in Dehradun*. January. <https://doi.org/10.1007/978-981-13-9310-5>
- Denbina, M., Simard, M., & Hawkins, B. (2018). *Forest Height Estimation Using Multibaseline PolInSAR and Sparse Lidar Data Fusion*. 1–19.
- DePasquale, J., Kowal Arcand, K., & Edmonds, P. (2015). *High Energy Vision: Processing X-rays*. <https://doi.org/10.11114/smc.v3i2.913>
- ESA-SNAP. *Help Contents*. (n.d.).
- Ferretti, A., Monti-guarnieri, A., Prati, C., & Rocca, F. (2007). *InSAR Principles: Guidelines for SAR Interferometry Processing and Interpretation* (Issue February).
- Forest Carbon Stock*. (n.d.). <https://www.forestresearch.gov.uk/tools-and-resources/statistics/forestry-statistics/forestry-statistics-2018/uk-forests-and-climate-change/forest-carbon-stock/>

- Ghosh, K., Kumar, S., & Tolpekin, V. A. (2018). *Multi-Baseline PolInSAR inversion and simulation of interferometric wavenumber for forest height retrieval using spaceborne SAR data.*
- Gorte, R. W., & Sheikh, P. A. (2010). *Deforestation and Climate Change.*
- Hajnsek, I., Kugler, F., Lee, S., Papathanassiou, K. P., & Member, S. (2009). *Tropical-Forest-Parameter Estimation by Means of Pol-InSAR: The INDREX-II Campaign.* 47(2), 481–493.
- Jin, Y.-Q., & Xu, F. (2013). *Polarimetric Scattering and SAR Information Retrieval.* 2013 John Wiley & Sons Singapore Pte. Ltd. <https://doi.org/10.1002/9781118188149>
- Joshi, S. K., & Kumar, S. (2017). *Performance of PolSAR backscatter and PolInSAR coherence for scattering characterization of forest vegetation using single pass X-band spaceborne synthetic aperture radar data.* 11(2). <https://doi.org/10.1117/1.JRS.11.026022>
- Khati, U. G., & Kumar, S. (2014). *POLINSAR BASED SCATTERING INFORMATION AND PHYSICAL PROPERTY RETRIEVAL OF VEGETATION.*
- Krieger, G., Papathanassiou, K. P., & Cloude, S. R. (2005). *Spaceborne Polarimetric SAR Interferometry: Performance Analysis and Mission Concepts.* 3272–3292.
- Kugler, F., Lee, S., Hajnsek, I., & Papathanassiou, K. P. (2015). *Forest Height Estimation by Means of Pol-InSAR Data Inversion: The Role of the Vertical Wavenumber.* 53(10), 5294–5311.
- Kumar, P., & Krishna, A. P. (2019). *InSAR-Based Tree Height Estimation of Hilly Forest Using Multitemporal Radarsat-1 and.* 1–6.
- Kumar, S. (2009). *Retrieval of forest parameters from Envisat ASAR data for biomass inventory in Retrieval of forest parameters from Envisat ASAR data for biomass inventory in.*
- Kumar, S., Dev, R., Kushwaha, G. S. P. S., Jayawardhana, W. G. N. N., & Agarwal, S. (2017). *Bistatic PolInSAR Inversion Modelling for Plant Height Retrieval in a Tropical Forest. Proceedings of the National Academy of Sciences, India Section A: Physical Sciences,* 87(4), 817–826. <https://doi.org/10.1007/s40010-017-0451-9>
- Kumar, S., Govil, H., Srivastava, P. K., Thakur, P. K., & Kushwaha, S. P. S. (2020). *Spaceborne Multifrequency PolInSAR-Based Inversion Modelling for Forest Height Retrieval.*
- Kuniyal, J. C., Jain, A. P., & Shannigrahi, A. S. (2003). *Environmental Impacts of Tourism in Kullu-Manali complex in North Western Himalaya, India. Part 1: The Adverse Impacts.* October 2014.
- Lee, J., Fellow, L., Ainsworth, T. L., & Member, S. (2011). *The Effect of Orientation Angle Compensation on Coherency Matrix and Polarimetric Target Decompositions.* 49(1), 53–64.
- Lee, S. (2013). *Forest parameter estimation using polarimetric SAR interferometry techniques at low frequencies.*
- Lee, S., Kugler, F., Hajnsek, I., & Papathanassiou, K. P. (2009). *The Impact of Temporal Decorrelation over Forest Terrain in Polarimetric SAR Interferometry The Impact of Temporal Decorrelation over Forest Terrain in Polarimetric SAR Interferometry.* January.
- Li, S., Liu, Q., Wang, N., Li, Z., Chen, E., Pang, Y., Si, L., & Tian, X. (2019). *Forest Stand Height Estimation Using Ziyuan-3 Tri-Stereo Imagery and Lidar.*
- Managhebi, T., & Maghsoudi, Y. (2018). *Four-Stage Inversion Algorithm for Forest Height Estimation Using Repeat*

- Pass Polarimetric SAR Interferometry Data*. <https://doi.org/10.3390/rs10081174>
- Mette, T, Papathanassiou, K., & Hajnsek, I. (2004). *Biomass estimation from polarimetric SAR interferometry over heterogeneous forest terrain*. 00(C), 511–514.
- Mette, Tobias, & Knoke, T. (2006). *Forest Biomass Estimation from Polarimetric SAR Interferometry*.
- Mette, Tobias, Papathanassiou, K. P., Hajnsek, I., & Zimmermann, R. (2002). *Forest Biomass Estimation Using Polarimetric SAR Interferometry*. January 2014. <https://doi.org/10.1109/IGARSS.2002.1025695>
- Minguez, J. C. S., Osborne, P. E., Cloude, S. R., Woodhouse, I. . ., Hope, J., & G, W. (2001). *The Glen Affric Project : forrest mapping using dual baseline polarimetric radar interferometry*. September 2014.
- Minh, D. H. T., Toan, T. Le, Rocca, F., Tebaldini, S., Alessandro, M. M. D., & Villard, L. (2014). *Relating P-Band Synthetic Aperture Radar Tomography to Tropical Forest Biomass*. 52(2).
- Mukhopadhyay, R., Kumar, S., & Aghababaei, H. (2021). *Estimation of aboveground biomass from PolSAR and PolInSAR using regression-based modelling techniques*. <https://doi.org/10.1080/10106049.2021.1878289>
- NASA-JPL: NISAR Mission. (n.d.). <https://nisar.jpl.nasa.gov/>
- NASA-JPL: Seasat. (n.d.). <https://www.jpl.nasa.gov/missions/seasat>
- Papathanassiou, K. P., & Cloude, S. R. (2001). *Single-Baseline Polarimetric SAR Interferometry*. 39(11), 2352–2363.
- Parida, B. R., & Mandal, S. P. (2020). *Polarimetric decomposition methods for LULC mapping using ALOS L - band PolSAR data in Western parts of Mizoram , Northeast India*. January.
- Pepe, A., & Calo, F. (2017). *A Review of Interferometric Synthetic Aperture RADAR (InSAR) Multi-Track Approaches for the Retrieval of Earth's Surface Displacements*. <https://doi.org/10.3390/app7121264>
- Sadeghi, Y., St-onge, B., Leblon, B., Simard, M., & Papathanassiou, K. (2011). *MAPPING FOREST CANOPY HEIGHT USING TANDEM-X DSM AND AIRBORNE LIDAR DTM*. 2, 2–5.
- Santoro, M. (2003). *Estimation of Biophysical Parameters in Boreal Forests from ERS and JERS SAR Interferometry*. *Estimation of Biophysical Parameters in Boreal Forests from ERS and JERS SAR Interferometry* (Issue 188).
- Shukla, J., Nobre, C., & Sellers, P. (1990). *Amazon Deforestation and Climate Change*. 1–4.
- Skolnik, M. I. (n.d.). *RADAR HANDBOOK* (D. A. Gonneau & B. E. Eckes (Eds.)). McGraw-Hill Publishing Company.
- Yamaguchi, Y., Moriyama, T., & Ishido, M. (2005). *Four-Component Scattering Model for Polarimetric SAR Image Decomposition*. 43(8), 1699–1706.